

Non-linear Recovery of Sparse Signal Representations with Applications to Temporal and Spatial Localization

THÈSE N° 6605 (2015)

PRÉSENTÉE LE 27 AVRIL 2015

À LA FACULTÉ DES SCIENCES ET TECHNIQUES DE L'INGÉNIEUR

GROUPE VAN DE VILLE

PROGRAMME DOCTORAL EN GÉNIE ÉLECTRIQUE

ÉCOLE POLYTECHNIQUE FÉDÉRALE DE LAUSANNE

POUR L'OBTENTION DU GRADE DE DOCTEUR ÈS SCIENCES

PAR

Zafer DOĞAN

acceptée sur proposition du jury:

Prof. J.-Ph. Thiran, président du jury

Prof. D. Van De Ville, Prof. T. Blu, directeurs de thèse

Prof. P. Frossard, rapporteur

Prof. Y. Lu, rapporteur

Prof. A. Pizurica, rapporteuse



ÉCOLE POLYTECHNIQUE
FÉDÉRALE DE LAUSANNE

Suisse
2015

Thèse N° 6605 (April 2015)

*Thèse présentée à la faculté des sciences et techniques de l'ingénieur
pour l'obtention du grade de docteur ès sciences
et acceptée sur proposition du jury*

Prof. Jean-Philippe Thiran, *président*
Prof. Dimitri Van De Ville, *directeur de thèse*
Prof. Thierry Blu, *co-directeur de thèse*
Prof. Yue M. Lu, *rapporteur*
Prof. Aleksandra Pizurica, *rapporteur*
Prof. Pascal Frossard, *rapporteur*

École polytechnique fédérale de Lausanne—2015

Cover design by Zafer Doğan
Printing and binding by Repro-EPFL
Typeset with L^AT_EX
Copyright © 2015 by Zafer Doğan
Available at <http://miplab.epfl.ch/>

Abstract

Foundations of signal processing are heavily based on Shannon's sampling theorem for acquisition, representation and reconstruction. This theorem states that signals should not contain frequency components higher than the Nyquist rate, which is half of the sampling rate. Then, the signal can be perfectly reconstructed from its samples. Increasing evidence shows that the requirements imposed by Shannon's sampling theorem are too conservative for many naturally-occurring signals, which can be accurately characterized by sparse representations that require lower sampling rates closer to the signal's intrinsic information rates. Finite rate of innovation (FRI) is a new theory that allows to extract underlying sparse signal representations while operating at a reduced sampling rate. The goal of this PhD work is to advance reconstruction techniques for sparse signal representations from both theoretical and practical points of view. Specifically, the FRI framework is extended to deal with applications that involve temporal and spatial localization of events, including inverse source problems from radiating fields.

The concept of finite rate of innovation (FRI) has been introduced for the sampling and reconstruction of specific classes of continuous-time signals that feature a sparse parametric signal representation such that they have finite degrees of freedom per unit time. Examples of such FRI signals are streams of Diracs, stream of short pulses, piecewise polynomials and piecewise sinusoidal signals. Clearly, these signals are neither bandlimited nor belong to a fixed subspace, and hence the classical sampling theory does not hold. Several new methods in the framework of FRI have shown that it is possible to develop exact sampling and reconstruction schemes to recover the signal innovations. In particular, this is achieved by adequate handling of the signal acquisition, which remains linear, but at the expense of non-linear reconstruction methods.

We propose a novel reconstruction method using a model-fitting approach that is based on minimizing the fitting error subject to an underlying annihilation system given by the Prony's method. First, we showed that this is related to the problem known as structured low-rank matrix approximation as in structured total least squares problem. Then, we proposed to solve our problem under three different constraints using the iterative quadratic maximum likelihood algorithm. Our analysis and simulation results indicate that the proposed algorithms improve the robustness of the results with respect to common FRI reconstruction schemes.

We have further developed the model-fitting approach to analyze spontaneous brain activity as measured by functional magnetic resonance imaging (fMRI). For this, we considered the noisy fMRI time course for every voxel as a convolution between an underlying activity inducing signal (i.e., a stream of Diracs) and the hemodynamic response function (HRF). We then validated this method using experimental fMRI data acquired during an event-related study. The results showed for the first time evidence for the practical usage of FRI for fMRI data analysis.

We also addressed the problem of retrieving a sparse source distribution from the boundary measurements of a radiating field. First, based on Green's theorem, we proposed a sensing principle that allows to relate the boundary measurements to the source distribution. We focused on characterizing these sensing functions with particular attention for those that can be derived from holomorphic functions as they allow to control spatial decay of the sensing functions. With this selection, we developed an FRI-inspired non-iterative reconstruction algorithm. Finally,

we developed an extension to the sensing principle (termed eigensing) where we choose the spatial eigenfunctions of the Laplace operator as the sensing functions. With this extension, we showed that eigensing principle allows to extract partial Fourier measurements of the source functions from boundary measurements. We considered photoacoustic tomography as a potential application of these theoretical developments.

Keywords: signal models, sparsity, finite rate of innovation, regularized reconstruction, inverse source problems, Helmholtz equation, functional magnetic resonance imaging, photoacoustic tomography

Résumé

Les fondements de la théorie du traitement du signal sont fortement basés sur le théorème d'échantillonnage de Shannon pour l'acquisition, la représentation et la reconstruction. Ce théorème indique que les signaux ne doivent pas contenir des composantes de fréquence supérieure à la fréquence de Nyquist, qui est la moitié du taux d'échantillonnage. Ainsi, le signal peut être parfaitement reconstruit à partir de ses échantillons. Il devient de plus en plus évident que les conditions imposées par le théorème d'échantillonnage de Shannon sont trop conservatives pour de nombreux signaux naturels, qui peuvent être caractérisés avec précision par des représentations parcimonieuses qui exigent des taux d'échantillonnage plus faibles et qui sont plus proches du taux d'information intrinsèque du signal. La théorie des taux fini d'innovation (TFI) est une nouvelle approche qui permet d'extraire des représentations exactes de signaux sous-jacente tout en fonctionnant à une fréquence d'échantillonnage réduite. Le but du travail de cette thèse est de faire progresser les techniques de reconstruction des représentations parcimonieuses de signaux, de point de vue théorique et pratique. Plus précisément, le cadre TFI est étendu pour traiter des applications qui impliquent la localisation spatiale et temporelle des événements, y compris les problèmes inverses de source de champs rayonnants.

Le concept de taux fini d'innovation (TFI) a été introduit pour l'échantillonnage et la reconstruction de catégories spécifiques de signaux continus dans le temps qui disposent d'une représentation parcimonieuse et paramétrique du signal telle qu'ils aient des degrés de liberté finis par unité de temps. Quelques exemples de tels signaux TFI sont les flux de Dirac, les flux d'impulsions courtes, les polynômes par morceaux et les signaux sinusoïdaux. De toute évidence, ces signaux ne sont ni à bande limitée, ni n'appartiennent à un sous-espace fixe, et donc la théorie de l'échantillonnage classique ne tient plus. Plusieurs nouvelles méthodes dans le cadre du TFI ont montré qu'il est possible de développer des systèmes d'échantillonnage et de reconstruction exacte pour récupérer les innovations du signal. En particulier, ceci est réalisé par une manipulation appropriée de l'acquisition du signal, qui reste linéaire, mais au détriment de méthodes de reconstruction non linéaires.

Nous proposons une nouvelle méthode de reconstruction en utilisant une approche de modèle ajusté qui est basée sur la minimisation de l'erreur d'ajustement soumise à un système d'annihilation sous-jacent donné par la méthode de Prony. Tout d'abord, nous avons montré que ceci est lié au problème connu sous le nom d'approximation structurée de matrices à faible rang comme structurée dans le problème des moindres carrés totales. Ensuite, nous avons proposé de résoudre notre problème sous trois contraintes différentes en utilisant l'algorithme itératif du maximum de vraisemblance quadratique. Nos analyses et simulations indiquent que les algorithmes proposés améliorent la robustesse des résultats par rapport aux méthodes usuelles de reconstruction à TFI.

Nous avons développé l'approche du modèle ajusté pour analyser l'activité cérébrale spontanée telle que mesurée par l'imagerie par résonance magnétique fonctionnelle (IRMf). Pour cela, nous avons considéré le signal bruité de l'IRMf pour chaque voxel comme une convolution entre un signal induisant d'activité sous-jacente (c.à.d., un flux de Dirac) et la fonction de réponse hémodynamique (FRH). Nous avons ensuite validé cette méthode en utilisant des données IRMf expérimentales acquises au cours d'une étude liée à un événement. Les résultats ont montré pour

la première fois l'évidence de l'utilisation pratique du TFI pour l'analyse des données IRMf.

Nous avons également abordé le problème de la récupération d'une distribution parcimonieuse de source à partir des mesures aux bords d'un champ rayonnant. Premièrement, on se basant sur le théorème de Green, nous avons proposé un principe de détection qui permet de relier les mesures aux bords à la distribution source. Nous nous sommes concentrés sur les fonctions de détection avec une attention particulière pour celles qui peuvent être dérivées de fonctions holomorphes car elles permettent de contrôler la décroissance spatiale des fonctions de détection. Avec cette sélection, nous avons développé un algorithme de reconstruction non-itérative inspiré par le TFI. Enfin, nous avons développé une extension du principe de détection (appelé détection propre) où nous choisissons les fonctions spatiales propres de l'opérateur de Laplace comme fonctions de détection. Grâce à cette extension, nous avons montré que le principe de la détection propre permet d'extraire des mesures partielles de Fourier des fonctions sources à partir des mesures aux bords. Nous avons considéré la tomographie photo-acoustique comme application potentielle des développements théoriques de cette thèse.

Mots-clés : modèles de signaux, parcimonie, taux fini d'innovation, reconstruction régularisée, problèmes de source inverse, équation de Helmholtz, imagerie par résonance magnétique fonctionnelle, tomographie photo-acoustique.

To my family

Acknowledgement

I would like to express my great appreciation to many people who had supported me during my doctoral studies without whom this manuscript would not have been possible.

First and foremost, I would like to express my deep gratitude to Prof. Dimitri Van De Ville and Prof. Thierry Blu, my research supervisors, for their patient guidance, enthusiastic encouragement and useful critiques of this research work. Prof. Van De Ville, the head of MIPLAB and my thesis supervisor, influenced both my professional and personal lives with his genuine enthusiasm and lasting optimism that I always appreciate. I am also grateful for his guidance and dedication in reading and correcting all the manuscripts with patience to improve my scientific skills. Without his continuous motivation, this work could never have been completed. Prof. Blu, my thesis co-supervisor, always impressed me with his ceaseless motivation for research and teaching. I would like to thank him for sharing me part of his tremendous mathematical knowledge and enthusiasm. I also want to thank him and his wife, Sybil Chan, for the hospitality during my stay in Hong Kong.

Next, I would like to thank to my thesis committee, Prof. Yue M. Lu, Prof. Aleksandra Pizurica and Prof. Pascal Frossard, and the jury president Prof. Jean-Philippe Thiran, for their insightful comments and suggestions to improve my thesis. Moreover, I am grateful to Jeff, Giulia, Djalel and Gürkan for sparing their valuable time for reading, correcting and improving the presentation of the material in this dissertation.

I am thankful to all former and current MIPLab members for providing this very friendly and productive research environment. I owe big thanks to my colleagues Işık , Nora, Jeff, Naghmeh, Thomas, Yuri, Franck, Jonas and Giulia for their companionship; I enjoyed every moment of our stimulating discussions and had a lot of good memories during the conferences. I would like to thank to my colleague Djalel for helping me with the translation of the abstract into French. I thank my students for giving me the opportunity to test myself as supervisor. I would like to thank Ruth Fiaux and human resources department in University of Geneva for their continuous help on my administrative problems.

Next, I would like to thank all my friends in Switzerland for the great moments we had during all these years. I thank to my friends, Emrah Bostan, Arda, Çağrı, Emrah Taş, Eray and Ali Sinan whom I shared the astonishment and joy of my first years in Lausanne during the master studies at EPFL. I also owe big thanks to my friends, Gürkan, Engin, Tuna, Yasemin, Elif, Deniz, Şeniz, Anıl and Gökhan for all the nice memories, dinners, drinks and outings.

Finally, I owe my deepest gratitude to my family, my parents Osman and Yaşar, my brothers Mehmet and Aliihsan for their endless love, patience and sacrifices. Though they are thousands of miles away from me, their continuous encouragement, silent concern and endless love converge to my momentum to work hard and achieve the best I can. Finally, I owe many thanks and gratefulness to my girlfriend, Ash Ercan. Without her support, care and patience, I do not think that I could overcome the difficulties during these years.

Contents

Abstract	i
Résumé	iii
Acknowledgement	vii
1 Introduction	1
1.1 Problem statement	1
1.2 Contributions of the thesis	2
1.3 Organization of the thesis	3
2 The Theory of Finite Rate of Innovation	5
2.1 Introduction	5
2.2 Signals with finite rate of innovation	6
2.3 The FRI framework	7
2.3.1 FRI sampling kernels	8
2.3.2 Mapping signal samples to FRI samples	12
2.3.3 FRI reconstruction methods	14
2.4 Conclusion	18
3 Reconstruction of FRI Signals with Model-Fitting Approach	21
3.1 Introduction	21
3.2 FRI model fitting	22
3.2.1 Constraints on the filter coefficients	25
3.2.2 FRI with model fitting algorithm	26
3.2.3 Model order selection	27
3.3 Results	28
3.3.1 Comparison of FRI algorithms	29
3.3.2 Model order selection	33
3.4 Summary	35
4 Detection of Spontaneous Brain Activity in fMRI Using FRI	37
4.1 Introduction	37
4.2 Functional magnetic resonance imaging	38
4.2.1 From MRI to fMRI	38
4.2.2 Hemodynamic response function (HRF)	39
4.2.3 fMRI data analysis and deconvolution frameworks	41
4.3 Finite rate of innovation for fMRI data	42
4.3.1 FRI framework	42
4.3.2 FRI with model-fitting	44
4.3.3 HRF model approximation	45

4.4	Results	46
4.4.1	Simulation results	46
4.4.2	Experimental results	47
4.5	Summary	48
5	FRI for the Inverse Source Problem of Radiating Fields	55
5.1	Introduction	55
5.1.1	Forward problem	56
5.1.2	Inverse source problem	57
5.2	Finite rate of innovation for the Helmholtz equation from boundary measurements	58
5.2.1	Innovation signal for radiating field	58
5.2.2	Sensing kernels	58
5.3	Proof-of-concept validation	63
5.3.1	Sensing step	63
5.3.2	Annihilation step	64
5.3.3	Practical recovery in 3-D	65
5.3.4	Alternative 3-D recovery method	67
5.3.5	Measurement noise and model mismatch	68
5.4	PAT as a potential application	70
5.4.1	Problem setting	70
5.4.2	Results	70
5.5	Outlook	74
5.6	Summary	75
6	Eigensensing Extension for Sparse Source Recovery	77
6.1	Introduction	77
6.2	The problem statement	78
6.3	Eigensensing principle	79
6.3.1	2D image reconstruction	79
6.4	PAT as a potential application	82
6.4.1	Simulation results	83
6.5	Summary	85
7	Conclusion	89
7.1	Summary of findings	89
7.2	Outlook	90
7.3	Concluding remarks	92
A	Appendices	95
A.1	Derivation of CRLB	95
A.2	Training error of the estimator	96
	Bibliography	97
	Curriculum Vitae	108

Chapter 1

Introduction

Sampling and reconstruction are two fundamental operations of signal processing. Implicit and explicit signal representations are at the heart of these essential steps in the processing pipeline. During the past two decades, there has been a significant paradigm shift in signal processing towards the search for efficient sparse signal representations that drastically impact these basic operations. The foremost reason for this paradigm shift is given by the key observation that many naturally-occurring signals can be accurately characterized by some kind of sparse representation. Starting with this discovery, research in signal processing has progressively moved away from its classical formulation based on the use of Fourier transform as the optimal signal representation to uncover powerful alternatives well-adapted to the underlying signal representation. The notion of sparsity, which was initially introduced with the discovery of the wavelet transform, superseded the classical signal processing and became the key development that is until today reshaping the field.

These recent developments consequently brought the need for new sampling and reconstruction strategies that allow for extracting the sparse signal representation while operating at the signal intrinsic information rate. The emerging theories of *compressive sensing* (CS) [1, 2, 3] and *finite rate of innovation* (FRI) [4, 5, 6] deal with the problem of signal reconstruction from a minimal number of samples. On one hand, the CS framework states that it is possible to recover certain types of *discrete-time* signals from a smaller number of samples compared to the traditional methods. On the other hand, the recent development of FRI framework demonstrates that it is possible to design effective sampling and reconstruction schemes for classes of *continuous-time* signals with parametric representations. Interestingly, in both CS and FRI, the signal acquisition remains linear, but at the expense of nonlinear reconstruction algorithms. Hence, there is an increasing interest towards nonlinear methods over the classical linear algorithms.

The theory of FRI offers interesting results for the sampling and reconstruction of signals with parametric representation that can accommodate many classes of signals. Even though the FRI theory has evolved considerably since the initial introduction, its potential remains to be fully discovered with accompanying challenges. This is likely due to the fact that the reconstruction of the parameters of an FRI signal is a nonlinear problem and some scenarios are potentially unstable in the presence of noise. Hence, improvement in the stability of the reconstruction is the key to the development of the theory for real applications.

1.1 Problem statement

In this thesis, we present a comprehensive study of the theory of finite rate of innovation and its extension for various applications requiring temporal and spatial localization of sparse events. Localization of sparse innovations in time is a typical problem frequently encountered in parametric signal representation to model streams of Diracs, streams of pulses, piecewise polynomials

and piecewise exponential signals. Regardless of the specific signal representation, the retrieval of the innovation instant is of greatest importance to fully characterize the underlying signal representation. For the first part of the thesis, we consider the reconstruction of sparse signal representations in time, specifically a stream of Diracs, in a typical FRI framework in case of noisy measurements. Within this context, we analyze the reconstruction quality of the spectral estimation methods known to FRI community and we propose a novel reconstruction for FRI using a model-fitting approach. Another challenge in FRI parameter estimation is to estimate the number of innovations from the data. This problem is well-studied in the case when the amount of noise allows to differentiate the signal subspace from the noise contribution. Here, we address the problem of reliable estimation of the number of innovations monitoring the quality of the model-fitting criteria, which is targeted for applications where the measurements are significantly degraded. Hence, we validate the contribution of this approach by means of tailoring the method for the detection of spontaneous brain activity in functional magnetic resonance imaging (fMRI) data.

In the second part of the thesis, we depart from the temporal localization problem of innovations and we consider spatial localization of sparse source representations for inverse source problems from boundary measurements of a radiating field. This model is frequently employed in array signal processing problems where the estimation of the direction of arrival, the localization of the transmitter and the receiver play a key role to sustain a proper communication of signals among different components of the array elements. Furthermore, this model is also useful in visualizing the internal volume in a tomographic imaging geometry where the sparse source distribution is generally used to represent abnormalities in the volume of interest. Despite the importance of the underlying application, the common feature in all these applications is the localization of a point-wise spatial abrupt change from an observation of the secondary field that can be measured at a distance away from the source distribution. Within this context, we extend the FRI framework by means of introducing the so-called sensing principle which is an application of Green's theorem engineered for the Helmholtz equation. We analyze plausible families of sensing kernels that create a link between the boundary measurements and the samples of the source. Then, we develop FRI-inspired parameter retrieval algorithms. Finally, we extend the problem to cover non-parametric source representations for applications where the generating source function follows a continuous model instead of a point source distribution.

1.2 Contributions of the thesis

- **Model-fitting approach to improve FRI reconstruction at low SNR**

We studied the problem of the reconstruction of FRI signal innovations from degraded signal samples. We proposed a novel reconstruction method using a model-fitting approach that is based on minimizing the fitting error subject to an underlying annihilation system given by the Prony's method. We showed that this method outperforms the state-of-the-art FRI reconstruction methods in many regards. First, we demonstrated that FRI recovery with model-fitting reaches the theoretical limit for an unbiased estimator given by the CRLB at low SNR levels. Second, our method provides acceptable results even if the noise level does not allow other FRI methods to function properly due to the involved nonlinear steps. Third, we propose a model order selection framework to determine the number of innovations to estimate. Therefore, this approach introduces a flexibility towards the selection of the model order depending on the noise level.

- **FRI to analyze spontaneous activity in fMRI data**

We have further developed the FRI reconstruction with a model fitting approach to detect spontaneous brain activity in fMRI data. We specifically considered the fMRI data where the measurements are corrupted by a significant amount of noise. We modeled the fMRI time course for every voxel as a convolution between the innovation signal (a stream of

Diracs) and the hemodynamic response function (HRF). We showed that the HRF can be adapted in the FRI framework to satisfy the approximate exponential reproduction. We then validated our work using the fMRI data acquired during an event-related experiment with visual stimuli. The results showed for the first time evidence for the practical usage of FRI for fMRI; i.e., to correctly detect activity in the cuneus region of the visual cortex of the brain. Hence, FRI reconstruction with model-fitting proved to be useful in detection of the activity without prior knowledge of the onsets and the duration of the visual stimuli.

- **FRI to retrieve sparse source distribution**

We addressed the problem of retrieving the parameters of a sparse source distribution (i.e., a 3-D stream of Diracs) from the measurements of the induced radiating field. For this, we introduced the sensing principle as a tool to map the boundary measurements of the field to the measurements of the source distribution with the so-called sensing functions. We proposed several classes of sensing function that allow to extract the information about the source distribution from the boundary measurements of the field through a closed surface integral. In particular, we focused on sensing kernels that are derived from complex polynomials which allow to control the concentration of the sensing kernel on the measurement surface. With this selection, we developed an FRI-driven reconstruction algorithm that allows extractions of the projections of the location of the source function. Then, we showed that using multiple of these projections, it is possible to recover the parameters of the source points. Further, we proposed a modified Cadzow algorithm to compensate for the measurement noise and model mismatch.

- **Eigensing principle and partial Fourier measurements**

We developed a novel theoretical framework for the inverse source problem of radiating field by generalizing the sensing principle. We addressed that spatial eigenfunctions of the Laplace operator are a subset of the sensing functions developed for the localization of sparse source distributions. Hence, we showed that using these eigenfunctions as the new sensing kernels allow the mapping from the boundary measurements to partial Fourier measurements of the source function. With this extension, we have shown that we computationally obtain several images of the source function, each corresponding to mutually exclusive Fourier measurements of the unknown source function. Finally, we developed a joint deconvolution framework to reconstruct the source function from these intermediate images. Hence, the results confirmed that the eigensing framework achieves the recovery of the source function from the boundary measurements without an explicit forward model.

1.3 Organization of the thesis

The outline of the thesis is as follows. In Chapter 2, we review the theory of finite rate of innovation displaying the steps of the complete framework from signal acquisition to reconstruction. We provide various sampling strategies and mainly focus on the reconstruction schemes in the presence of noise. In Chapter 3, we propose a novel FRI reconstruction based on a model-fitting approach. In particular, we propose to minimize the error between the computed and the recovered samples subject to the annihilation system. We show that it is a particular case of structured total least squares problem and we develop it for the recovery of the FRI parameters. Moreover, we propose a model order selection framework to determine the number of innovations to estimate using the estimation quality of the data as a measure. In Chapter 4, we further extend the model fitting approach for the analysis of time series in fMRI data. In particular, we aim at detecting spontaneous brain activity and further analysis of the fMRI data without a priori known temporal regressor. Starting from Chapter 5, we move to the extension of the FRI for the inverse source problems of radiating fields governed by the wave equation. We

further demonstrated that this framework can be used in a potential tomography application. In Chapter 6, we provide an extension of the sensing principle to recover continuously defined source functions in radiating fields. We show that the proposed sensing kernels in this case allow to extract partial Fourier measurements of the source function. Then, we propose a joint deconvolution algorithm using these partial Fourier measurements and we use the total variation as a measure of smoothness to regularize the solution. Finally, in chapter 7, we conclude with a summary of our findings with some related discussion and outlook.

Chapter 2

The Theory of Finite Rate of Innovation

2.1 Introduction

Sampling is an essential step in digital signal processing to convert a continuous-time signal into a discrete-time one. Over the past 60 years, the sampling process is predominantly based on the well-known Shannon sampling theorem that states uniform samples of a bandlimited (BL) signal at the Nyquist rate (i.e., at least twice of the bandwidth) are sufficient to perfectly reconstruct the signal [7, 8]. For any BL-signal, the signal's Fourier transform is zero above a certain finite frequency that determines the bandwidth. Consequently, for any signal bandlimited to $[-\frac{B}{2}, \frac{B}{2}]$, the reconstruction formula is given as a linear interpolation of the discrete samples with a sinc function,

$$x(t) = \sum_{n \in \mathbb{Z}} x_n \text{sinc}(Bt - n), \quad (2.1)$$

where $x_n = \langle x(t), \text{sinc}(Bt - n) \rangle = x(n/B)$. We may also state that the signal $x(t)$ has B degrees of freedom per second, since $x(t)$ is exactly defined by a sequence of samples $\{x_n\}_{n \in \mathbb{Z}}$, spaced $T = 1/B$ seconds apart, given that the basis function (i.e., the sinc) is known [6]. Equivalently, the BL-signal $x(t)$ is said to have a *finite rate of innovation*, denoted $\rho = B$.

This idea can be generalized to space of shift-invariant signals by replacing the sinc function with a known function ϕ . Specifically, consider the signal of the form

$$x(t) = \sum_{n \in \mathbb{Z}} c_n \phi\left(\frac{t}{T} - n\right), \quad (2.2)$$

which is not necessarily bandlimited, yet still has a rate of innovation $\rho = 1/T$ [8]. Note that now c_n is the discrete representation of $x(t)$ in the approximation space defined by the linear combination of integer-shifted functions ϕ [8, 9, 10]. There are many examples of such signals, for example when ϕ is a scaling function in multiresolution wavelet framework [11, 12] and in approximation theory [13, 14].

Further generalization of the above case appears when we allow arbitrary shifts in the signal representation

$$x(t) = \sum_{n \in \mathbb{Z}} c_n \phi\left(\frac{t}{T} - t_n\right), \quad (2.3)$$

where the only degrees of freedom in (2.3) are the innovation instants t_n and the innovation weights c_n ; i.e., the innovation rate is now twice the one of the representation in (2.2). Note that this class of signals no longer belongs to a single subspace, but rather a union of subspaces [15].

Indeed, consider the case where the innovation instants are known and the innovation weights are unknown, then the signal belongs to a linear subspace spanned by $\{\phi(\frac{t}{T} - t_n)\}_{n \in \mathbb{Z}}$. Hence, the set of all possible signals in (2.3) constitutes a union of subspaces, each of which corresponds to a set of possible shifts $\{t_n\}_{n \in \mathbb{Z}}$. The estimation of this type of signals is clearly a non-linear problem, and hence classical sampling theory does not hold anymore.

The natural question to raise is the following. Is there any sampling and reconstruction framework that covers this type of sparse signal representations? As it turns out, the answer is yes. The theory of finite rate of innovation (FRI), initially introduced by Vetterli et al. in 2002 [4], has shown that it is possible to develop exact sampling and reconstruction schemes for specific classes of signals that are neither BL nor belong to a fixed subspace, but belong to a union of subspaces [6, 4, 5, 16]. In this chapter we provide a background on the theory of finite rate of innovation.

2.2 Signals with finite rate of innovation

The notion of FRI is closely linked with parametric signal representation. In this case, a parametric signal can be seen as an FRI signal, if the signal model depends on finitely many parameters. More formally, consider a signal of the form:

$$x(t) = \sum_{n \in \mathbb{Z}} \sum_{r=0}^{R-1} \gamma_{n,r} g_r(t - t_n), \quad (2.4)$$

where $\{g_r(t)\}_{r=0, \dots, R-1}$ is a set of known functions. In this respect, it is clear that the only degrees of freedom in the signal are the innovation instants t_k , and the innovation weights $\gamma_{n,r}$. Hence, the signal $x(t)$ is defined as an FRI signal, if the number of signal innovations is finite per unit time [4, 5]. More precisely, introducing a counting function $C_x(t_a, t_b)$ that counts the number of free parameters in $x(t)$ over the interval $[t_a, t_b]$, the rate of innovation of the signal $x(t)$, is defined as [4, 5]:

$$\rho = \lim_{\tau \rightarrow \infty} \frac{1}{\tau} C_x\left(-\frac{\tau}{2}, \frac{\tau}{2}\right). \quad (2.5)$$

We further define a local rate of innovation with respect to a moving window size τ for finite length or periodic signals. In this case, the local rate of innovation at time t is given by [4, 5]:

$$\rho_\tau(t) = \frac{1}{\tau} C_x\left(t - \frac{\tau}{2}, t + \frac{\tau}{2}\right). \quad (2.6)$$

which clearly tends to ρ as τ tends to infinity. As it will become clear later, the local rate of innovation plays a more important role than the global rate of innovation, since the reconstruction schemes are local in general.

Examples of such FRI signals are streams of Diracs, streams of short pulses (with known pulse shape) [16, 17], uniform and non-uniform splines, piecewise polynomials and sinusoidal signals [5, 18], etc. In Figure 2.1, we illustrate some of these FRI signals. All these examples are uniquely characterized by a set of signal innovations, namely the innovation instants and the innovations weights. Consequently, a stream of Diracs is generally considered as a prototypical FRI signal. Hence, we consider a set of signal innovations $\{t_k, a_k\}_{k=0}^{K-1}$ that generates a signal characterized by a parametric representation of the form

$$x(t) = \sum_{k=0}^{K-1} a_k \delta(t - t_k). \quad (2.7)$$

The only degrees of freedom in the signal are the number of innovations K , the innovation instants t_k , and the innovation weights a_k . Despite the simple representation as a train of Diracs, it serves

as a prototypical example of the FRI signal. This representation has $2K$ degrees of freedom and indicates the innovative part of an FRI signal that is the foundation for other types of FRI signals. For example, a *stream of pulses* can be easily derived from (2.7) simply by replacing the Dirac shape by a known pulse shape [16].

Another example is the *nonuniform spline* of degree R with weights $\{a_k\}_{k=0}^{K-1}$ and knots $\{t_k\}_{k=0}^{K-1}$ where the $(R+1)$ th derivative is a stream of Diracs (2.7). Hence, a nonuniform spline of order R consists of $K+1$ segments with K transitions, each of which is a polynomial of degree R , such that the signal is continuously differentiable $R-1$ times. Consequently, the $(R+1)$ th derivative converts the signal into a stream of K weighted Diracs, which again has $2K$ degrees of freedom [4].

Similar to the nonuniform spline, a *piecewise polynomial* consists of K segments of maximum degree R such that $(R+1)$ th derivative converts the signal into a stream of differentiated Diracs, that is given by $x^{R+1}(t) = \sum_{k=0}^{K-1} \sum_{r=0}^R a_{k,r} \delta^{(r)}(t - t_k)$.¹ In this case, the signal has $K(R+2)$ degrees of freedom in total with K from innovation instants and $(R+1)K$ from the innovation weights. Note that the difference with the nonuniform spline is that the piecewise polynomial is not differentiable at the knots.

Finally, it is possible to extend (2.7) to higher dimensions [19]. In this case, a stream of Diracs can be written as

$$x(\mathbf{r}) = \sum_{k=0}^{K-1} a_k \delta(\mathbf{r} - \mathbf{r}_k), \quad (2.8)$$

where $\mathbf{r}_k \in \mathbb{R}^N$ are the innovation locations and a_k are the innovation weights, hence the signal has $(N+1)K$ degrees of freedom. This has been used to model bilevel polygons [19], parametric curves [20], generating dipoles in electroencephalography (EEG) [21, 22] and sparse source distribution in radiating waves [23].

2.3 The FRI framework

The FRI acquisition is typically modeled with the standard prefiltering and sampling stages. Hence, the FRI signal is first filtered before being uniformly sampled. This process can be written in terms of an inner product of the input signal with the sampling kernel. The signal samples are then given by

$$y_n = \left\langle x(t), \varphi\left(\frac{t}{T} - n\right) \right\rangle, \quad (2.9)$$

where the sampling kernel, φ , is the scaled and time-reversed version of the filter's impulse response. In fact, the impulse response of the filter accounts for the physical properties of the acquisition device and cannot be modified. Therefore, it is essential to develop sampling schemes that do not impose particular filters.

The FRI framework is depicted in Figure 2.2 with its three essential steps. For the acquisition, various sampling kernels have been proposed such as the infinite-support sinc and Gaussian kernels [4] as well as compact support sampling kernels that satisfy the generalized Strang-Fix condition for reproduction of polynomials and exponentials, i.e., the family of B-splines [5]. Recently, FRI sampling has been further extended to include arbitrary sampling kernels that only satisfy approximate reproduction of exponentials. As a consequence, the limitation on the choice of the sampling kernel has been successfully alleviated [24]. In the second step, namely the mapping, the ability of the sampling kernel to reproduce exponentials plays a central role. For this purpose, the mapping coefficients are first computed imposing the (generalized) Strang-Fix condition to reproduce a set of exponentials. Then, these coefficients are used to combine linearly the signal samples to obtain the FRI samples, which are actually the moments of the

¹The Dirac function is a distribution function whose r th derivative satisfies $\int_{-\infty}^{\infty} f(t) \delta^{(r)}(t - t_0) dt = (-1)^r f^{(r)}(t_0)$, where $f(t)$ is r times continuously differentiable.

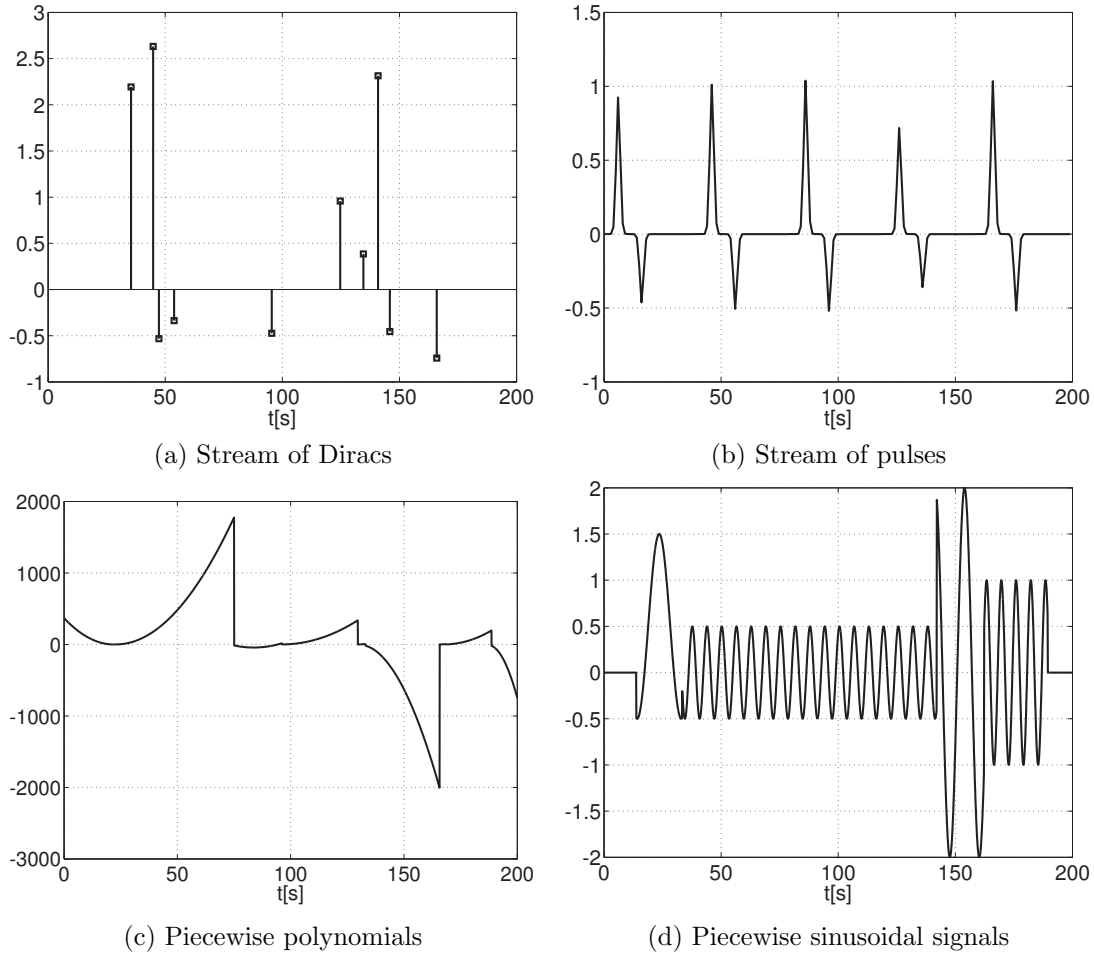


Figure 2.1: Examples of FRI signals; the only degrees of freedom in these signals are the innovation instants and innovation weights.

FRI signal. Hence, the reconstruction is reduced to recovering the signal innovations from these FRI samples that typically reverts to a spectral estimation problem that involves a nonlinear estimation of the innovation instants and a least squares problem for the innovation weights.

2.3.1 FRI sampling kernels

To guarantee exact reconstruction, the FRI sampling kernels are required to satisfy the so-called generalized Strang-Fix conditions [25]. Here, we review the condition for the exponential reproducing kernels that heavily relies on the theory of e-splines [26]. An exponential reproducing kernel is any function $\varphi(t)$ that, together with a linear combination of its shifted versions, can reproduce exponentials of the form

$$\sum_{n \in \mathbb{Z}} c_{m,n} \varphi(t - n) = e^{\alpha_m t}, \quad (2.10)$$

for proper coefficients $c_{m,n}$, and where $\alpha_m \in \mathbb{C}$ and $m = 0, \dots, P$. Specifically, (2.10) holds if and only if the sampling kernel satisfies the generalized Strang-Fix conditions,

$$\widehat{\varphi}(\alpha_m) \neq 0 \text{ and } \widehat{\varphi}(\alpha_m + 2i\pi l) = 0 \text{ for } l \in \mathbb{Z} \setminus \{0\} \quad (2.11)$$

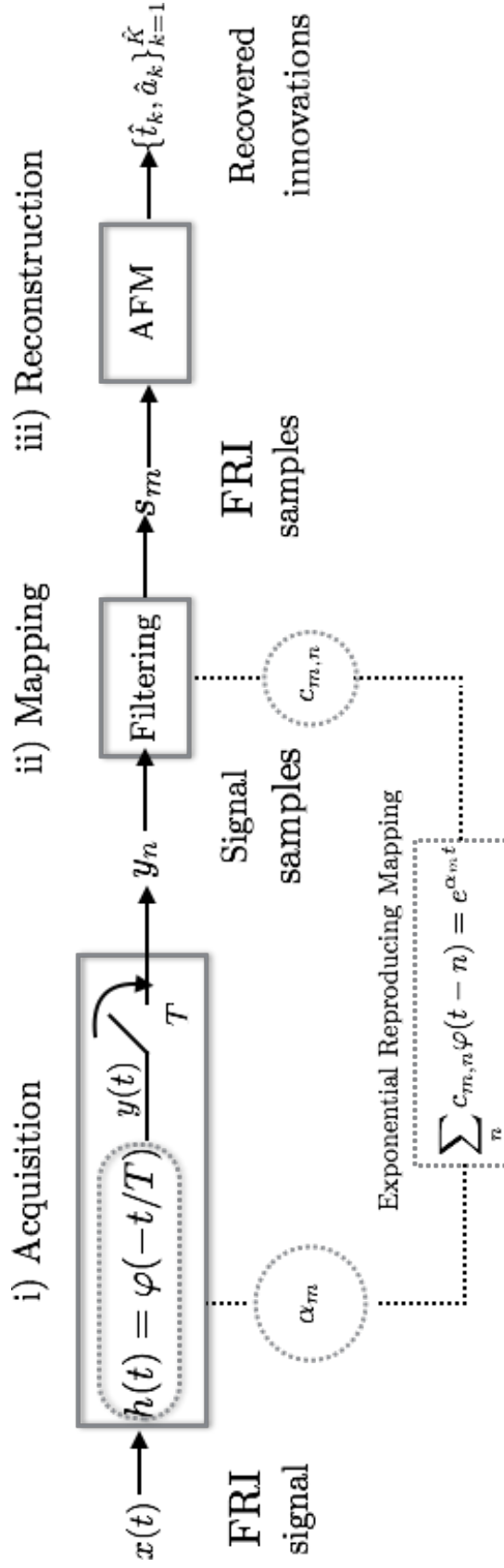


Figure 2.2: FRI framework: The FRI signal is characterized by a finite number of signal innovations, namely innovation instants t_k and innovation weights a_k . i) Acquisition: The FRI-signal $x(t)$ is filtered with a sampling kernel before being uniformly sampled. ii) Mapping: The signal samples are mapped to FRI samples using the coefficients $c_{m,n}$ derived from the information of the sampling kernel. iii) Reconstruction: The signal innovations are recovered from the FRI-samples using a spectral estimation method such as the annihilating filter method.

where $\widehat{\varphi}(\alpha_m)$ represents the bilateral Laplace transform² of $\varphi(t)$ evaluated at α_m . In this case, the coefficients are given by

$$c_{m,n} = \langle e^{\alpha_m t}, \widetilde{\varphi}(t-n) \rangle = e^{\alpha_m n} \widehat{\varphi}(-\alpha_m), \quad (2.12)$$

where $\widetilde{\varphi}(t)$ forms a biorthonormal set with $\varphi(t)$ [5, 9]. One particular case appears when $\widetilde{\varphi}(t)$ is chosen as the dual of $\varphi(t)$. Then, the coefficients are given as

$$c_{m,n} = e^{\alpha_m n} \widehat{\varphi}(\alpha_m)^{(-1)}, \quad (2.13)$$

where $\widehat{\varphi}(\alpha_m)^{(-1)}$ is the Laplace transform of the sampling kernel at α_m [24]. Here, we give an alternative derivation of this result that will pave the way to better understand further extension of FRI sampling kernels.

The dual basis $\{\widetilde{\varphi}(t-k)\}_{k \in \mathbb{Z}}$ can be uniquely determined by the biorthogonality condition [8], i.e., $\langle \widetilde{\varphi}(t-k), \varphi(t-l) \rangle = \delta_{k-l}$. Since, $\widetilde{\varphi}(t)$ must live in the space spanned by φ , we may represent it as

$$\widetilde{\varphi}(t) = \sum_{k \in \mathbb{Z}} p(k) \varphi(t-k) \xleftrightarrow{\text{Fourier}} \widehat{\varphi}(\omega) \widehat{P}(e^{j\omega}), \quad (2.14)$$

where $p(k)$ is a suitable sequence to be determined next. Now consider the biorthogonality condition, and evaluate the inner product

$$\underbrace{\langle \widetilde{\varphi}(t), \varphi(t-k) \rangle}_{\delta_k} = \sum_{l \in \mathbb{Z}} p(l) \langle \varphi(t-l), \varphi(t-k) \rangle \quad (2.15)$$

$$= (p * a_\varphi)(k),$$

where $a_\varphi(k)$ is the autocorrelation sequence defined as $a_\varphi(k) = \langle \varphi(t), \varphi(t-k) \rangle$ with the Fourier transform given as $\widehat{A}_\varphi(e^{j\omega}) = \sum_{k \in \mathbb{Z}} |\widehat{\varphi}(\omega + 2\pi k)|^2$ [8]. Finally, by solving (2.15) in the Fourier domain and using (2.14), we find that

$$\widehat{\varphi}(\omega) = \frac{\widehat{\varphi}(\omega)}{\widehat{A}_\varphi(e^{j\omega})} = \frac{\widehat{\varphi}(\omega)}{\sum_{k \in \mathbb{Z}} |\widehat{\varphi}(\omega + 2\pi k)|^2}. \quad (2.16)$$

Note that, for sampling kernels that satisfy (2.11), the last identity simplifies into

$$\widehat{\varphi}(\omega) = \frac{1}{\widehat{\varphi}(\omega)^*}, \quad (2.17)$$

which is equivalent to $\widetilde{\varphi}(-\alpha_m) = \widehat{\varphi}(\alpha_m)^{(-1)}$ in Laplace domain from (2.12) and (2.13). Moreover, this identity is also particularly important for sampling kernels that do not satisfy (2.11) exactly, but decays fast enough so that it allows the use of approximate form (2.17) rather than (2.16).

Cardinal Splines

One important example of functions satisfying the generalized Strang-Fix conditions is given by the family of exponential splines [26, 5]. A function with Fourier transform

$$\widehat{\beta}_\alpha(\omega) = \frac{1 - e^{\alpha - j\omega}}{j\omega - \alpha} \quad (2.18)$$

is called an E-spline of first order with $\alpha \in \mathbb{C}$. In the time domain, the expression of an E-spline of first order is given as:

$$\beta_\alpha(t) = \begin{cases} e^{\alpha t} & 0 \leq t < 1 \\ 0 & \text{otherwise} \end{cases}. \quad (2.19)$$

²The bilateral Laplace transform is defined as: $\widehat{\varphi}(s) = \int_{-\infty}^{\infty} e^{-st} \varphi(t) dt$ where $s \in \mathbb{C}$.

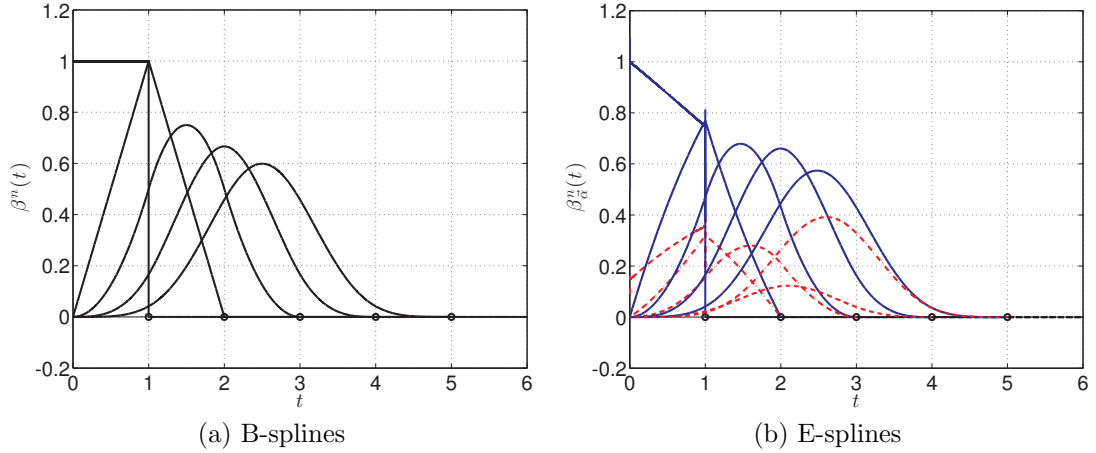


Figure 2.3: Examples of cardinal splines (a) B-splines, $\beta^n(t)$, of degree $n = 0$ to 4, (b) E-splines, $\beta_{\vec{\alpha}}^n(t)$ of degree 0 to 4 with $\vec{\alpha} = [-0.2 + 0.3i, -0.2 + 0.1i, 0.3, 0.1 - 0.2i, 0.2 + 0.4i]$; the solid blue and dashed red lines show the real and the imaginary parts of the E-splines, respectively.

Therefore, the function $\beta_{\vec{\alpha}}(t)$ is of compact support and linear combinations of its shifted versions reproduce the exponential $e^{\alpha t}$. Then, an E-spline of order $P + 1$ is obtained by successive convolutions of lower-order ones, and given by the following Fourier transform

$$\hat{\beta}_{\vec{\alpha}}(\omega) = \prod_{m=0}^P \frac{1 - e^{\alpha_m j \omega}}{j \omega - \alpha_m}, \quad (2.20)$$

where $\vec{\alpha} = (\alpha_0, \alpha_1, \dots, \alpha_P)$. The resulting E-spline is again of compact support $P + 1$ and can reproduce any exponentials in the subspace spanned by $\{e^{\alpha_0 t}, e^{\alpha_1 t}, \dots, e^{\alpha_P t}\}$ [26]. Moreover, since the exponential reproduction property is preserved through the convolution, any composite function of the form $\gamma(t) * \beta_{\vec{\alpha}}(t)$ is also able to reproduce the same set of exponentials.

Notice that the family of E-splines is a generalization of that of B-splines, in that when $\alpha_m = 0$ for $m = 0, \dots, P$, the function $\beta_{\vec{\alpha}}(t)$ reduces to a B-spline satisfying the so-called Strang-Fix conditions [25]. Consequently, they no longer reproduce exponentials but polynomials up to order P [13]. In particular, the family of B-splines is a subset of plausible FRI sampling kernels that are known as polynomial reproducing kernels in the FRI framework [5]. Figure 2.3 (a) and (b) show examples of cardinal B-splines and E-splines of order 1 to 5, respectively.

Approximate reproduction of exponentials

Typically, the impulse response of the filter accounts for the physical properties of the acquisition device and cannot be modified. Therefore, it is essential to develop sampling schemes that do not require the use of particular kernels. However, these limitations on the choice of the sampling kernels can be removed by relaxing the exact exponential reproduction requirement [24, 17].

The generalized Strang-Fix conditions of (2.11) impose restrictive constraints on the choice of the sampling kernel. In particular, the first part of the conditions, that is $\hat{\varphi}(\alpha_m) \neq 0$ is easy to achieve, but it is harder to guarantee the second part, i.e., $\hat{\varphi}(\alpha_m + 2i\pi l) = 0$ for $l \in \mathbb{Z} \setminus \{0\}$, when we do not have control on the acquisition device. In this case, since the sampling kernel does not satisfy the generalized Strang-Fix condition, the exponential reproduction property in

(2.10) cannot be satisfied exactly, and it becomes an approximation problem

$$\sum_{n \in \mathbb{Z}} c_{m,n} \varphi(t-n) \simeq e^{\alpha_m t}, \quad (2.21)$$

with the coefficient $c_{m,n}$ to be determined based on a type of approximation. We first note that the coefficients $c_{m,n}$ are discrete exponentials as in (2.12) such that $c_{m,n} = c_{m,0} e^{\alpha_m n}$. In general $\varphi(t)$ can be any function and we can find different sets of coefficients such that $\varphi(t)$ is used to approximate a given exponential. Initially, consider the least-squares approximation of $e^{\alpha_m t}$ in the subspace spanned by $\varphi(t-n)$. Despite the fact that it is not square-integrable, we can still obtain the coefficients $c_{m,n}$ by computing the orthogonal projection [10]. In this case, the coefficients are given by

$$c_{m,n} = \frac{\hat{\varphi}(-\alpha_m)}{\hat{a}_\varphi(e^{\alpha_m})} e^{\alpha_m n}, \quad (2.22)$$

where \hat{a}_φ is the same autocorrelation function defined in (2.15). Here, the least-squares approximation requires exact knowledge of $\varphi(t)$. However, if the sampling kernel decays sufficiently fast, we can assume that the terms $\hat{\varphi}(\alpha + i2\pi l)$ for $l \in \mathbb{Z} \setminus \{0\}$ are small enough so that we can approximate it with only the first term. Hence, the coefficients for the constant least-squares are given by [24]

$$c_{m,n} = \frac{e^{\alpha_m n}}{\hat{\varphi}(\alpha_m)}. \quad (2.23)$$

Moreover, there are further alternatives to the type of approximation and the selection of the coefficients for arbitrary sampling kernels in FRI. Hence, with this extension³, the limitations on the choice of the sampling kernels have been successfully removed.

Finally, we return to the exponential reproduction property of the sampling kernel given by (2.10) for compact support (or truncated) kernels. Despite the initial examples of FRI sampling kernels, the infinite support sinc and Gaussian kernels [4], the compact support kernels come with the advantage that the summation in (2.10) can be truncated and still have a range where the exponentials are perfectly reproduced in time. In general, the exponentials $e^{\alpha_m t}$ are perfectly reproduced when the summation is computed for all $n \in \mathbb{Z}$. However, for a compact support (or truncated) sampling kernel, this identity holds for a certain range of interest in time. For example, consider a sampling kernel of compact support L that is $\varphi(t) = 0$ for $t \notin [t_0, t_0 + L)$. In this case, if the summation in (2.10) is truncated to $n = n_0, \dots, n_f$, it follows that the perfect reproduction of the exponential functions holds for $t \in [n_0 + L + t_0 - 1, n_f + 1]$. In Figure 2.4, we illustrate exact reproduction of exponentials with an E-spline sampling kernel defined using pure imaginary exponentials. Here, we can perfectly reproduce 0.2Hz, 0.1Hz and the constant signal exactly for the region of interest specified on each plot. Instead, Figure 2.5 illustrates approximate reproduction of exponentials with a Gaussian sampling kernel. In this case, we note that good approximation of the exponentials in the range of interest is achieved.

2.3.2 Mapping signal samples to FRI samples

Once the signal samples y_n are available through a sampling kernel that satisfies (2.10), the second step in the FRI framework (see Figure 2.2) is to map the signal samples to the FRI samples. This is achieved using the exponential reproducing map of the previous section, i.e., the coefficients $c_{m,n}$ for a set of complex exponentials α_m .

We obtain a new sequence of samples that we name as *FRI samples* hereafter, by linearly combining the signal samples y_n with the coefficients $c_{m,n}$:

$$s_m = \sum_n c_{m,n} y_n. \quad (2.24)$$

³We refer the reader to [24] for a rigorous treatment of the topic and to [8, 27] for further analysis on different types of approximation spaces.

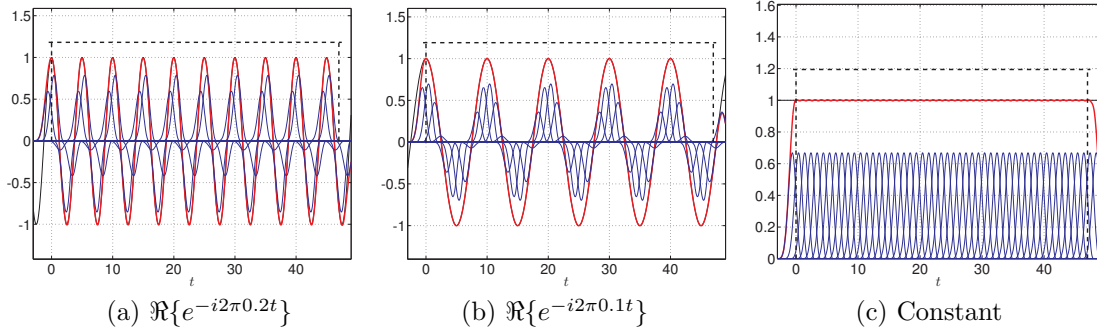


Figure 2.4: Reproduction of exponentials with an E-spline, $\beta_{\vec{\alpha}}(t)$, defined by $\vec{\alpha} = i2\pi[-0.2, -0.1, 0.0, 0.1, 0.2]$. Only the real parts (i.e., \Re) of first three frequencies are illustrated; the thin blue lines represent the shifted and weighted E-splines, the thick red line represents the reproduced exponentials in the range of interest that is given by the black dashed lines above each plot.

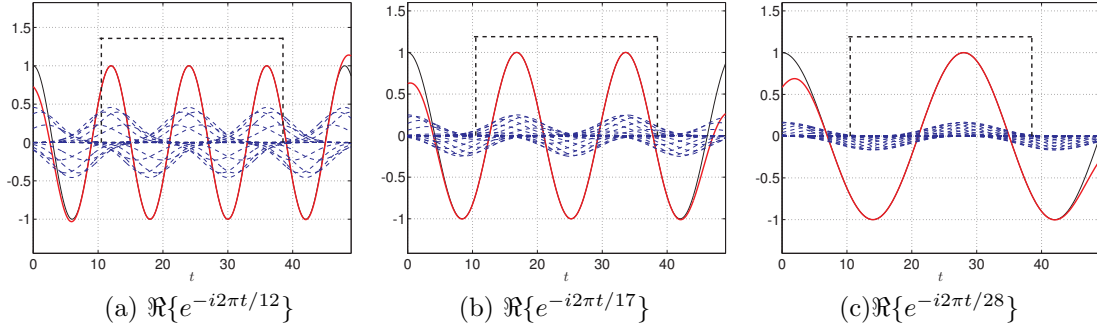


Figure 2.5: Reproduction of exponentials with a Gaussian sampling kernel, $\varphi(t)$, defined by $\sigma_g = 3 * T$. $N=50, T=1$ Only the real parts of first three frequencies are illustrated; the thin blue lines represent the shifted and weighted E-splines, the thick red line represents the reproduction of exponentials in the range of interest that is given by the black dashed lines above each plot.

Then, using (2.9), we have

$$s_m = \sum_n c_{m,n} \left\langle x(t), \varphi\left(\frac{t}{T} - n\right) \right\rangle, \quad (2.25)$$

$$= \left\langle x(t), \sum_n c_{m,n} \varphi\left(\frac{t}{T} - n\right) \right\rangle, \quad (2.26)$$

$$= \left\langle x(t), e^{\alpha_m \frac{t}{T}} \right\rangle, \quad (2.27)$$

which states that the FRI samples are indeed the exponential moments of the FRI signal. Here, we note that any choice of complex exponentials α_m is allowed as long as the corresponding coefficients $c_{m,n}$ are derived from the knowledge of the sampling kernel and the FRI samples will satisfy the line (2.27). However, in the FRI framework, the choice of the exponents is restricted to

$$\alpha_m = \alpha_0 + m\alpha. \quad (2.28)$$

With this choice, the reconstruction problem is converted into a spectral estimation problem, which allows the use of high resolution estimation methods at the reconstruction step.

Finally, using (2.28) and assuming that $x(t)$ being the prototypical FRI signal, i.e., the stream of K Diracs in (2.7), the FRI samples will be

$$s_m = \sum_{k=0}^{K-1} a_k e^{\alpha_m \frac{t_k}{T}}, \quad (2.29)$$

$$= \sum_{k=0}^{K-1} \tilde{a}_k u_k^m, \quad (2.30)$$

where $\tilde{a}_k = a_k e^{\alpha_0 \frac{t_k}{T}}$ and $u_k = e^{\alpha \frac{t_k}{T}}$. Here, we note that the choice $\alpha_m = \alpha_0 + m\alpha$ allows us to write the FRI samples s_m in a power sum form. Moreover, when choosing α_m to be purely imaginary, there exists an ambiguity in obtaining the locations t_k from u_k , since t_k and $t_k + \frac{2\pi T l}{Im(\alpha)}$, for any $l \in \mathbb{Z}$, produces the same annihilating filter roots $u_k = e^{\alpha \frac{t_k}{T} + i2\pi l}$. Hence, it is necessary that $0 \leq t_k < \frac{2\pi T}{Im(\alpha)}$ in order to determine the locations without ambiguity.

2.3.3 FRI reconstruction methods

The mapping step transforms the reconstruction problem of FRI signal into a parameter estimation problem that is similar to spectral estimation. The final step in the FRI framework (see Figure 2.2) is then the recovery of the FRI signal innovations from the extracted FRI samples. In (2.30), we are interested in retrieving \tilde{a}_k and u_k given only s_m for $m = 0, \dots, P$ and the knowledge that they are in a power series form. The signal innovations $\{a_k, t_k\}_{k=0}^{K-1}$ can be retrieved subsequently. Equation (2.30) is common to many problems such as spectral estimation [28, 29] to decompose a signal into a linear mixture of complex exponentials, direction of arrival estimation in array signal processing [30, 31] and polygonal shape estimation from its complex moments [32, 33].

Another challenge for the reconstruction is to estimate the number of exponentials K . Often, this is assumed to be known beforehand. The case with K unknown is a well studied problem and known as the model order selection in statistical estimation to estimate the dimension of the problem [28, 29]. Obviously, this is an inherent step of the estimation problem and might affect the estimation quality. However, for now we assume that K is known unless otherwise stated and we will return to this point in Chapter 3.

Returning back to our problem (2.30), the first solution to the estimation problem was first proposed by Prony in 1795 [34, 29] and is also known as annihilating filter method. To explain Prony's approach, let us first define a filter h with z-transform given by

$$H(z) = \sum_{m=0}^K h_m z^{-m} = h_0 \prod_{k=0}^{K-1} (1 - u_k z^{-1}), \quad (2.31)$$

where the roots corresponds to the values u_k in (2.30). Then, it follows that the convolution of the filter coefficients, h_m with the FRI samples yields an annihilation system

$$\begin{aligned} (h * s)_m &= \sum_{i=0}^K h_i s_{m-i} \\ &= \sum_{k=0}^{K-1} \tilde{a}_k \underbrace{\sum_{i=0}^K h_i u_k^{-i}}_{H(u_k)=0} = 0. \end{aligned} \quad (2.32)$$

$$(2.33)$$

The filter $H(z)$ is called an *annihilating filter* since it annihilates the FRI samples s_m . By construction, the zeros of the filter h uniquely define the values u_k provided that the instants

t_k 's are distinct. To retrieve the coefficients of the filter, (2.32) is written in matrix/vector representation as

$$\mathbf{S}\mathbf{h} = \mathbf{0}, \quad (2.34)$$

where \mathbf{S} is a rank-deficient Toeplitz matrix with $[\mathbf{S}]_{mi} = s_{m-i}$ and \mathbf{h} admits a solution in the nullspace of \mathbf{S} , if $\text{rank}(\mathbf{S}) = K$ for noiseless samples. Explicitly, (2.34) is written in the following form

$$\mathbf{S} = \begin{bmatrix} s_K & s_{K-1} & \cdots & s_0 \\ s_{K+1} & s_K & \cdots & s_1 \\ \vdots & \vdots & \ddots & \vdots \\ s_P & s_{P-1} & \cdots & s_{P-K} \end{bmatrix}, \quad (2.35)$$

which indicates that the matrix is rank deficient and of size $(P - K + 1) \times (K + 1)$.

Once the filter coefficients are found, u_k 's are retrieved as the zeros of the polynomial $H(z)$ from (2.31). Then, given u_k , \tilde{a}_k can be obtained directly from (2.30) by considering K consecutive equations

$$\begin{bmatrix} 1 & 1 & \cdots & 1 \\ u_0 & u_1 & \cdots & u_{K-1} \\ u_0^2 & u_1^2 & \cdots & u_{K-1}^2 \\ \vdots & \vdots & \ddots & \vdots \\ u_0^{K-1} & u_1^{K-1} & \cdots & u_{K-1}^{K-1} \end{bmatrix} \begin{bmatrix} \tilde{a}_0 \\ \tilde{a}_1 \\ \vdots \\ \tilde{a}_{K-1} \end{bmatrix} = \begin{bmatrix} s_0 \\ s_1 \\ \vdots \\ s_{K-1} \end{bmatrix}, \quad (2.36)$$

which is known as a Vandermonde system of equations and leads to a unique solution \tilde{a}_k if the u_k 's are distinct.

Annihilating filter method

In general, the samples in (2.9) are not ideal and degraded by noise,

$$\tilde{y}_n = y_n + \epsilon_n, \quad (2.37)$$

where ϵ_n is assumed to be i.i.d. AWGN, with zero mean and variance, σ^2 . Therefore, the system in (2.34) cannot be satisfied exactly since the FRI samples (2.24) will be also corrupted by noise,

$$\tilde{s}_m = s_m + \tilde{\epsilon}_m, \quad (2.38)$$

where $\tilde{\epsilon}_m$ is the filtered noise given by $\tilde{\epsilon}_m = \sum_n c_{m,n} \epsilon_n$. Hence, the matrix \mathbf{S} is now perturbed by noise

$$\tilde{\mathbf{S}} = \mathbf{S} + \mathbf{E}, \quad (2.39)$$

where the \mathbf{E} is the Toeplitz matrix corresponding to the filtered noise $\tilde{\epsilon}_m$ in (2.38). In [6, 4], the total least-squares (TLS) approach has been proposed to reduce the effect of noise, by minimizing the Euclidean norm $\|\tilde{\mathbf{S}}\mathbf{h}\|^2$ under the constraint that $\|\mathbf{h}\|^2 = 1$. In this case, the solution to \mathbf{h} is the eigenvector that corresponds to the smallest eigenvalue of $\tilde{\mathbf{S}}^H \tilde{\mathbf{S}}$, which can be done by performing the singular-value-decomposition (SVD) [35, 36] of the Toeplitz matrix $\tilde{\mathbf{S}} = \mathbf{U}\mathbf{\Sigma}\mathbf{V}^T$ and choosing the column vector of matrix \mathbf{V} that corresponds to the smallest singular value. The steps of the annihilating filter (AF) method are given in Algorithm 1.

Cadzow denoising algorithm

Another approach to control the effect of noise in the measurements is by studying the rank deficiency property of the matrix \mathbf{S} , which is ideally $\text{rank}(\mathbf{S}) = K$ as stated before. For this purpose, the classical AF method can be improved by denoising $\tilde{\mathbf{S}}$ using the Cadzow denoising

Algorithm 1 Annihilating Filter (AF) Method

Retrieve the parameters of an FRI signal -a stream of K Diracs in (2.7) from the samples in (2.9) taken by an FRI kernel

- 1: Build the system of equations in (2.35) using the FRI samples, s_m
- 2: Retrieve the annihilating filter coefficients h_m by performing an SVD on the Toeplitz matrix $\tilde{\mathbf{S}}$ and choosing the singular vector corresponding to the smallest singular value.
- 3: Compute the roots u_k of the zeros of the filter $H(z)$ (4.8), and retrieve the values of t_k
- 4: Calculate the weights \tilde{a}_k solving the system in (2.36) and obtain a_k

algorithm before applying TLS [6]. Indeed, by only applying the AF method the solution to the problem is suboptimal, since using SVD and keeping the singular vector corresponding to the smallest singular value is equivalent to solve $\tilde{\mathbf{S}}_{\mathbf{K}}\mathbf{h} = \mathbf{0}$ where $\tilde{\mathbf{S}}_{\mathbf{K}}$ is the rank- K approximation of $\tilde{\mathbf{S}}$. This implies that $\tilde{\mathbf{S}}_{\mathbf{K}}$ does not maintain the Toeplitz structure anymore. In fact, this problem is known as the structured low-rank matrix approximation problem and is related to structured total least squares of [37, 38], which we will consider again in Chapter 3 where we propose an FRI reconstruction method based on model-fitting approach.

The algorithm is based on the fact that the matrix $\tilde{\mathbf{S}}$ becomes full rank in the presence of noise. Hence, it can be denoised by iteratively imposing the two properties until convergence. Here, we first replace $\tilde{\mathbf{S}}$ with another Toeplitz matrix $\hat{\mathbf{S}}$

$$\hat{\mathbf{S}} = \begin{bmatrix} s_{\hat{K}} & s_{\hat{K}-1} & \cdots & s_0 \\ s_{\hat{K}+1} & s_{\hat{K}} & \cdots & s_1 \\ \vdots & \vdots & \ddots & \vdots \\ s_P & s_{P-1} & \cdots & s_{P-\hat{K}} \end{bmatrix}, \quad (2.40)$$

assuming that we have $\hat{K} \geq K$ Diracs to allow model mismatch. Note that in this case, the matrix (2.45) is of size $(P - \hat{K} + 1) \times (\hat{K} + 1)$ subject to $P + 1 \geq 2\hat{K} \geq 2K$. Typically, $\hat{\mathbf{S}}$ is full rank due to the noise. Now, if you perform an SVD to $\hat{\mathbf{S}} = U\Delta V^T$, there are $\hat{K} - K + 1$ vectors that form the noise space of $\hat{\mathbf{S}}$. Hence, we first obtain $\hat{\mathbf{S}}_{\mathbf{K}}$, the rank- K approximation of $\hat{\mathbf{S}}$, by keeping the largest singular values and replacing the smallest singular values by zero. Then, we compute the Toeplitz approximation to $\hat{\mathbf{S}}$ by averaging over the diagonals. Iteratively imposing these two conditions, the Cadzow algorithm converges to a rank-reduced Toeplitz matrix [39, 4]. The criterion for the convergence is chosen as the ratio between the K th and the $(K + 1)$ th singular values of $\hat{\mathbf{S}}$ is above a certain threshold. We provide the details of the method in Algorithm 2.

Algorithm 2 AF Method and Cadzow Denoising Algorithm (AF+C)

Retrieve the parameters of an FRI signal -a stream of K Diracs in (2.7) from the samples in (2.9) taken by an FRI kernel

- 1: Calculate the mapping coefficients $c_{m,n}$ as in Section 2.3.1
- 2: Calculate the sequence s_m in (2.24)
- 3: Build the system of equations in (2.45) using the FRI samples, s_m
- 4: Compute the rank-reduced matrix $\hat{\mathbf{S}}_{\mathbf{K}}$
- 5: Compute $\mathbf{S}_{\mathbf{T}}$ the Toeplitz approximation $\hat{\mathbf{S}}$ by averaging over the diagonals and update $\hat{\mathbf{S}}$ with this and repeat from step 4 until an optimlatily criterion is met.
- 6: Retrieve the annihilating filter coefficients h_m by solving the system $\mathbf{S}_{\mathbf{T}}\mathbf{h} = \mathbf{0}$ with AF method of Algorithm 1
- 7: Compute the roots u_k of the zeros of the filter $H(z)$ (4.8), and retrieve the values of t_k
- 8: Calculate the weights \tilde{a}_k solving the system in (2.36) and obtain a_k

Matrix pencil method

Another spectral estimation method used in the FRI framework is the matrix pencil approach [40, 41]. It is based on state space parametrization of a signal subspace [42] that makes use of Hankel matrices and eigendecomposition of certain well-conditioned matrices [43, 42]. The matrix pencil method is a subspace estimator that directly estimates u_k without the need of calculating the annihilating filter coefficients h_k . In this case, we consider the following Hankel matrix constructed by the FRI samples

$$\mathbf{X} = \begin{bmatrix} s_0 & s_1 & \dots & s_{N-1} \\ s_1 & s_2 & \dots & s_N \\ \vdots & \vdots & \ddots & \vdots \\ s_{M-1} & s_M & \dots & s_{M+N-2} \end{bmatrix}, \quad (2.41)$$

where \mathbf{X} is of size $M \times N$ with $M, N > K$. In the absence of noise, \mathbf{X} can be decomposed as $\mathbf{X} = \mathbf{U}\mathbf{A}\mathbf{V}^H$ with the following decomposition:

$$\underbrace{\begin{bmatrix} 1 & 1 & \dots & 1 \\ u_0 & u_1 & \dots & u_{K-1} \\ \vdots & \ddots & & \vdots \\ u_0^{M-1} & u_1^{M-1} & \dots & u_{K-1}^{M-1} \end{bmatrix}}_{\mathbf{U}} \underbrace{\begin{bmatrix} \tilde{a}_0 & 0 & \dots & 0 \\ 0 & \tilde{a}_1 & \dots & 0 \\ \vdots & \vdots & \ddots & \vdots \\ 0 & 0 & \dots & \tilde{a}_{K-1} \end{bmatrix}}_{\mathbf{A}} \underbrace{\begin{bmatrix} 1 & 1 & \dots & 1 \\ u_0 & u_1 & \dots & u_{K-1} \\ \vdots & \ddots & & \vdots \\ u_0^{N-1} & u_1^{N-1} & \dots & u_{K-1}^{N-1} \end{bmatrix}}_{\mathbf{V}^H}^H. \quad (2.42)$$

Here, we note that this factorization is not unique. For example, if $\mathbf{X} = \mathbf{U}\mathbf{A}\mathbf{V}^H$, then $\mathbf{X} = \mathbf{U}\mathbf{P} \cdot \mathbf{P}^{-1}\mathbf{A}\mathbf{Q} \cdot \mathbf{Q}^{-1}\mathbf{V}^H$ is another possible factorization for every choice of $K \times K$ nonsingular matrices \mathbf{P} and \mathbf{Q} . However, any such factorization can be used in the estimation.

The subspace approach makes use of two properties of the data matrix \mathbf{X} . The first property is that the matrix is rank deficient; i.e., ideally $\text{rank}(\mathbf{X}) = K$. Hence, this is used to reduce the amount of noise by approximating \mathbf{X} with a matrix of rank K . The second property is that \mathbf{U} and \mathbf{V} satisfy the shift-invariance subspace property [44], such that the following relations are valid

$$\overline{\mathbf{U}} = \mathbf{U} \cdot \Phi \text{ and } \overline{\mathbf{V}} = \mathbf{V} \cdot \Phi \quad (2.43)$$

where Φ is a $K \times K$ diagonal matrix of entries u_k , and $\overline{(\cdot)}$, (\cdot) denote the operations of omitting the first and the last rows of a given matrix (\cdot) , respectively. Note that the shift-invariance property is also satisfied for $\mathbf{U}\mathbf{P}$ and $\mathbf{V}\mathbf{Q}$ matrices. Specifically, $\overline{\mathbf{U}\mathbf{P}} = \mathbf{U}\mathbf{P}\mathbf{P}^{-1}\Phi\mathbf{P}$ and $\mathbf{U}\mathbf{P} = \mathbf{V}\mathbf{Q}\mathbf{Q}^{-1}\Phi\mathbf{Q}$. Since, $\mathbf{P}^{-1}\Phi\mathbf{P}$ and $\mathbf{Q}^{-1}\Phi\mathbf{Q}$ are related to Φ by a similarity transformation, they have the same eigenvalues as Φ . Therefore, the values u_k can be found from the eigenvalues of an operator that maps $\overline{\mathbf{U}}$ onto \mathbf{U} or $\overline{\mathbf{V}}$ onto \mathbf{V} defined by

$$\mathbf{Z} = \mathbf{U}^+ \overline{\mathbf{U}}. \quad (2.44)$$

We have already mentioned that a key feature of the matrix \mathbf{X} is that it is of rank K . In practice, \mathbf{X} becomes full rank. Hence, in the presence of noise, the components \mathbf{U} and \mathbf{V} will not satisfy the shift-invariance subspace property. Therefore, we find the left and the right singular vector, \mathbf{U}_K and \mathbf{V}_K corresponding to the K largest singular values of \mathbf{X} to construct the operator in (2.44). The details of the method are given in Algorithm 3.

Kumaresan-Tufts Algorithm

Another method developed for estimating the parameters of exponentials is proposed by Kumaresan and Tufts and is based on forward-backward linear prediction (FBLP) filter method

Algorithm 3 Matrix Pencil Method (MP)

Retrieve the parameters of an FRI signal -a stream of K Diracs in (2.7) from the samples in (2.9) taken by an FRI kernel

- 1: Build the system of \mathbf{X} in (2.42) using the FRI samples, s_m
- 2: Compute the singular value decomposition of $\mathbf{X} = \mathbf{U}\mathbf{A}\mathbf{V}^H$
- 3: Find the rank reduced forms, \mathbf{U}_K and \mathbf{V}_K , corresponding to the K largest singular values of \mathbf{X}
- 4: Estimate signal poles u_k by computing the eigenvalues of a matrix $\mathbf{Z} = \underline{\mathbf{U}}_K + \overline{\mathbf{U}}_K$
- 5: Find the values of t_k using the estimated u_k
- 6: Calculate the weights \tilde{a}_k solving the system in (2.36) and obtain a_k

[45, 46]. In this case, the prediction filter is defined assuming that we have L exponentials satisfying $K \leq L \leq P + 1 - \frac{K}{2}$. This way we introduce exactly $L - K$ extraneous zeros of the prediction filter. The algorithm is based on the fact that these extra zeros of the prediction filter are placed inside the unit circle. Using this property, we can choose K zeros of the prediction filter that correspond to the signal subspace. Here, we first construct \mathbf{S}_L using the FRI samples s_m

$$\mathbf{S}_L = \begin{bmatrix} s_L & s_{L-1} & \cdots & s_0 \\ s_{L+1} & s_L & \cdots & s_1 \\ \vdots & \vdots & \ddots & \vdots \\ s_P & s_{P-1} & \cdots & s_{P-L} \end{bmatrix}, \quad (2.45)$$

which is a rank-deficient Toeplitz matrix as before. We define the FBLP filter of order L as

$$\tilde{H}(z) = \sum_{m=0}^L \tilde{h}_m z^{-m}, \quad (2.46)$$

where $\tilde{h}_0 = 1$, and $H(z)$ has $L - K$ extra zeros. Then, we retrieve the FBLP filter coefficients (2.45) as a solution to the system $\mathbf{S}_L \mathbf{h} = \mathbf{0}$ by performing an SVD on \mathbf{S}_L , as in Algorithm 1. Finally, we estimate K out of L zeros that are outside of the unit circle and correspond to the signal subspace. We provide the details of the method in Algorithm 4.

Algorithm 4 Kumaresan-Tufts Algorithm (KT)

Retrieve the parameters of an FRI signal -a stream of K Diracs in (2.7) from the samples in (2.9) taken by an FRI kernel

- 1: Construct the \mathbf{S}_L such that $K \leq L \leq P + 1 - \frac{K}{2}$
- 2: Find the rank reduced forms, \mathbf{S}_{LK}
- 3: Retrieve the FBLP filter coefficients \tilde{h}_m by solving the system $\mathbf{S}_{LK} \mathbf{h} = \mathbf{0}$ with AF method of Algorithm 1
- 4: Compute the roots \tilde{u}_k filter $\tilde{H}(z)$ in(2.46)
- 5: Assign the u_k by picking up K out of L poles outside the unit circle that corresponds to signal space
- 6: Find the values of t_k using the estimated u_k
- 7: Calculate the weights \tilde{a}_k solving the system in (2.36) and obtain a_k

2.4 Conclusion

In this chapter we presented a background on sampling and reconstruction of finite rate of innovation signals. We described the FRI framework in terms of three essential steps, namely

the acquisition, the mapping and the reconstruction. In particular, we explained the importance of the FRI sampling kernels and their exponential reproduction property to map the signal samples into FRI samples. We also gave an overview of the spectral estimation methods that are well-known in the FRI framework.

Chapter 3

Reconstruction of FRI Signals with Model–Fitting Approach

This chapter is based on a submitted paper: Z. Doğan, T. Blu and D. Van De Ville, ‘*Reconstruction of Finite Rate of Innovation Signals with Model–Fitting Approach*’, submitted to IEEE Transactions on Signal Processing.

3.1 Introduction

In the previous chapter we have reviewed the fundamentals of the FRI framework, namely the definition of FRI signals, FRI sampling kernels, and existing FRI reconstruction methods. We have seen that exact recovery of the FRI signal innovations has been demonstrated using various FRI recovery algorithms in the absence of noise such as using the well-known Prony’s method [28]. However, in the presence of noise this method becomes unstable and the accuracy of the reconstruction substantially degrades. Several approaches to improve resilience against measurement noise and model mismatch have been proposed [44, 47, 18]. Further extensions of these approaches have been proposed to improve the performance of the reconstruction in the FRI framework [48, 18, 49, 50]. Yet, the estimation of the signal innovations, which depends nonlinearly on the measurements, remains a challenge for practical applications.

Another challenge that we have already mentioned is the estimation of the innovation rate of the FRI signal, i.e., the number of signal innovations per unit of time. In the statistical estimation framework, this problem is known as the model order selection. In this case, the optimal model minimizes an information criterion with the principle of parsimony that favors simple models over complex ones for equal data fitting quality, e.g., the Bayesian information criterion (BIC), Akaike’s information criterion (AIC), and network information criterion (NIC) [51]. For the FRI framework, this problem is translated in estimating the innovation rate from a set of FRI samples together with the signal innovations. Often, the innovation rate is assumed to be known by the conventional FRI recovery methods and, the standard way to compare the performance of the algorithms, is to check the estimation accuracy of the signal innovations against the Cramér-Rao lower bound CRLB [4, 6, 24]. However, this may not be applicable if the true innovation rate or the true signal innovations are unknown. Hence, there are different approaches to estimate the innovation rate of the signal based on the observation of the separation of the singular values of the system matrix in Cadzow denoising [6, 23] and in the subspace-based methods [18]. However, these methods can only provide a reliable estimation of the innovation rate if the amount of noise permits to clearly differentiate the signal-related singular values from the remaining ones. Moreover, it is still necessary to provide adequate reconstruction that best explains the available data even if the noise level does not allow an accurate estimation of the true innovation rate. In [17], another practical approach is proposed to perform a consistency analysis

of the retrieved innovation instants using a sliding window approach by building a histogram of retrieved locations among different windows.

In this chapter, we propose a novel FRI reconstruction method based on a model-fitting approach. For this purpose, we formulate the nonlinear estimation of the innovation instants as a constrained optimization problem where we minimize the error between the measured FRI samples and the estimated FRI samples subject to the annihilation system. Our contributions are twofold: First, we propose a number of new model-fitting reconstruction methods exploring different constraints applicable to the annihilation system for the estimation of the innovation instants. We show that the problem can be reduced to a simplified version of the structured total least squares (STLS) problem [52]. We then solve a complex least squares problem for the estimation of the innovation weights. Our second contribution is a model order selection to determine the innovation rate of the FRI signal that allows reliable estimation of the signal innovations even at low SNR. The model order selection is based on analyzing the training error curve that reflects the error between the FRI samples and the estimated FRI samples for different model orders.

3.2 FRI model fitting

FRI signals carry a finite number of innovations. For example, consider a stream of K Diracs, which we have already introduced in Chapter 2,

$$x(t) = \sum_{k=0}^{K-1} a_k \delta(t - t_k), \quad (3.1)$$

which is completely determined from $2K$ parameters being the innovation instants t_k and the innovations weights a_k . The performance of the FRI reconstruction methods is measured based on the estimation quality of these parameters. However, this may not be reliable as it depends on the model order K that is an internal parameter of the estimation. In particular, the nonlinear part of the FRI reconstruction, i.e., the localization of these innovations, assumes that the number of Diracs is known beforehand. Moreover, the case with unknown model order inherently deteriorates the estimation quality. Instead, we propose a novel FRI reconstruction method using a model fitting approach based on minimizing the error between the measured FRI samples and the recovered FRI samples. Consequently, this approach allows to define a criterion to monitor the reconstruction quality and adopt the model order accordingly.

The goal of FRI reconstruction methods in Chapter 2 was to first denoise the matrix $\tilde{\mathbf{S}}$ before looking for a solution to the annihilation system in (2.34). As mentioned before, these methods are highly sensitive to noise. Moreover, at low SNR, the estimation of the model order K becomes unreliable. Here, we propose a novel FRI reconstruction to overcome these problems using a model fitting approach based on the structured-TLS (STLS) problem for affinely structured matrices as proposed by De Moor [52]. For this purpose, we first revisit the fundamental concepts of the STLS problem by developing an equivalent formulation for the FRI framework, and then we propose several new FRI reconstructions based on the STLS framework.

Considering the FRI framework, we assume that we have an FRI signal of (3.1) that is sampled with an acquisition device that allows to map the signal samples into FRI samples as in Chapter 2. The following FRI samples are available:

$$s_m = \sum_{k=0}^{K-1} \tilde{a}_k u_k^m, \quad (3.2)$$

where $\tilde{a}_k = a_k e^{\alpha_0 \frac{t_k}{T}}$ and $u_k = e^{\alpha \frac{t_k}{T}}$ and $\alpha_0, \alpha \in \mathbb{C}$ are known by construction of the mapping. Moreover, we also know from Chapter 2 and repeat here for convenience the corresponding

annihilating filter that is necessary to retrieve the innovation locations. The filter h is defined by

$$H(z) = \sum_{m=0}^K h_m z^{-m} = h_0 \prod_{k=0}^{K-1} (1 - u_k z^{-1}), \quad (3.3)$$

where the roots corresponds to the values u_k in (3.2). Finally, the goal of FRI model fitting is to find the parameters of (3.1) using only $(P+1)$ FRI samples s_m for $m = 0, \dots, P$ such that the error between the measured and the recovered FRI samples is minimized. This problem can be reformulated as

$$\min_{\mathbf{s}, \mathbf{h}} \|\tilde{\mathbf{s}} - \mathbf{s}\|^2, \text{ subject to } \mathbf{S}(\mathbf{s})\mathbf{h} = 0 \text{ and } \|\mathbf{h}\|^2 = 1, \quad (3.4)$$

where $\tilde{\mathbf{s}}, \mathbf{s} \in \mathbb{C}^{(P+1) \times 1}$ are the measured and recovered FRI sample vectors, $\mathbf{h} \in \mathbb{R}^{K+1}$ is the filter coefficients vector in (2.31) and $\mathbf{S}(\mathbf{s}) \doteq \sum_{i=0}^K s_i \mathbf{S}_i$ with $\mathbf{S}_i \in \mathbb{C}^{(P+1) \times (K+1)}$ being fixed indicator matrices to represent the Toeplitz structure of \mathbf{S} . Note that we write the matrix \mathbf{S} intentionally as $\mathbf{S}(\mathbf{s})$ to emphasize the linearity of $\mathbf{S}(\mathbf{s})$ with regards to \mathbf{s} . Hence, it is particularly interesting to define the left and the right dual matrices $\mathbf{L}(\cdot)$ and $\mathbf{R}(\cdot)$ of \mathbf{S} for further development.

Lemma 1. *Given the linearity of $\mathbf{S}(\mathbf{s})$ with respect to \mathbf{s} , the left and the right dual matrices $\mathbf{L}(\cdot)$ and $\mathbf{R}(\cdot)$ are defined respectively by*

$$\left. \begin{aligned} \mathbf{g}^H \mathbf{S}(\mathbf{s})\mathbf{h} &= \mathbf{g}^H (\mathbf{R}(\mathbf{h})\mathbf{s}) \\ &= (\mathbf{L}(\mathbf{g})\mathbf{s})^H \mathbf{h} \end{aligned} \right\} \text{ for all } \mathbf{g}, \mathbf{h} \text{ and } \mathbf{s},$$

which yields the following identities

$$\mathbf{S}(\mathbf{s})\mathbf{h} = \mathbf{R}(\mathbf{h})\mathbf{s}, \quad (3.5)$$

$$\mathbf{S}(\mathbf{s})^H \mathbf{g} = \mathbf{L}(\mathbf{g})\mathbf{s}, \quad (3.6)$$

$$\mathbf{L}(\mathbf{g})^H \mathbf{h} = \mathbf{R}(\mathbf{h})^H \mathbf{g}. \quad (3.7)$$

Proof. The first two identities are straightforward. The last one can be obtained from

$$\begin{aligned} \Re\{\mathbf{g}^H \mathbf{S}(\mathbf{s})\mathbf{h}\} &= \Re\{\mathbf{s}^H \mathbf{L}(\mathbf{g})\mathbf{h}\} \\ &= \Re\{\mathbf{g}^H \mathbf{R}(\mathbf{h})\mathbf{s}\} \\ &= \Re\{\mathbf{s}^H \mathbf{R}(\mathbf{h})^H \mathbf{g}\}, \end{aligned}$$

which is satisfied for all \mathbf{s} . □

Theorem 1 (FRI model fitting). *The equations satisfied by the optimal solutions of the problem (3.4) are*

$$\left\{ \begin{aligned} \mathbf{R}(\mathbf{h})^H \mathbf{u} &= \tilde{\mathbf{s}} - \mathbf{s} \\ \mathbf{L}(\mathbf{u})\mathbf{s} &= 0 \\ \mathbf{R}(\mathbf{h})\mathbf{s} &= 0 \\ \|\mathbf{h}\|^2 &= 1 \end{aligned} \right. \quad (3.8)$$

where the unknowns are the $(N-K) \times 1$ vector \mathbf{u} , the $(K+1) \times 1$ vector \mathbf{h} and the $(P+1) \times 1$ vector \mathbf{s} .

Proof. We start by replacing the original problem (3.4) with the following unconstrained minimization problem

$$\min_{\mathbf{s}, \mathbf{h}} \underbrace{\|\tilde{\mathbf{s}} - \mathbf{s}\|^2 + 2\Re\{\mathbf{u}^H \mathbf{S}\mathbf{h}\} + \lambda\{\|\mathbf{h}\|^2 - 1\}}_{\mathcal{L}\{\mathbf{s}, \mathbf{h}, \mathbf{u}, \lambda\}}, \quad (3.9)$$

where \mathcal{L} is the Lagrangian to be minimized, \mathbf{u} is a vector Lagrange multiplier for the constraints $\mathbf{S}(\mathbf{s})\mathbf{h} = 0$ and λ is a scalar Lagrange multiplier for the constraint $\|\mathbf{h}\|^2 = 1$.

The solution is then obtained by setting all the partial derivatives of $\mathcal{L}\{\mathbf{s}, \mathbf{h}, \mathbf{u}, \lambda\}$ with respect to $\mathbf{s}, \mathbf{h}, \mathbf{u}, \lambda$ to 0

$$\begin{aligned}\frac{\partial \mathcal{L}\{\mathbf{s}, \mathbf{h}, \mathbf{u}, \lambda\}}{\partial \mathbf{s}} &= 0 \Leftrightarrow \mathbf{R}(\mathbf{h})^H \mathbf{u} + \mathbf{s} - \tilde{\mathbf{s}} = 0 \\ \frac{\partial \mathcal{L}\{\mathbf{s}, \mathbf{h}, \mathbf{u}, \lambda\}}{\partial \mathbf{h}} &= 0 \Leftrightarrow \mathbf{S}(\mathbf{s})^H \mathbf{u} + \lambda \mathbf{h} = 0 \\ \frac{\partial \mathcal{L}\{\mathbf{s}, \mathbf{h}, \mathbf{u}, \lambda\}}{\partial \mathbf{u}} &= 0 \Leftrightarrow \mathbf{S}(\mathbf{s})\mathbf{h} = 0 \\ \frac{\partial \mathcal{L}\{\mathbf{s}, \mathbf{h}, \mathbf{u}, \lambda\}}{\partial \lambda} &= 0 \Leftrightarrow \|\mathbf{h}\|^2 = 1\end{aligned}$$

Here, the application of the constraints; i.e., the last two lines, shows that $\lambda = 0$. Finally, the use of the duality relations leads to the system of four equations (3.8). \square

The next step of the STLS framework is the elimination of the unknown \mathbf{s} to further reduce the problem to two unknowns. For that, the unknown \mathbf{s} can be readily obtained from the first equation of (3.8), and subsequently replaced in the second and third equations of (3.8). Using the identities from Lemma 1, the optimality equations restricted to the two unknowns \mathbf{u} and \mathbf{h} are

$$\begin{cases} \mathbf{L}(\mathbf{u})\mathbf{L}(\mathbf{u})^H \mathbf{h} - \mathbf{S}(\tilde{\mathbf{s}})^H \mathbf{u} = 0 \\ -\mathbf{S}(\tilde{\mathbf{s}})\mathbf{h} + \mathbf{R}(\mathbf{h})\mathbf{R}(\mathbf{h})^H \mathbf{u} = 0, \\ \|\mathbf{h}\|^2 = 1 \end{cases} \quad (3.10)$$

while the third unknown is given by $\mathbf{s} = \tilde{\mathbf{s}} - \mathbf{R}(\mathbf{h})^H \mathbf{u} = 0$. Note that it is possible to check that

$$\mathbf{D}_{\mathbf{u}} = \mathbf{L}(\mathbf{u})\mathbf{L}(\mathbf{u})^H \text{ and } \mathbf{D}_{\mathbf{h}} = \mathbf{R}(\mathbf{h})\mathbf{R}(\mathbf{h})^H$$

and that

$$\mathbf{u}^H \mathbf{D}_{\mathbf{h}} \mathbf{u} = \|\mathbf{R}(\mathbf{h})^H \mathbf{u}\|^2 = \|\mathbf{L}(\mathbf{u})^H \mathbf{h}\|^2 = \mathbf{h}^H \mathbf{D}_{\mathbf{u}} \mathbf{h}.$$

Hence, by replacing \mathbf{h} with a non-unit vector \mathbf{v} according to $\mathbf{h} = \tau \mathbf{v}$, the system (3.10) is essentially the same as the one in [52] except that, since \mathbf{h} is not normalized anymore, one degree of freedom is left undetermined.

The nonlinear system of equations (3.10) cannot be solved directly for \mathbf{u} and \mathbf{h} , and it is necessary to resort to an iterative procedure where both \mathbf{u} and \mathbf{h} are updated [52]. Here, we propose a simplified alternative being equipped with the analysis of the STLS. We first note that the \mathbf{u} of the Theorem 1 can be readily obtained from the first and the third equations of (3.8)

$$\mathbf{u} = \mathbf{D}_{\mathbf{h}}^{-1} \mathbf{R}(\mathbf{h}) \tilde{\mathbf{s}}. \quad (3.11)$$

Then, using the Lemma 1 and the Theorem 1, we obtain

$$\begin{aligned}\|\tilde{\mathbf{s}} - \mathbf{s}\|^2 &= \|\mathbf{R}(\mathbf{h})^H \mathbf{u}\|^2 \\ &= \|\mathbf{R}(\mathbf{h})^H \mathbf{D}_{\mathbf{h}}^{-1} \mathbf{R}(\mathbf{h}) \tilde{\mathbf{s}}\|^2 \\ &= \tilde{\mathbf{s}}^H \mathbf{R}(\mathbf{h})^H \mathbf{D}_{\mathbf{h}}^{-1} \mathbf{R}(\mathbf{h}) \mathbf{R}(\mathbf{h})^H \mathbf{D}_{\mathbf{h}}^{-1} \mathbf{R}(\mathbf{h}) \tilde{\mathbf{s}} \\ &= \tilde{\mathbf{s}}^H \mathbf{R}(\mathbf{h})^H \mathbf{D}_{\mathbf{h}}^{-1} \mathbf{R}(\mathbf{h}) \tilde{\mathbf{s}} \\ &= \mathbf{h}^H \mathbf{S}(\tilde{\mathbf{s}})^H \mathbf{D}_{\mathbf{h}}^{-1} \mathbf{S}(\tilde{\mathbf{s}}) \mathbf{h}.\end{aligned}$$

Therefore, rather than minimizing (3.10) with respect to \mathbf{u} and \mathbf{h} , we propose to minimize the following quadratic form with respect to \mathbf{h} only,

$$\min_{\mathbf{h}} \mathbf{h}^H \mathbf{S}(\tilde{\mathbf{s}})^H \mathbf{D}_{\mathbf{h}}^{-1} \mathbf{S}(\tilde{\mathbf{s}}) \mathbf{h} \text{ subject to } \mathbf{h} \in \Theta, \quad (3.12)$$

where Θ is a constraint set necessary to avoid the trivial solution. However, since the FRI problem only requires the roots of the polynomial defined by the coefficients \mathbf{h} , neither the solution to this problem is unique nor there exists only one constraint that will lead to the same solution. We will further discuss about the possible conditions on \mathbf{h} and their effect on the solution of the problem later on.

Next, we need to define the operator $\mathbf{R}(\mathbf{h})$ to proceed for the FRI model-fitting framework. Indeed, the dual of the annihilation equation (2.32) can be written using commutativity of the convolution as

$$(s * h)_m = \sum_{i=0}^{N-1} s_i h_{m-i} = 0, \quad (3.13)$$

which can be written in matrix vector form

$$\mathbf{R}(\mathbf{h})\mathbf{s} = \mathbf{0}, \quad (3.14)$$

where \mathbf{R} is a rank-deficient Toeplitz matrix with $[\mathbf{R}]_{mi} = h_{m-i}$. Explicitly, (3.14) is written in the following form

$$\mathbf{R}(\mathbf{h}) = \begin{bmatrix} h_K & h_{K-1} & \dots & h_0 & \dots & \dots & 0 \\ 0 & h_K & \dots & h_1 & h_0 & \dots & 0 \\ \vdots & \vdots & \ddots & \vdots & \vdots & \dots & 0 \\ 0 & \dots & 0 & h_K & \dots & \dots & h_0 \end{bmatrix}, \quad (3.15)$$

which indicates that the matrix is rank deficient and of size $(P - K + 1) \times (P + 1)$.

3.2.1 Constraints on the filter coefficients

In this section, we consider possible cases for the constraint set Θ defined in (3.12) to avoid the trivial zero solution for the filter coefficients \mathbf{h} .

Quadratic norm constraint (MF-1)

We consider a quadratic norm constraint such as $\|\mathbf{h}\|^2 = 1$ for (3.12). We first note that this is an appropriate condition since the coefficients of the filter in (2.31); i.e., h_0, \dots, h_K , can always be scaled by a constant such as $1/\|\mathbf{h}\|$ without altering the roots of the filter. With this condition, we want to minimize

$$\min_{\mathbf{h}} \mathbf{h}^H \mathbf{S}(\tilde{\mathbf{s}})^H \mathbf{D}_{\mathbf{h}}^{-1} \mathbf{S}(\tilde{\mathbf{s}}) \mathbf{h} \text{ subject to } \|\mathbf{h}\|^2 = 1, \quad (3.16)$$

where the term $\mathbf{D}_{\mathbf{h}}$ also depends on \mathbf{h} . Hence, the problem cannot be minimized directly and we propose an iterative scheme, also known as iterative quadratic maximum likelihood (IQML) algorithm [38, 53, 54, 55], assuming that the term $\mathbf{D}_{\mathbf{h}}$ remains constant at each iteration of the solution and that it is obtained using the previous estimate of the solution \mathbf{h} . Hence, the estimation of the filter coefficients is implemented by iteratively solving

$$\min_{\mathbf{h}^{(i)}} \mathbf{h}^{(i)H} \mathbf{S}(\tilde{\mathbf{s}})^H (\mathbf{D}_{\mathbf{h}}^{-1})^{(i-1)} \mathbf{S}(\tilde{\mathbf{s}}) \mathbf{h}^{(i)} \text{ subject to } \|\mathbf{h}^{(i)}\|^2 = 1, \quad (3.17)$$

where $(\mathbf{D}_{\mathbf{h}}^{-1})^{(i-1)} = (\mathbf{R}(\mathbf{h}^{(i-1)})\mathbf{R}(\mathbf{h}^{(i-1)})^H)^{-1}$ and $\mathbf{h}^{(0)}$ is randomly initialized. Then, the solution $\mathbf{h}^{(i)}$ involves finding the eigenvector corresponding to the minimum eigenvalue of $\mathbf{X}_{\mathbf{h}}^{(i)} = \mathbf{S}(\tilde{\mathbf{s}})^H \mathbf{D}_{\mathbf{h}}^{(i-1)} \mathbf{S}(\tilde{\mathbf{s}})$ at each iteration. We name this method as model fitting 1 (MF-1) and provide the details in Algorithm 5.

Linear constraint (MF-2)

We consider a linear constraint such that one element of \mathbf{h} needs to be 1. Specifically, we note that scaling the coefficients of the filter (2.31); i.e., h_0, \dots, h_K with respect to h_K will not alter the roots of the filter. With this condition, we want to minimize

$$\min_{\mathbf{h}} \mathbf{h}^H \mathbf{S}(\tilde{\mathbf{s}})^H \mathbf{D}_{\mathbf{h}}^{-1} \mathbf{S}(\tilde{\mathbf{s}}) \mathbf{h} \text{ subject to } \mathbf{e}_{K+1}^T \mathbf{h} = 1, \quad (3.18)$$

where \mathbf{e}_{K+1} is a length- $(K+1)$ discrete impulse vector with “1” in position $K+1$ and “0” elsewhere. Here the problem cannot be minimized directly and the term $\mathbf{D}_{\mathbf{h}}$ depends on \mathbf{h} . Hence, we propose to use the IQML algorithm [38, 53, 54, 55] assuming the term $\mathbf{D}_{\mathbf{h}}$ remains constant at each iteration. Hence, the estimation of the filter coefficients is implemented by iteratively solving

$$\min_{\mathbf{h}^{(i)}} \mathbf{h}^{(i)H} \mathbf{S}(\tilde{\mathbf{s}})^H (\mathbf{D}_{\mathbf{h}}^{-1})^{(i-1)} \mathbf{S}(\tilde{\mathbf{s}}) \mathbf{h}^{(i)} \text{ subject to } \mathbf{e}_{K+1}^T \mathbf{h} = 1, \quad (3.19)$$

where $(\mathbf{D}_{\mathbf{h}}^{-1})^{(i-1)} = (\mathbf{R}(\mathbf{h}^{(i-1)}) \mathbf{R}(\mathbf{h}^{(i-1)})^H)^{-1}$ and $\mathbf{h}^{(0)}$ is randomly initialized. Then, the solution update is

$$\mathbf{h}^{(i+1)} = \frac{\mathbf{e}_{K+1}^T (\mathbf{X}_{\mathbf{h}}^{(i)})^{-1}}{\mathbf{e}_{K+1}^T (\mathbf{X}_{\mathbf{h}}^{(i)})^{-1} \mathbf{e}_{K+1}}, \quad (3.20)$$

where $\mathbf{X}_{\mathbf{h}}^{(i)} = \mathbf{S}(\tilde{\mathbf{s}})^H \mathbf{D}_{\mathbf{h}}^{(i-1)} \mathbf{S}(\tilde{\mathbf{s}})$ as before. We name this method as model fitting 2 (MF-2) and provide the details in Algorithm 5.

Randomized (linear) constraint (MF-3)

We consider a randomized (linear) constraint based on the randomly initialized solution such that the inner product with \mathbf{h} and the initial estimation remains constant; i.e., $(\mathbf{h}^{(0)})^H \mathbf{h} = 1$. Hence, we want to minimize the following problem

$$\min_{\mathbf{h}} \mathbf{h}^H \mathbf{S}(\tilde{\mathbf{s}})^H \mathbf{D}_{\mathbf{h}}^{-1} \mathbf{S}(\tilde{\mathbf{s}}) \mathbf{h} \text{ subject to } (\mathbf{h}^{(0)})^H \mathbf{h} = 1, \quad (3.21)$$

which cannot be minimized directly since the term $\mathbf{D}_{\mathbf{h}}$ depends on \mathbf{h} . Similarly, we propose to use IQML algorithm [38, 53, 54, 55] assuming the term $\mathbf{D}_{\mathbf{h}}$ remains constant at each iteration. Consequently, the estimation of the filter coefficients is implemented by iteratively solving

$$\min_{\mathbf{h}^{(i)}} \mathbf{h}^{(i)H} \mathbf{S}(\tilde{\mathbf{s}})^H (\mathbf{D}_{\mathbf{h}}^{-1})^{(i-1)} \mathbf{S}(\tilde{\mathbf{s}}) \mathbf{h}^{(i)} \text{ subject to } (\mathbf{h}^{(0)})^H \mathbf{h}^{(i)} = 1, \quad (3.22)$$

where $(\mathbf{D}_{\mathbf{h}}^{-1})^{(i-1)} = (\mathbf{R}(\mathbf{h}^{(i-1)}) \mathbf{R}(\mathbf{h}^{(i-1)})^H)^{-1}$ and $\mathbf{h}^{(0)}$ is randomly initialized. Then, the solution update is given by

$$(\mathbf{h})^{(i+1)} = \frac{(\mathbf{X}_{\mathbf{h}}^{(i)})^{-1} \mathbf{h}^{(0)}}{(\mathbf{h}^{(0)})^H (\mathbf{X}_{\mathbf{h}}^{(i)})^{-1} \mathbf{h}^{(0)}}, \quad (3.23)$$

where we note that the effect of the random initialization will remain (only) in this case due to the imposed constraint. We name this method as model fitting 3 (MF-3) and provide the details in Algorithm 5.

3.2.2 FRI with model fitting algorithm

We propose a full FRI reconstruction algorithm integrating the model fitting approach. Once we have the FRI samples $\tilde{\mathbf{s}}$, we first construct $\mathbf{S}(\tilde{\mathbf{s}})$ and $\mathbf{D}_{\mathbf{h}}$ using randomly initialized $\mathbf{h}^{(0)}$. Then, choosing any of the FRI model fitting approaches (MF-1), (MF-2) or (MF-3), we iteratively obtain the filter coefficients $\mathbf{h}^{(i)}$ to retrieve $u_k^{(i)}$ by finding the roots of the filter in (2.31). We

then obtain the locations $t_k^{(i)}$ using the solution $u_k^{(i)}$, since $u_k = e^{\alpha \frac{t_k}{T}}$ from (4.6). By construction, the zeros of the filter \mathbf{h} uniquely define the values u_k provided that the instants t_k 's are distinct.

In the next step, the amplitudes a_k can be determined either by solving first K consecutive equations of (4.2) or (4.7) with the estimated locations t_k . Specifically, given the locations $t_k^{(i)}$, we determine the amplitudes $a_k^{(i)}$ by solving K consecutive equations of (2.30). Indeed, we propose to minimize the following complex-valued least-squares problem constrained to the real solution

$$\min_{\mathbf{a}^{(i)}} \|\mathbf{B}\mathbf{a}^{(i)} - \mathbf{s}\|^2 \text{ subject to } \mathbf{a}^{(i)} \in \mathbb{R}^{K \times 1}, \quad (3.24)$$

where $\mathbf{B} \in \mathbb{C}^{(P+1) \times K}$ is a complex matrix with entries $[\mathbf{B}]_{mk} = e^{\alpha_m t_k^{(i)}/T}$ and $\mathbf{s} \in \mathbb{C}^{(P+1) \times 1}$ is the complex-moment vector. As a convergence test, we compute the recovered FRI samples as

$$\hat{s}_m^{(i)} = \sum_{k=0}^{K-1} a_k^{(i)} e^{\alpha_m t_k^{(i)}/T} \quad (3.25)$$

and check the numerical convergence by $\frac{\sum_{m=0}^P \hat{s}_m^{(i)} - \hat{s}_m^{(i-1)}}{\sum_{m=0}^P \hat{s}_m^{(i-1)}} \leq \varepsilon$ where ε is a chosen threshold. Although we have no proof of convergence of this algorithm, numerical experiments demonstrate that convergence is typically reached after 10 iterations.

It is important to realize that we look for the convergence in terms of fitting quality in FRI samples, but not in terms of the values of the filter coefficients. One could have chosen the convergence criterion based on the filter coefficients which would not require to extract the parameters of the signal in each iteration. However, we have observed experimentally the first condition converges earlier than the second one, especially with increasing noise levels.

Algorithm 5 FRI model fitting

Require: Inputs: $\tilde{\mathbf{s}}, K > 0$

- 1: **Initialization:** Choose $\mathbf{h}^{(0)}$ and construct \mathbf{D}_h and \mathbf{X}_h
 - 2: **for** $i = 0$ **till convergence do**
 - 3: $\mathbf{h}^{(i)} \leftarrow$ Solution to either (3.16) or (3.18) or (3.21)
 - 4: $u_k^{(i)} \leftarrow$ Find the roots of the filter (2.31)
 - 5: $t_k^{(i)} \leftarrow T/\alpha \ln u_k^{(i)}$
 - 6: $a_k^{(i)} \leftarrow$ Solution to (3.24)
 - 7: $\hat{s}_m^{(i)} \leftarrow$ Recovered FRI samples (3.25)
 - 8: If converged stop, else go to 2
 - 9: **end for**
 - 10: **return** $\{t_k, a_k\}$
-

3.2.3 Model order selection

The estimation of the model order K is a challenging part of all FRI frameworks when the samples are corrupted by noise. Although there exist some methods to estimate the model order, the performance significantly depends on the amount of noise. In this case, current model order estimation methods for FRI fail in particular at low SNR. Here, we propose a novel model order selection procedure that allows us to choose the model number K based on the noise level of the samples.

We start by noting that the annihilation system (4.10) can be solved if we have $(P+1) \geq 2K$ samples of s_m to solve for K innovations; i.e., we need at least as many equations as unknowns. This implies that $(P+1)$ samples can be used to reconstruct at most $\frac{(P+1)}{2}$ innovations. Now, we define the model order selection problem as estimating the optimal model order K , which

can take the values from a discrete set of $\hat{k} = [1, \dots, \frac{(P+1)}{2}]$, for a given $(P+1)$ samples of \tilde{s} degraded by noise. For this purpose, we define a training error of the estimator

$$E_T(\hat{k}) = \|\hat{\mathbf{s}}(\hat{k}) - \tilde{\mathbf{s}}\|_2^2, \quad (3.26)$$

where $\hat{\mathbf{s}}(\hat{k})$ is the recovered FRI sample for model order \hat{k} in (3.25) with the estimated parameters $\{\hat{t}_k, \hat{a}_k\}_{k=1 \dots \hat{k}}$. Notice that the training error curve E_T reveals a U-curve pattern in which the initial drop and final rise regimes represent an under-fitting and over-fitting behavior, respectively, and the flat region in the middle shows the optimal fitting region. We then define the fitting level as the minimum of the training error

$$\hat{\sigma}^2 = \min_{\hat{k}} E_T(\hat{k}), \quad (3.27)$$

which is a good estimator of the input noise level σ^2 for small amounts of noise. Finally, the plausible model order is chosen at the intersection of under-fitting and fitting regions; i.e., it is the minimum \hat{k} that yields the sharpest decrease in the training error and achieves the fitting level in the range $(1 \pm 0.5) \hat{\sigma}^2$. This framework allows to determine the model order based on the SNR level. We refer the reader to Appendix A.2 for a detailed discussion on the training error.

Algorithm 6 FRI model order selection

Require: $\tilde{\mathbf{s}} \in \mathbb{C}^{(P+1) \times 1}$

- 1: **for** $\hat{k} = 1$ to $\frac{(P+1)}{2}$ **do**
 - 2: $\{\hat{t}_k, \hat{a}_k\} \leftarrow$ Apply Algorithm 5
 - 3: $E_T(\hat{k}) \leftarrow$ Find the training error (3.26)
 - 4: **end for**
 - 5: $\hat{\sigma}^2 \leftarrow$ Find the fitting level (3.27)
 - 6: $\bar{k} \leftarrow$ Model order selection (see 3.2.3)
 - 7: **return** $\{K, t_{\bar{k}}, a_{\bar{k}}\}$
-

3.3 Results

We now present various simulation results to validate the proposed approach and demonstrate its practical feasibility. Specifically, we investigate the performance of the FRI model-fitting methods and compare them with the state-of-the-art FRI reconstruction algorithms introduced in Chapter 2. Moreover, we show results for the model order selection framework developed in Section 3.2.3.

We assume that an FRI signal (2.7) with K signal innovations, $\{t_k, a_k\}_{k=0}^{K-1}$, is sampled with a proper FRI kernel that enables to compute the FRI samples. Here, we specifically focus on the reconstruction of FRI signal innovations from FRI samples. Hence, we consider $(P+1)$ FRI samples of

$$\tilde{s}_m = \underbrace{\sum_{k=1}^K a_k e^{i2\pi t_k m}}_{s_m} + \tilde{e}_m, \quad m = 0, \dots, P, \quad (3.28)$$

where $\tilde{e}_m = \tilde{e}_{\mathcal{R}m} + i\tilde{e}_{\mathcal{I}m}$ is complex additive white Gaussian noise with variance σ^2 . The real and the imaginary parts of \tilde{e}_m are uncorrelated and each has a variance of $\sigma^2/2$, i.e., $\tilde{e}_{\mathcal{R}m}, \tilde{e}_{\mathcal{I}m} \sim \mathcal{N}(0, \sigma^2/2)$, so that the covariance matrix of the noise is $\mathbf{R} = \mathbb{E}\{\tilde{\mathbf{e}}\tilde{\mathbf{e}}^H\} = \sigma^2 \mathbf{I}$. The signal-to-noise-ratio (SNR) is defined to be

$$\text{SNR}(\text{dB}) = 10 \log_{10} \frac{\frac{1}{(P+1)} \sum_{m=0}^P (s_m)^2}{\sigma^2}. \quad (3.29)$$

3.3.1 Comparison of FRI algorithms

In the first part, we compare the performance of FRI model-fitting approach combined with one of the three constraints (MF-1 to MF-3) with the most common methods in FRI reconstruction. Among these, the annihilating filter (AF) method and its extension with Cadzow (AF+C) enhancement were the first methods applied to FRI problem [6]. We also added Matrix Pencil (MP) method [40] and Kumaresan-Tufts (KT) algorithm [45] into our comparison [44, 47]. (See Chapter 2 for a review of these spectral estimation methods.)

In the absence of noise, every method is able to recover the signal innovations exactly. However, as noise increases, the accuracy of each method significantly degrades. The FRI signal innovations are generated randomly such that we have K innovation instants between $t_k \in [0, 1]$ with innovation weights $a_k \sim \mathcal{N}(1, 0.1^2)$. Then, we take $(P + 1)$ samples of (3.28) degraded by noise. The variance is chosen to match the target SNR given by (3.29).

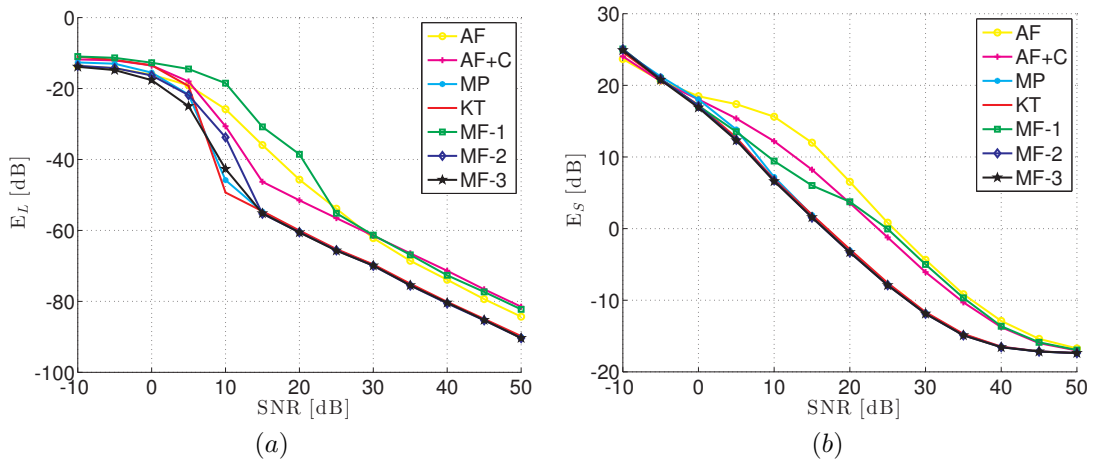


Figure 3.1: Comparison of FRI algorithms: Parameter estimation of a signal with $K=5$ frequencies and $(P + 1) = 4 \times K + 1$ for an average of $N = 1'000$ independent trials: (a) normalized localization error (b) normalized fitting error.

The signal is fully characterized by the innovation parameters: the instants t_1, \dots, t_K and the weights a_1, \dots, a_K . For the numerical experiments, we define two metrics to facilitate comparisons: a normalized localization error in instant estimation, E_L , and a normalized fitting error in FRI samples E_S

$$E_L = 10 \log_{10} \frac{1}{N} \sum_{n=1}^N \frac{\sum_k (\hat{t}_{n,k} - t_k)^2}{\sum_k (t_k)^2}, \quad (3.30)$$

$$E_S = 10 \log_{10} \frac{1}{N} \sum_{n=1}^N \frac{\sum_m (\hat{s}_{n,m} - s_m)^2}{\sum_m (s_m)^2}, \quad (3.31)$$

where $\hat{t}_{n,k}$ are the recovered instants, and $\hat{s}_{n,m}$ are the recovered FRI samples (3.25) in trial n , and N is the total number of independent trials. We further assume that the number of innovations is known and provided to each method so as to make a fair comparison.

We start with an FRI signal of five Diracs with the parameters given as $\mathbf{t} = [0.30, 0.44, 0.56, 0.67, 0.88]^T$ and $\mathbf{a} = [0.914, 0.667, 1.025, 1.058, 0.770]^T$. In Fig. 3.1, we observe the plot of normalized localization and moments error with respect to the SNR level. Clearly, E_L , in Fig. 3.1 (a), exhibits a thresholding effect with respect to SNR level due to the non-linear estimation step. Furthermore, we observe that three of the methods, namely, AF, AF with Cadzow, and

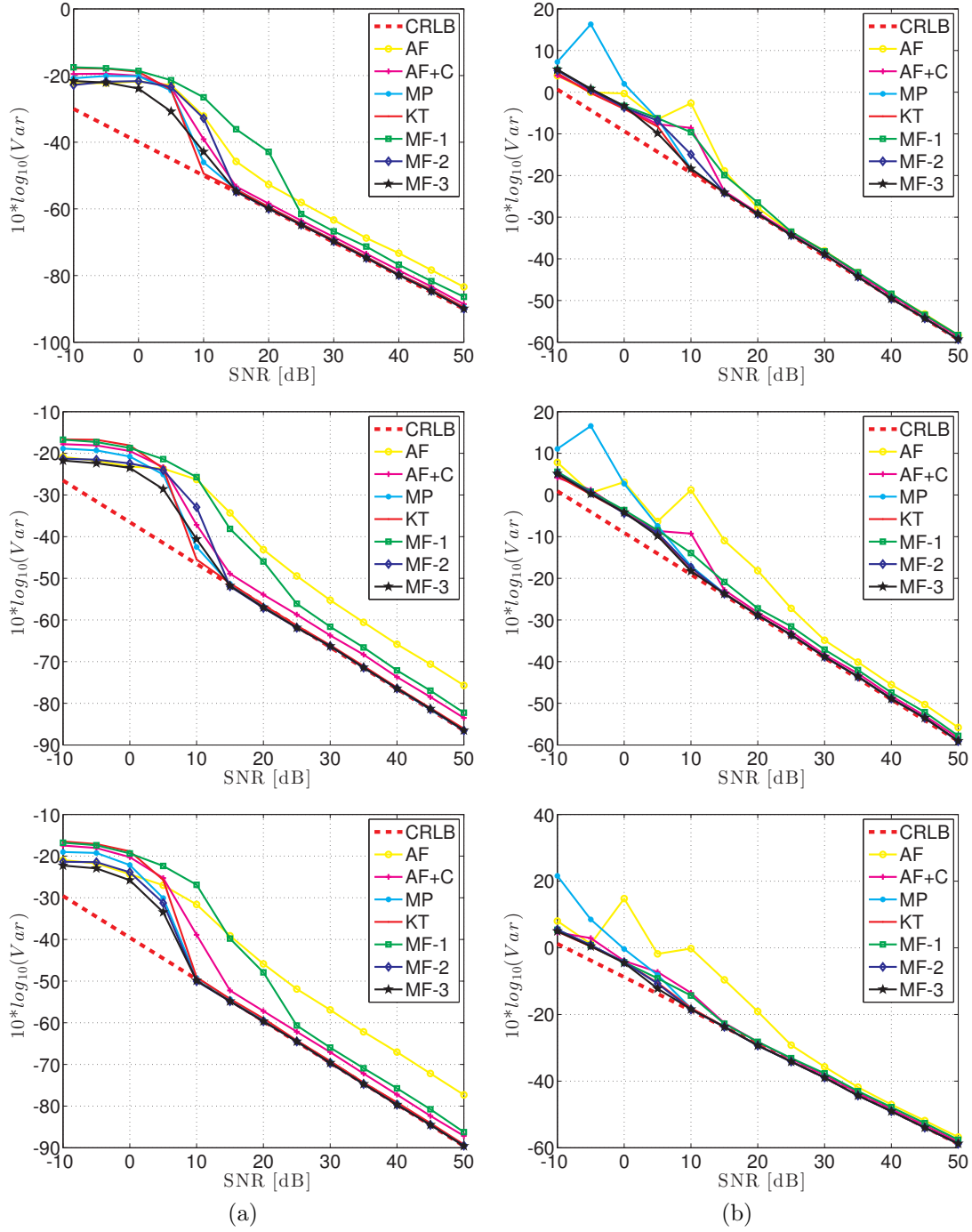


Figure 3.2: Comparison of the performance of FRI algorithms based on estimator variance (Var) and CRLB with respect to each parameter for various SNR levels: Column (a) location parameters t_1, t_2 and t_3 (b) weights a_1, a_2 and a_3 . Parameter estimation of a signal with $K=5$ frequencies and $(P+1) = 4 \times K + 1$ for an average of $N = 1'000$ independent trials.

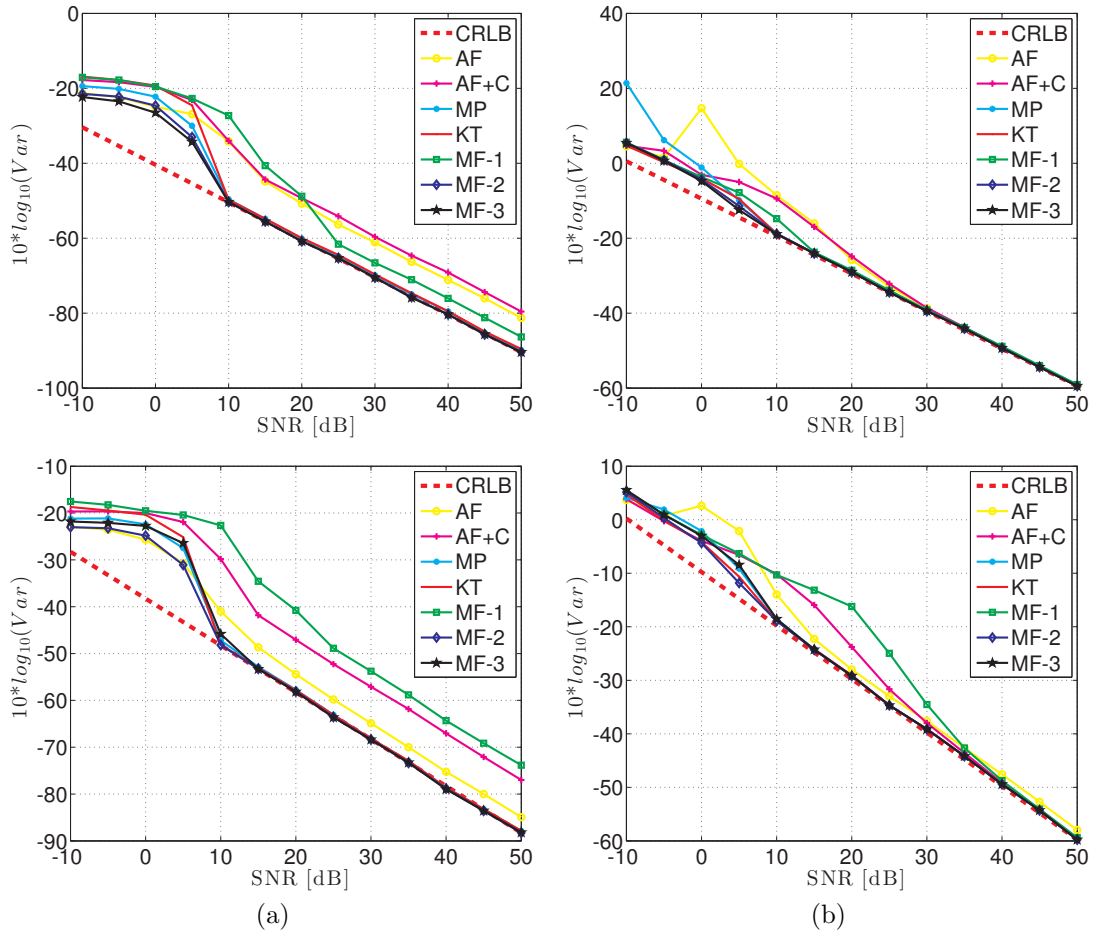


Figure 3.2: (continued) Comparison of the performance of FRI algorithms based on estimator variance (Var) and CRLB with respect to each parameter for various SNR levels: Column (a) location parameters t_4 and t_5 (b) weights a_4 and a_5 . Parameter estimation of a signal with $K=5$ frequencies and $(P+1) = 4 \times K + 1$ for an average of $N = 1'000$ independent trials.

the MF-1, differ in their asymptotic behavior for high SNR. They show significantly poor performance even for high SNR while Cadzow enhancement helps AF method to attain its asymptotic behavior at a lower SNR. In contrast, E_S , in Fig. 3.1 (b), follows a rather smooth curve due to the compensation effect by the estimation of the weights as a solution to the complex least squares problem (3.24).

For the same setting, we now focus on the comparison of the performance of the methods on individual parameters. In Fig. 3.2, we observe the estimator's variance and the theoretical CRLB for each parameter. For the details of the derivation of the CRLB for complex AWGN, we refer the reader to Appendix A.1. Here, we show the observed standard deviation (over $N = 1'000$ independent realizations) compared to CRLB of each parameter. In Fig. 3.2, column (a), we observe the same thresholding effect for the innovation instants that reveals differences for different FRI algorithms. Note that MF-3, the model-fitting approach with randomized linear constraint, performs better for the low SNR and together with MF-2, they achieve the theoretical limit given by the CRLB around 10 dB despite other methods attain this level around 20 dB. In contrast, the weights do not follow a general pattern expressing the compensation behavior of the complex least squares step.

We next provide a different visualization of the innovation instants estimation to better illustrate the interaction between the SNR level, resolution and variance of the estimation. For this purpose, we design a visualization such that each trial of estimation for the innovation instant t_k can be mapped to a point on a ring with a phase given by $2\pi t_k$ and the radius of the ring determines the SNR level, hence termed an SNR bagel. The continuous instant t_k is mapped to $2\pi t_k$ with 1 degree radial resolution and the colorbar shows an average probability of detection for each innovation instant value. In Fig. 3.3, we observe the SNR bagel of the AF method where each ring corresponds to different SNR levels between -10dB to 50dB . For each SNR level, we compute the average over $N = 1'000$ independent realizations. Clearly, the uncertainty of the estimation drops as we move from inside to outside of the SNR bagel. Moreover, we also observe another interpretation of the CRLB, i.e., the varying thickness of the uncertainty cloud. We observe that at low SNR level, the estimations are more spread reflecting the larger variance on the estimation whereas the white narrow regions at high SNR show that the method achieves the minimum variance given by the CRLB. Moreover, we observe the thickness of the uncertainty region changes with respect to the spacing of the two instants which is also another interpretation of the non-diagonal entries the inverse of the Fisher information matrix (A.4) in Appendix A.1.

With this new visualization, we can now look at the Fig. 3.4 and compare the performance of the known FRI reconstruction methods with our FRI model-fitting approach combined with one of the three constraints. We observe that the MF-2, MF-3 and KT methods achieve better performance in the low SNR regime whereas all the methods perform similarly at high SNR. However, MF-1 clearly performs worse than the other two constraints of the model-fitting approach. Hence, we conclude linear constraints for our FRI model-fitting approach perform better than the quadratic constraint.

Next, we compare the FRI algorithms for different model orders K and SNR levels. For this experiment, we consider randomly generating $K = [3, \dots, 10]$ innovations with instants in $t_k \in [0, 1]$ and random weights $a \sim \mathcal{N}(1, 0.1^2)$ using $(P + 1) = 4 \times K + 1$ samples given by (3.28) degraded by complex AWGN as before. In Table 3.1, we compare the performance of all FRI algorithms with respect to normalized localization error in frequency estimation, E_L whereas in Table 3.2 we provide the comparison with respect to normalized FRI sample estimation error E_S . From both tables, we conclude that MF-3 outperforms other algorithms in terms of innovation parameter estimation.

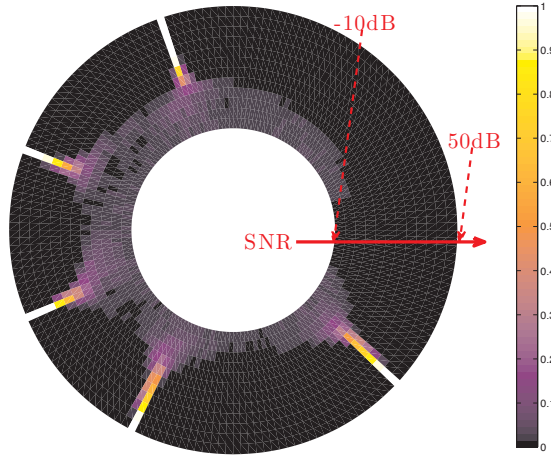


Figure 3.3: SNR bagel: Visualization of frequency estimation for annihilating filter method, where each ring corresponds to a different SNR and the color represents probability of detection for each frequency averaged over $N = 1'000$ realizations.

Table 3.1: Comparison of FRI algorithms for normalized localization error E_L averaged over $N = 1'000$ independent realizations of varying model order $K \in [3, \dots, 10]$.

	SNR(dB)				
	0	5	10	15	20
AF	-17.24	-21.99	-32.84	-41.69	-48.70
AF+C	-14.30	-18.38	-22.37	-26.13	-31.18
MP	-15.95	-22.47	-40.84	-48.13	-52.90
KT	-13.54	-19.19	-36.76	-48.54	-53.13
MF-1	-11.66	-12.99	-14.25	-14.10	-13.91
MF-2	-14.53	-16.20	-18.84	-25.02	-32.71
MF-3	-17.29	-23.36	-42.44	-48.49	-53.83

3.3.2 Model order selection

Several applications of FRI require a robust model order selection as an integral part of the framework. In this section, we demonstrate the feasibility of the model order selection proposed in Section 3.2.3. We first observe the training error curve for the same setting as in the previous part with $K = 5$ frequencies. In Fig. 3.5 (a), we observe the corresponding U-curve; i.e., the training error curve of (3.26), for each SNR level. Using Algorithm 6, we estimate the model order which is given by a gray square on the U-curve (Fig. 3.5 (a)). Clearly, the model order selection algorithm successfully determines the true model order above 10 dB. Moreover, it allows to predict the best model selection for a low SNR-regime, which results in reliable parameter estimation of the FRI signal.

We further extend and demonstrate this SNR level dependent property of the model order selection framework in Fig. 3.5 (b). Here, we consider randomly generating $K = [5, \dots, 10]$ innovations in $t_k = [0, 1]$ with random weights $a \sim \mathcal{N}(1, 0.1^2)$ using $(P+1) = 4 \times K + 1$ samples as before. We observe the average of the model selection over $N = 1'000$ independent trials. From each curve in Fig. 3.5 (b), we clearly observe that the framework chooses a lower model order for low SNR (up to 10 dB) whereas it converges to the true model order for high SNR on the average. We conclude that Algorithm 6 of Section 3.2.3 can be used for reliable estimation of the FRI signal innovations for a range of SNRs.

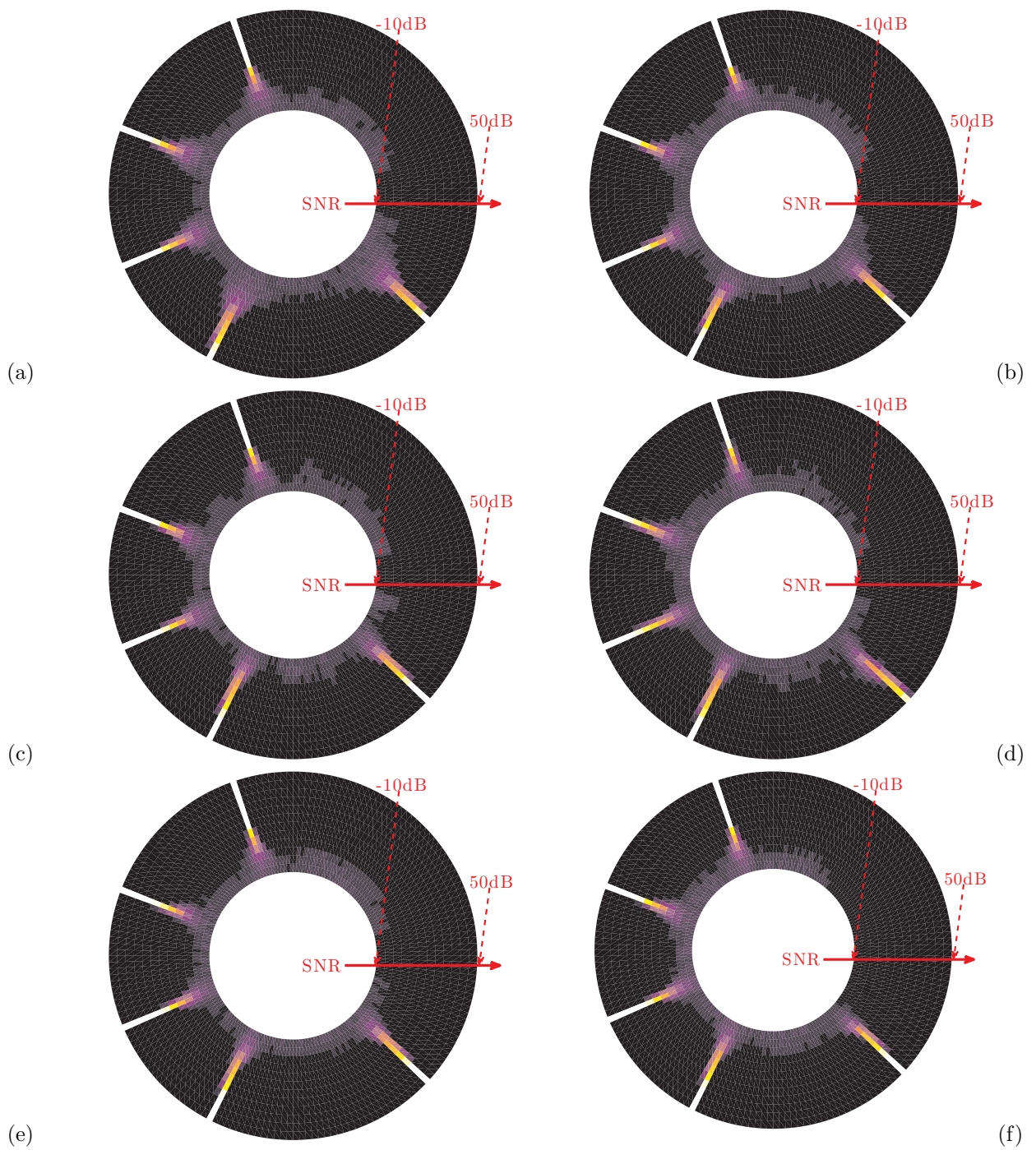


Figure 3.4: Comparison of FRI algorithms on frequency estimation performance mapped to SNR bagel: (a) Annihilating filter + Cadzow (b) Matrix Pencil (c) Kumaresan and Tufts (d) MF-1 (e) MF-2 (f) MF-3.

Table 3.2: Comparison of FRI algorithms for normalized FRI sample error E_S averaged over $N = 1'000$ independent realizations of varying model order $K \in [3, \dots, 10]$.

	SNR(dB)				
	0	5	10	15	20
AF	-0.41	-2.52	-5.77	-10.71	-16.53
AF+C	-0.84	-3.26	-5.70	-7.93	-10.40
MP	-0.65	-4.40	-10.11	-15.91	-20.81
KT	-1.75	-6.17	-11.37	-16.20	-20.94
MF-1	-1.05	-3.96	-6.47	-7.61	-7.98
MF-2	-1.17	-4.42	-8.63	-14.24	-20.11
MF-3	-1.71	-6.35	-11.51	-16.40	-21.36

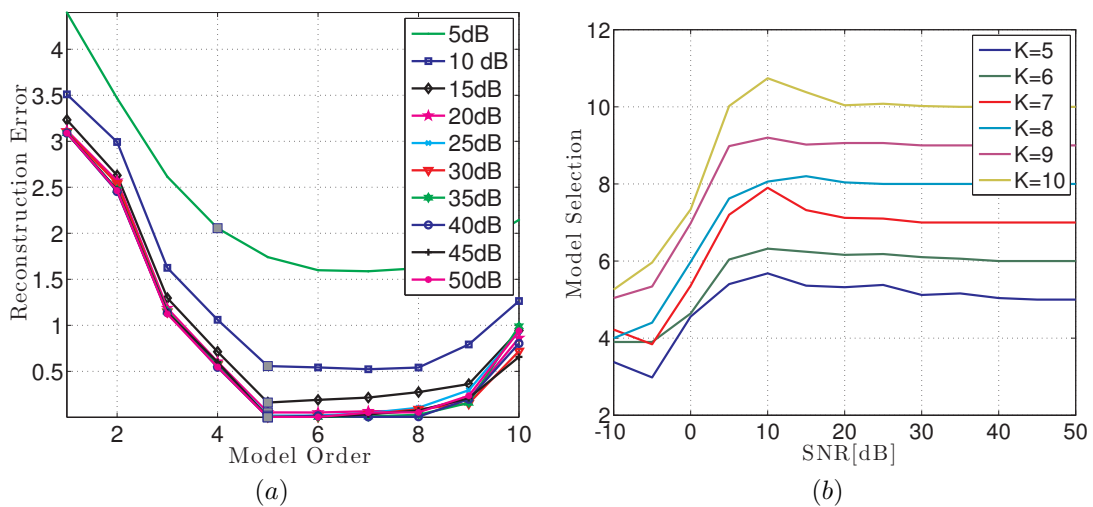


Figure 3.5: FRI model selection: (a) Training error curve at different SNRs for a true model order of $K = 5$, the selected order at each SNR level is given by the gray square (b) Model order selection for different true model order with respect to SNR levels an average of $N = 1'000$ independent trials.

3.4 Summary

We have considered the FRI reconstruction problem in the presence of noise and proposed a novel reconstruction algorithm with a model fitting approach and a novel model order selection framework that allows to estimate innovations even at very low SNR. Numerical results showed that the proposed algorithm with the (randomized) linear constraint outperforms the other FRI reconstruction methods. This new method with model fitting approach would have a potential effect on applications with FRI signal degraded with realistic levels of measurements noise [17, 16, 56].

Chapter 4

Detection of Spontaneous Brain Activity in fMRI Using FRI

Functional magnetic resonance imaging (fMRI) data has rich structure and, therefore, methods that allow better characterization of the brain activity are needed. In particular, resting state fMRI data only contains spontaneous brain activity that cannot be modeled using conventional confirmatory approaches based on linear regression. Our motivation is to further develop the method in Chapter 3 for the detection of spontaneous brain activity in fMRI data using finite rate of innovation (FRI) framework with the model-fitting approach. For this, we represent the fMRI time course for each voxel as a convolution between an innovation signal—a stream of Diracs—and the hemodynamic response function (HRF). First, using an HRF model characterized by a difference of Gaussians, the fMRI samples are mapped to so-called FRI samples. We apply the model-fitting method based on minimizing the error between the measured and the recovered FRI samples. We illustrate the feasibility of our method by showing the detection of the activity signal in simulated data and in experimental data acquired on three subjects during an event-related experiment with visual stimulation unknown to our method.

4.1 Introduction

Functional magnetic resonance imaging (fMRI) plays a central role in modern neuroscience by allowing noninvasive measurement of the brain activity based on the blood oxygenated-level-dependent (BOLD) signal [57]. In conventional fMRI, the analysis is based on stimulus-driven paradigms. Typically, prior knowledge about the experimental paradigm is used to construct temporal regressors, which are then fitted to the time course of every voxel using the general linear model (GLM) method. The analysis is followed by a statistical hypothesis testing for a given contrast weights to relate the experimental paradigm to the fMRI data. In Fig. 4.4, we show a typical fMRI signal model where the BOLD signal of every voxel in fMRI data is represented as a convolution of an activity signal with the hemodynamic response function (HRF). The precise shape of HRF may vary between brain regions and between individuals. There exist various methods accommodating the inter- and intra-subject variability for estimating the shape of the HRF in the literature, e.g., Fourier basis sets, finite impulse response and gamma functions [58, 59].

A temporal regressor of the activity signal cannot be modeled in cases when there is a spontaneous activity, for example, hallucinations in schizophrenia, or interictal discharges in epilepsy. Moreover, analysis of spontaneous brain activity in healthy subjects may provide characteristic patterns of the brain activity referred as resting-state networks [60]. Such spontaneous activity cannot be deduced by standard GLM approaches. Hence, there is an increasing need

for alternative methodologies that enable analysis of fMRI data without predefined responses. fMRI deconvolution methods have been proposed to uncover the underlying activity signal at the fMRI timescale. Within the convolution framework, the linear system assumption is retained while regularization terms are generally used to promote sparsity in the activity signal [61, 62, 63]. Moreover, exploratory methods are essentially employed in extracting information from the fMRI data; e.g., subspace decomposition methods such as independent component analysis (ICA) [64, 65].

In this chapter, we start with an overview of fMRI modality and we propose a novel method to analyze spontaneous brain activity in fMRI data using finite rate of innovation (FRI) framework as initially proposed in our preliminary work [56]. We exploit a new HRF model described by a difference of Gaussians that allows to construct FRI mapping kernels analytically. We propose to use the reconstruction method of Chapter 3 based on a fitting approach to recover the activity signal with respect to the desired level of sensitivity and specificity. We consider the fMRI signal setup as in Fig. 4.4 where the spontaneous activity signal is modeled as an FRI signal – a stream of Diracs with time instants and amplitudes as the innovations of the signal. The FRI fitting method allows to choose varying number of spontaneous events that achieves more flexible analyses of the resting state data.

4.2 Functional magnetic resonance imaging

In this section, we provide an overview of fundamental principles of fMRI data acquisition and analysis. An in-depth overview of the concepts can be found in [66, 67].

4.2.1 From MRI to fMRI

Quantum theory states that each atomic nucleus has specific spin angular momentum which gives rise to a magnetic moment. In the absence of an external magnetic field, these moments are randomly aligned, producing zero net magnetization. However, when placed within a magnetic field, the spins start to align parallel or anti-parallel with respect to the field direction defining the lower and the upper energy levels, respectively. At equilibrium, there is a net magnetization due to slight abundance in the lower energy state, which precesses at the so-called Larmor frequency around the external field direction. In order to measure the magnetization, the equilibrium condition needs to be perturbed by applying polarized magnetic field in the form of RF pulses. In the resonance condition; i.e., when the frequency of the RF pulse is matched to the precession frequency, the net magnetization is effectively tipped into the transverse plane where the magnetization can be measured. This principle is known as nuclear magnetic resonance (NMR) and used extensively in chemical spectroscopy to understand the composition of the substances [68, 69]. The concept of MR image (MRI) became possible only after the discovery that the resonance frequency can be varied as a function of position using additional gradient filters that allow to extract partial Fourier measurements of the screened volume [70, 71].

MRI provides different contrasts, which underpins the success of MRI in clinical applications to demonstrate different anatomical structures or pathologies. MRI contrast is defined based on two intrinsic properties known as the longitudinal and transverse relaxations times of each tissue, denoted as the T1 and T2, respectively. The former is defined as the rate at which the net magnetization will tend to grow back to its equilibrium along the longitudinal axis, whereas the latter is defined as the rate of the decay of the transverse component of the magnetization. Additionally, inhomogeneities in the magnetic field further reduce the transverse relaxation time to T2*. Two important parameters of the MR image formation are the repetition time (TR), which is the elapsed time between successive applications of the RF pulses, and the echo time (TE), which is the elapsed time between the RF excitation and the measurement of the MR signal. Hence, the MR image is formed by choosing appropriate TR, TE and pulse sequences

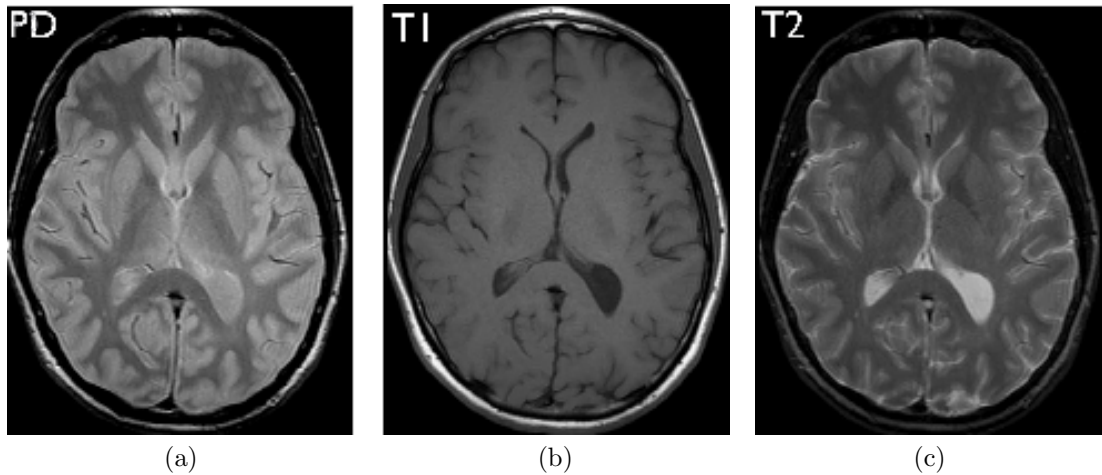


Figure 4.1: Different contrast MR images of the brain. (a) Proton density image shows minimum T1 and T2 effects with long TR and short TE. (b) T1 weighted image shows the white matter with highest contrast. (c) T2 weighted image shows the cerebrospinal fluid and the white matter with highest and lowest intensities, respectively.

such that the images provide maximum contrast of the tissue of interest. Figure 4.1 demonstrates MR images of the brain with three different contrasts.

Functional MRI (fMRI) is a non-invasive modality that measures neural activity based on associated changes in blood flow. In particular, it is based on monitoring the density of hemoglobin (Hb) level as an intrinsic contrast agent through the blood-oxygen-level-dependent (BOLD) response. More specifically, the relationship between the neural activity and the BOLD signal is described by a neurovascular coupling model. Consequently, fMRI indirectly reveals neural activation with hemodynamic changes in the cerebral blood volume (CBV) and blood flow (CBF). Basically, any neural activity increases the consumption of energy and oxygen resulting in an increased demand for nutrients which triggers a vascular response in CBV and CBF. In particular, the BOLD signal measures the ratio of deoxygenated hemoglobin to oxygenated hemoglobin dHb/Hb . The decrease in this ratio causes an increase in the fMRI signal, which can be measured with $(T2-T2^*)$ -weighted imaging. Clearly, the vascular effect brings on over compensation of oxygen leading to an increase in the BOLD signal. Figure 4.2 shows the changes in the dHb/Hb ratio, CBF, CBV and the BOLD. Nevertheless, the actual link between the neural activity and the BOLD signal is not yet completely understood, and is still an active research field [72, 73].

The fMRI data is acquired using $(T2-T2^*)$ -contrasted imaging to maximize the dHb/Hb concentration. The dataset is composed of time series of individual voxels in the brain. The temporal resolution is determined by TR (typically around 1-2 sec) and the spatial resolution depends on the volume of interest (typically the voxel size ranges between $3-10 \text{ mm}^3$ for a whole brain scan that results in $10^4 - 10^5$ voxels in total). The duration of an fMRI data acquisition depends on the type of the experiment (typically 5-20 min), which also imposes a trade-off between the temporal and spatial resolutions.

4.2.2 Hemodynamic response function (HRF)

Many studies have investigated explicit modeling of the BOLD response following a stimulus through linear and nonlinear models. Although some nonlinear aspects of the BOLD have been observed in the literature [74], nonlinear models often limit the fMRI analysis when quantitative comparisons of fMRI responses are needed. Alternatively, linear models have been extensively employed in fMRI data analysis due to their simplicity and ease of data interpretation over

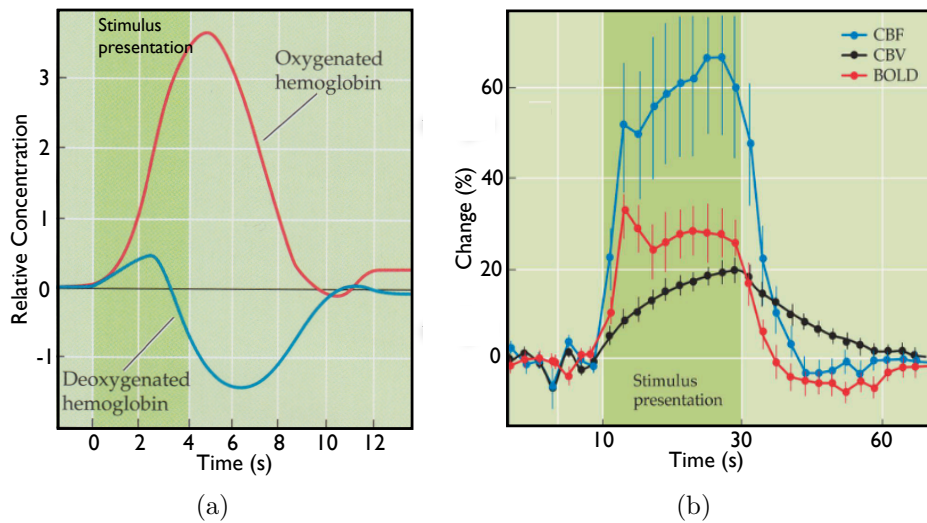


Figure 4.2: Hemodynamic response following neuronal activation (courtesy of [66]) (a) Changes in oxygenated and deoxygenated hemoglobin following neuronal stimulation. (b) Relative changes in cerebral blood flow and cerebral blood volume following neuronal activity.

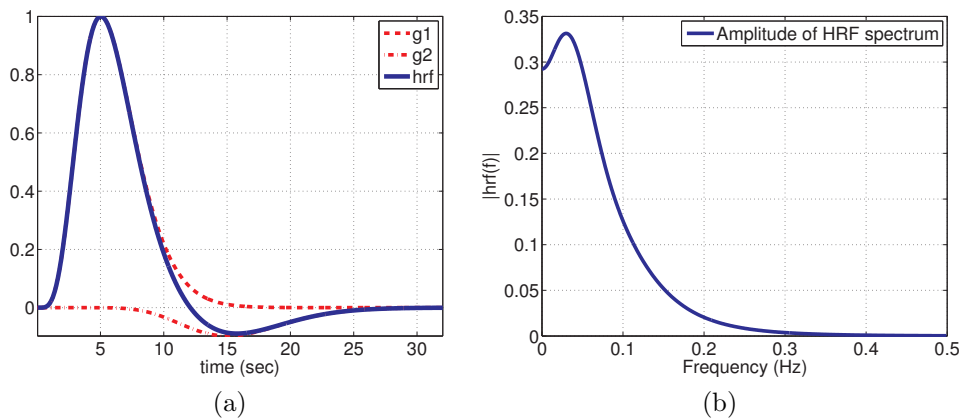


Figure 4.3: HRF and its spectrum: (a) two gamma representation of HRF where g_1 is a gamma function modelling the peak and g_2 is a gamma function modelling the undershoot (b) Amplitude of HRF spectrum

group studies including different tasks and brain regions [75, 76]. Therefore, the BOLD signal is represented through a linear convolution model between an activity signal and the hemodynamic response function (HRF), which is the supposed impulse response that characterizes the BOLD signal following a short period of brain activity.

There exist various approximation methods addressing the inter- and intra- subject variability, e.g, Fourier basis sets, finite impulse response and gamma functions [58, 59]. In the current work, we only consider simple approximations of the HRF with a difference of Gamma or Gaussian functions. Figure 4.3 shows the canonical HRF approximation using two gamma functions. Another advanced HRF model uses the linear approximation of the balloon model, which is the state-space representation of the BOLD response, and uses the first-order Volterra kernels [77]. With this model, the HRF is represented by a linear differential operator with its zeros and poles that demonstrates the underlying sparse structure of the fMRI signal model and provides

an operator that inverts the hemodynamic system [62].

The variability of the BOLD signal is not only due to the neural response. In particular, the measurement of the fMRI signal is corrupted by different types of artifacts including, but not limited to thermal noise due to the subject and the scanner, which tends to be spatially and temporally independent [78], physiological noise due to the subject's cardiac and respiratory movements [79], other subject specific effects due to the variation of BOLD hemodynamic responses across subjects and brain regions [80] and the gradual low frequency drifts and baseline variation in the voxel time series due to magnetic field inhomogeneities characterized by $1/f$ power spectrum [81, 82]. Typically, the noise in fMRI data is characterized by autoregressive models. Furthermore, artifacts due to head motion and low frequency drifts are carefully handled in the preprocessing stage of fMRI data analysis, then the residual errors are modeled with white noise assumption [59, 79].

4.2.3 FMRI data analysis and deconvolution frameworks

FMRI data is measured sequentially, typically while subjects engage in a task for a paradigm-based study or just lie in the scanner without any particular task for a resting-state study. The recorded data is then analyzed in order to understand how the particular task is processed by the brain. Selecting a suitable analysis method depends highly upon the aim of the study. Two classes of techniques are distinguished corresponding to the type of the experiments. On the one hand, confirmatory approaches put forward a hypothesis to be verified with the data from the experimental paradigm. Specifically, based on the research question, the experimenter first designs an experimental paradigm, and then exploits a subsequent statistical testing to affirm or reject the hypothesis. General linear model (GLM) is one of the most acknowledged methods in task-related fMRI analysis [83]. On the other hand, the purpose of the exploratory approaches, or data-driven methods, is to discover the underlying structures of the data that are not predicted a priori. Exploratory methods are essentially employed when the brain activity cannot be modeled with predefined responses, hence used extensively in the analysis of spontaneous brain activity. Independent component analysis (ICA) is one of the most commonly used data-driven method that aims at segregating the data into different compartments based on their statistical independence [84].

The GLM and the ICA are the common methods in modern fMRI data analysis. Alternatively, temporal analysis of the fMRI data is of practical interest to especially elaborate the unpredicted activations. Since GLM is only applicable when the task is explicit, and ICA does not incorporate any hemodynamic effect, new methodologies should be developed enabling the exploration of the hemodynamic brain activity without predefined responses.

FMRI deconvolution methods have been proposed to uncover underlying activity signals in BOLD response. Activelets framework is designed as an extension to traditional wavelets to decompose BOLD response that should ideally be represented by sparse activelet coefficients [85, 62]. Activelets are families of exponential spline wavelets that annihilate the null space of a general differential operator. More specifically, the activelets are constructed from the shifted replicates of the inverse of the hemodynamic system in a multiscale formalism. Paradigm-free mapping is another deconvolution method proposed for fMRI analysis [86, 61]. The method consists of two steps: temporal deconvolution using the canonical HRF model and consecutive statistical analysis of the time courses. Total activation (TA) [87, 63] is another alternative for the deconvolution of fMRI data that is based on spatiotemporal regularization where the temporal regularization is based on generalization of the total variation to the differential operator chosen as to invert the hemodynamic system and the spatial regularization uses a mixed-norm regularization to favor coherent activity-inducing signals in brain regions chosen from an anatomical brain atlas. Clearly, all the fMRI deconvolution methods have been proposed to uncover the underlying activity signal in BOLD at the fMRI timescale, and hence none of them examines the problem using a continuous-domain formulation.

4.3 Finite rate of innovation for fMRI data

We consider the BOLD response following a neural activation as a convolution of the activity signal $x(t)$ with an HRF model $f(t)$. In Figure 4.4, we observe an fMRI signal model for a single voxel's response over time. We specifically consider a set of innovation parameters $\{t_k, a_k\}_{k=0}^{K-1}$ that characterize the activity for that single voxel where $a_k \in \mathbb{R}$ are the amplitudes and $t_k \in \mathbb{R}$ are the instants. These signals are completely characterized by a finite number of parameters per unit time and hence, known as FRI signals. We will review the framework for FRI for a single voxel processing of the fMRI data.

4.3.1 FRI framework

We define the spontaneous activity signal $x(t)$ as a stream of K Diracs

$$x(t) = \sum_{k=0}^{K-1} a_k \delta(t - t_k), \quad (4.1)$$

where $\{t_k, a_k\}_{k=0}^{K-1}$ are the innovation parameters. The first step of the framework is the signal acquisition, which corresponds to the measurements of the BOLD response to an activity-inducing signal. The time course of a single voxel is then given by

$$\tilde{y}_n = \left\langle x(t), \varphi\left(\frac{t}{T} - n\right) \right\rangle + \epsilon_n, \quad (4.2)$$

where φ is a FRI sampling kernel that is related to the HRF such that $f(t) = \varphi(-t/T)$ where T is the sampling period; i.e., the scan repeat-time (TR) of the fMRI data and ϵ_n is the additive white noise.

The second step in the FRI framework (see Figure 4.4) is to compute the exponential reproducing coefficients $c_{m,n}$ that allow to map the fMRI samples to the so-called FRI samples. We first note that the HRF models do not satisfy the generalized Strang-Fix condition, but we have seen in Chapter 2 that for sufficiently fast decaying kernels, accurate reproduction of exponentials is possible. Hence, we now show how to obtain these coefficients using the knowledge of the HRF. We focus on the following approximation problem

$$\sum_{n \in \mathbb{Z}} c_{m,n} \varphi(t - n) \simeq e^{\alpha_m t}, \quad (4.3)$$

where $\alpha_m \in \mathbb{C}$ and $m = 0, \dots, P$. In Chapter 2, we have seen that the coefficients corresponding to the constant least-squares approximation are given by (2.23), namely $c_{m,n} = c_{m,0} e^{\alpha_m n}$ where $c_{m,0} = (\hat{\varphi}(\alpha_m))^{-1}$. In matrix representation, the mapping matrix \mathbf{C} is given as

$$\mathbf{C} = \underbrace{\begin{bmatrix} c_{0,0} & 0 & \cdots & 0 \\ 0 & c_{1,0} & \vdots & 0 \\ \vdots & \vdots & \ddots & \vdots \\ 0 & 0 & \cdots & c_{P,0} \end{bmatrix}}_{\mathbf{D}} \underbrace{\begin{bmatrix} 1 & e^{\alpha_0} & \cdots & e^{\alpha_0(N-1)} \\ 1 & e^{\alpha_1} & \cdots & e^{\alpha_1(N-1)} \\ \vdots & \vdots & \ddots & \vdots \\ 1 & e^{\alpha_P} & \cdots & e^{\alpha_P(N-1)} \end{bmatrix}}_{\mathbf{V}}, \quad (4.4)$$

where \mathbf{D} is a diagonal matrix, and \mathbf{V} is a Vandermonde matrix. Hence, for the FRI-mapping matrix \mathbf{C} to be better conditioned, we want the ratio the absolute values of the diagonal elements of \mathbf{D} to be chosen close to each other so that $\frac{\max\{|c_{m,0}|\}}{\min\{|c_{m,0}|\}} \simeq 1$ and the elements in \mathbf{V} to lie on the unit circle [88]. While choosing α_m to be purely imaginary makes the Vandermonde matrix \mathbf{V} better conditioned, the coefficients are now related to the Fourier transform of the sampling

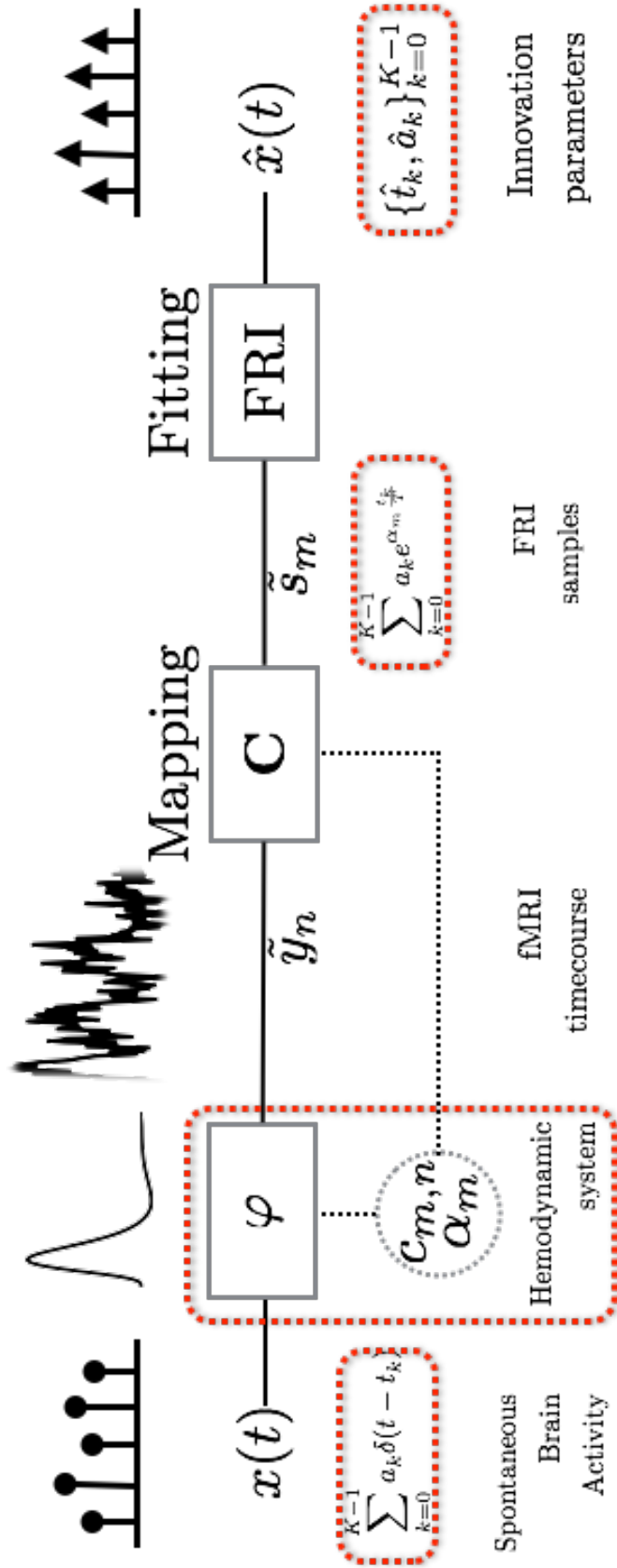


Figure 4.4: FRI framework for fMRI: The original continuous-time activity signal $x(t)$ is filtered with an arbitrary sampling kernel before being uniformly sampled with a sampling period T where the samples are given by $y_n = \langle x(t), \varphi(t/T - n) \rangle$. Then, using the information about the sampling kernel one designs a weighting matrix **C** so that the samples are mapped to FRI-space, i.e., to retrieve exponential moments of the signal. Finally, the reconstruction of the parameters is achieved using the FRI with model-fitting approach

kernel, $c_{m,0} = \hat{\varphi}(j\omega_m)^{-1}$. Since the HRF signal is a low-pass blurring kernel, the condition on the diagonal entries of \mathbf{D} is satisfied when the set of exponentials are chosen where the spectrum attenuation is not very strong. This fact leads to a trade-off in the choice of ω_m and we choose to use the frequency range only up to the full width at half maximum (FWHM) of the spectrum of the HRF. We define the exponentials as

$$\alpha_m = j\omega_m = j\frac{\pi}{L}(2m - P) \quad m = 0, \dots, P, \quad (4.5)$$

and then optimize the values P and L , accordingly. Here, the ratio of $\frac{2\pi}{L}$ defines the spacing of the chosen frequencies in the spectrum. Moreover, we would like to emphasize that by choosing P odd, we can remove the zero frequency component in the set of reproduced exponentials which can be used to remove gradual low frequency drifts in the fMRI data inherently.

Given a set of frequencies α_m and the corresponding coefficients $c_{m,n}$, the fMRI samples y_n are then mapped to the FRI-space by linearly combining the samples with the coefficients $c_{m,n}$. Hence, the FRI samples are given by,

$$\tilde{s}_m = \sum_n c_{m,n} \tilde{y}_n, \quad (4.6)$$

which we know from Chapter 2 to be equivalent to

$$\tilde{s}_m = \sum_{k=0}^{K-1} \tilde{a}_k u_k^m + \tilde{e}_m, \quad (4.7)$$

where $\tilde{a}_k = a_k e^{\alpha_0 \frac{t_k}{T}}$, $u_k = e^{\alpha \frac{t_k}{T}}$ and \tilde{e}_m is the filtered noise that remains white by construction of the matrix \mathbf{C} .

In standard FRI framework, the annihilating filter (AF) method proceeds by defining the Prony's filter h with z-transform

$$H(z) = \sum_{m=0}^K h_m z^{-m} = h_0 \prod_{k=0}^{K-1} (1 - u_k z^{-1}), \quad (4.8)$$

where the roots correspond to the values u_k . Then, it follows that h_m annihilates the sequence s_m as:

$$(h * s)_m = \sum_{i=0}^K h_i s_{m-i} = 0. \quad (4.9)$$

which can be written in matrix/vector representation as

$$\mathbf{S}(\mathbf{s})\mathbf{h} = \mathbf{0}, \quad (4.10)$$

where $\mathbf{S}(\mathbf{s})$ is a rank deficient Toeplitz matrix and \mathbf{h} admits a solution in the nullspace of $\mathbf{S}(\mathbf{s})$ if $\text{rank}(\mathbf{S}(\mathbf{s})) = K$. Hence, the standard FRI looks for a solution that minimizes $\|\tilde{\mathbf{S}}\mathbf{h}\|$ under the constraint that $\|\mathbf{h}\|^2 = 1$.

4.3.2 FRI with model-fitting

We propose to use the FRI reconstruction method with a model fitting approach using the (randomized) linear constraint (MF-3) of Chapter 3. The idea is to minimize the error between the measured FRI samples \tilde{s}_m and the recovered FRI samples s_m subject to the annihilation system in (4.10) as a constrained optimization problem. Hence, we reformulate the estimation problem as

$$\min_{s, h} \|\tilde{\mathbf{s}} - \mathbf{s}\|^2 \quad \text{subject to } \mathbf{S}(\mathbf{s})\mathbf{h} = \mathbf{0} \text{ and } (\mathbf{h}^{(0)})^H \mathbf{h} = 1, \quad (4.11)$$

where $\mathbf{S}(\mathbf{s})$ is the same Toeplitz matrix in (4.10) with $[\mathbf{S}]_{mi} = s_{m-i}$, \mathbf{h} is the vector of the coefficients of the filter defined in (4.8) and $\mathbf{h}^{(0)}$ is random initialization of \mathbf{h} . We note that, using the commutativity of the convolution, the annihilation equation (4.9) can be rewritten as

$$\mathbf{R}(\mathbf{h})\mathbf{s} = \mathbf{0}, \quad (4.12)$$

where $\mathbf{R}(\mathbf{h})$ is the Toeplitz matrix with $[\mathbf{R}(\mathbf{h})]_{mj} = h_{m-j}$. We first replace the original problem (4.11) with the following unconstrained minimization problem

$$\min_{\mathbf{s}, \mathbf{h}} \underbrace{\|\tilde{\mathbf{s}} - \mathbf{s}\|^2 + 2\{\mathbf{u}^H \mathbf{S}(\mathbf{s})\mathbf{h}\} + \lambda((\mathbf{h}^{(0)})^H \mathbf{h} - 1)}_{\mathcal{L}\{\mathbf{s}, \mathbf{h}\}}, \quad (4.13)$$

to be minimized with respect to \mathbf{s} and \mathbf{h} where \mathbf{u} is a vector Lagrange multiplier for the constraints $\mathbf{S}(\mathbf{s})\mathbf{h} = \mathbf{0}$ and λ is a scalar Lagrange multiplier for the constraint $((\mathbf{h}^{(0)})^H \mathbf{h} - 1)$. Following the development of Chapter 3, we obtain an equivalent problem. Therefore, rather than minimizing (4.13) with respect to \mathbf{s} and \mathbf{h} , we minimize the following problem with respect to \mathbf{h} only

$$\min_{\mathbf{h}} \mathbf{h}^H \mathbf{S}(\tilde{\mathbf{s}})^H \mathbf{D}_{\mathbf{h}}^{-1} \mathbf{S}(\tilde{\mathbf{s}}) \mathbf{h} \text{ subject to } (\mathbf{h}^{(0)})^H \mathbf{h} = 1, \quad (4.14)$$

where $\mathbf{D}_{\mathbf{h}} = \mathbf{R}(\mathbf{h})\mathbf{R}(\mathbf{h})^H$. Similarly, we propose to use IQML algorithm assuming the term $\mathbf{D}_{\mathbf{h}}$ remains constant at each iteration.

By solving (4.14), we first obtain the filter coefficients h_m to retrieve u_k by finding the roots of the filter in (4.8). We then obtain the locations t_k using the solution u_k , since $u_k = e^{\alpha \frac{t_k}{T}}$. Finally, given the locations t_k , we determine the amplitudes a_k by solving K consecutive equations of (4.7).

4.3.3 HRF model approximation

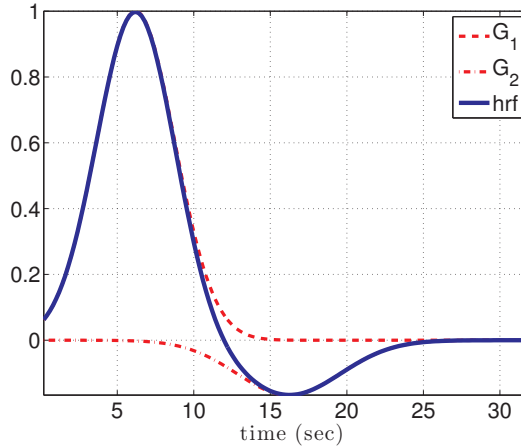


Figure 4.5: Difference of Gaussian representation of HRF where G_1 models the peak and G_2 models the undershoot

In principle, any HRF model approximation can be used in this framework as long as the approximation allows us to compute the exponential reproduction coefficients efficiently, which is related to the Fourier transform of the kernel. We propose to use an HRF model described by a difference of two Gaussians, since the Gaussian functions are good candidates for this approach

as the analytic expression of their Fourier transform is known. We choose to use an HRF model described by:

$$f(t) = \sum_{i=1}^2 a_i G_i(t, \mu_i, \sigma_i^2), \quad (4.15)$$

where $G_i(t, \mu_i, \sigma_i^2)$ is a Gaussian function with mean μ_i and variance σ_i^2 and the parameters are estimated using the canonical HRF model. Finally, the specific model parameters are chosen as $a = [1, -\frac{1}{6}]^T$, $\mu = [6, 16]^T$ and $\sigma = [\frac{6}{2\sqrt{2}\log 2}, \frac{8}{2\sqrt{2}\log 2}]^T$ for the initial peak, and the undershoot, respectively.

4.4 Results

4.4.1 Simulation results

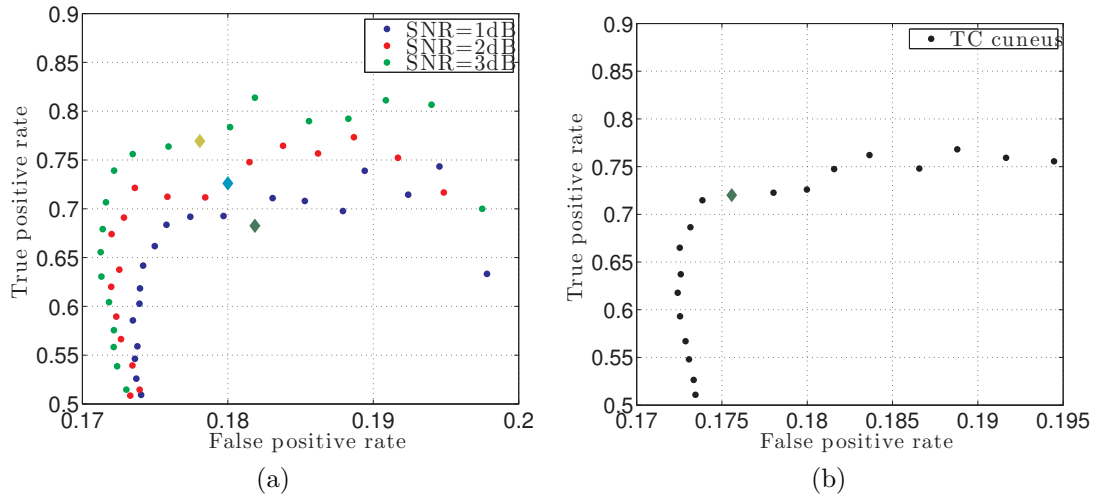


Figure 4.6: Receiver operating characteristic (ROC) curve for (a) simulated data (b) experimental data taken as the time course of the cuneus region for subject-1. Each point represents the average true and false positive rates with model order changing from $K = 1$ to $K = 20$ in counterclockwise directions, and the diamond indicates the ground-truth model order.

We simulate a number of voxels that are assumed to have same weighing activation. However, the instants of the activity may differ up to $\pm 1\text{TR}$ with respect to different voxels. We design the spontaneous activity pattern with unit amplitudes and different onset times given by $t_k = [20, 34, 54, 92, 130, 142, 170, 188]^T$ secs for 150 voxels with $\text{TR}=2$ sec and we focus on the retrieval of the timing of the activities. In Fig. 4.6, we show the receiver operating characteristic (ROC) curves for the proposed FRI fitting algorithm for different SNR levels. Each point represents the average true and false positive rates with the model order changing from $K = 1$ to $K = 20$ in counterclockwise directions. Clearly, we observe high sensitivity and specificity behavior around the true model order $K = 8$.

4.4.2 Experimental results

Data preprocessing

We further tested our method with experimental data acquired from three subjects during a sparse event-related paradigm where resting-state periods were disrupted by 10 visual stimuli of 8Hz flickering checkerboard of duration 1s with onsets $t_k = [17, 32, 51, 90, 127, 139, 168, 185, 212, 247]^T$ s [63]. The fMRI data comprised N= 190 (subjects-1) and N=160 (subject-2 and subject-3) $T2^*$ -weighted gradient echo-planar volumes (TR/TE/flip Angle: 2 s/30 ms/85, voxel size: $3.25 \times 25 \times 3.5$ mm³, matrix= 64×64). A T1-weighted MPRAGE anatomical image was also acquired during the MR session (192 slices, TR/TE/flip Angle: 1.9 s/2.32 ms/9, voxel size: $0.45 \times 0.45 \times 0.9$ mm³, matrix= 512×512).

Anatomical and functional data were preprocessed using SPM8 [59], and a combination of in-house MATLAB scripts. The first ten functional volumes were discarded to allow for T1 equilibration effects. The remaining functional volumes were spatially realigned to the mean image, and then followed by spatial smoothing with a Gaussian filter (FWHM=5 mm). The anatomical data of each subject were coregistered to the functional images and segmented into white matter, gray matter and cerebrospinal fluid (new segmentation algorithm of SPM8, an extension of the unified segmentation algorithm [89]). Nuisance variables (motion parameters, average cerebrospinal fluid and white matter signal) were regressed out from fMRI time courses using a GLM. The T1 volume was then parcellated into 90 cortical regions using the automated anatomical labeling (AAL) atlas (90 regions without the cerebellum) and the IBASPM toolbox [90]. This structural atlas was then resampled to the functional space resolution and overlapped with the fMRI volumes to select voxels of specific brain anatomical regions. We also computed the average time courses of each region and pairwise correlations between all pairs of regions forming a 90×90 connectivity matrix for every subject.

FRI recovery results

In the first part, we considered the voxels from the cuneus region in the visual cortex, which supposedly activates completely during the visual stimuli. After the preprocessing steps, we have in total 363 voxels for subject-1, 230 voxels for subject-2 and 327 voxels for subject-3. Moreover, by removing the first ten functional volumes, we omit the initial flickering that occurs at 17 sec. The flexibility to choose different model order K thanks to the model fitting approach allows to analyze the fMRI data with respect to desired specificity and sensitivity range, which is also shown in Fig. 4.6 (b). Here, we observe high sensitivity and specificity behavior around the true model order $K = 9$. In Figures 4.7, 4.8 and 4.9, we illustrate the change in the voxel data and spatial covariance before and after applying the FRI recovery for subject-1, subject-2 and subject-3, respectively. We choose the model order K based on the model order selection framework of Section 3.2.3. After applying the FRI recovery for the specified model order, we recover the fMRI time course based on the estimated innovation parameters. We then perform a k-means clustering using cosine distance measure to arrange the voxels in two groups based on the spatial covariance of the voxels. Clearly, in all three subjects, model-fitting framework improves the segregation of the voxels in terms of the assigned silhouette values of the clusters before and after the FRI recovery (see Figures 4.7 to 4.9).

Interestingly, we observe that the cuneus region of subject-1 (Figure 4.7) responds to all the stimuli and with $K = 10$ we can successfully detect all activations in the FRI framework. Instead, the subject-2 (figure 4.8) and the subject-3 (figure 4.7) are less responsive to some of the stimuli. In this case the FRI framework recovers the activity signal with a reduced number of activity, i.e., $K = 5$ for subject-2 and $K = 6$ for subject-3. A potential reason is that the visual stimuli are unanticipated by the subject undergoing the experiment, hence it is likely that some stimuli were only briefly attended or even missed by the subjects. Further we noticed that not all the voxels of the cuneus follow the paradigm, and this could be due to the fact that the cuneus

region is defined by an atlas that has certain limitations such that morphing it to individual's brain cause inevitable distortions.

In the second part, we repeat the same analysis to uncover interactions of different regions using the data acquired from subject-1. For this, we compare the activities in the cuneus with one region showing positive correlation with the cuneus in the connectivity matrix (superior occipital cortex), one showing negative correlation (postcentral gyrus) and one showing no correlation (precentral gyrus). These specific regions are shown in Figure 4.10 (a) and (b) in terms of the connectivity matrix and T1-registered functional atlas, respectively. To note, the functional connectivity matrix is based on regionally averaged time series, therefore the correlation are computed supposing the voxels in the same region behave similarly. In Figures 4.11 and 4.12, we illustrate the change in the fMRI data before and after applying the FRI recovery with the specified activity rate K based on the model order selection framework of Section 3.2.3 and a consecutive performing of k-means clustering to arrange the voxels in two groups using the spatial covariance of the voxels. Even for these regions, we observed the FRI framework is able to detect visual and non-visual related activities. For the regions that we expect to be correlated with the cuneus (superior occipital cortex and postcentral gyrus), we observe only a subset of voxels showing an activity pattern related to the paradigm. This can again be explained with the suboptimal approximation given by the atlas in parcellating functional regions. Further, the FRI framework detects activation events unrelated to the stimulation pattern for the precentral gyrus, expected to be uncorrelated with the cuneus, preliminarily showing the capability of detecting spontaneous activity.

4.5 Summary

We have proposed a new framework for the analysis of fMRI data using the novel FRI fitting framework. Modeling the spontaneous activity signal as an FRI signal (i.e., a stream of Diracs), we considered the fMRI time course as a filtered version of the activity signal with an HRF model that was approximated by two Gaussian functions. Using an appropriate FRI space mapping kernel, we obtained an equivalent FRI space estimation problem that we solved using a fitting approach that allows stable recovery of the innovation parameters for different innovation rate. Hence, we achieved a stable FRI reconstruction method for the detection of spontaneous activity in fMRI data up to the desired level of specificity and sensitivity.

We demonstrated the feasibility of our approach for fMRI analysis by retrieving the activity signal from simulated and experimental fMRI data. Both results show the potential of this novel method, however larger datasets should be analyzed to confirm the consistency and eventually draw conclusions that might be useful from a neuroscientific point-of-view.

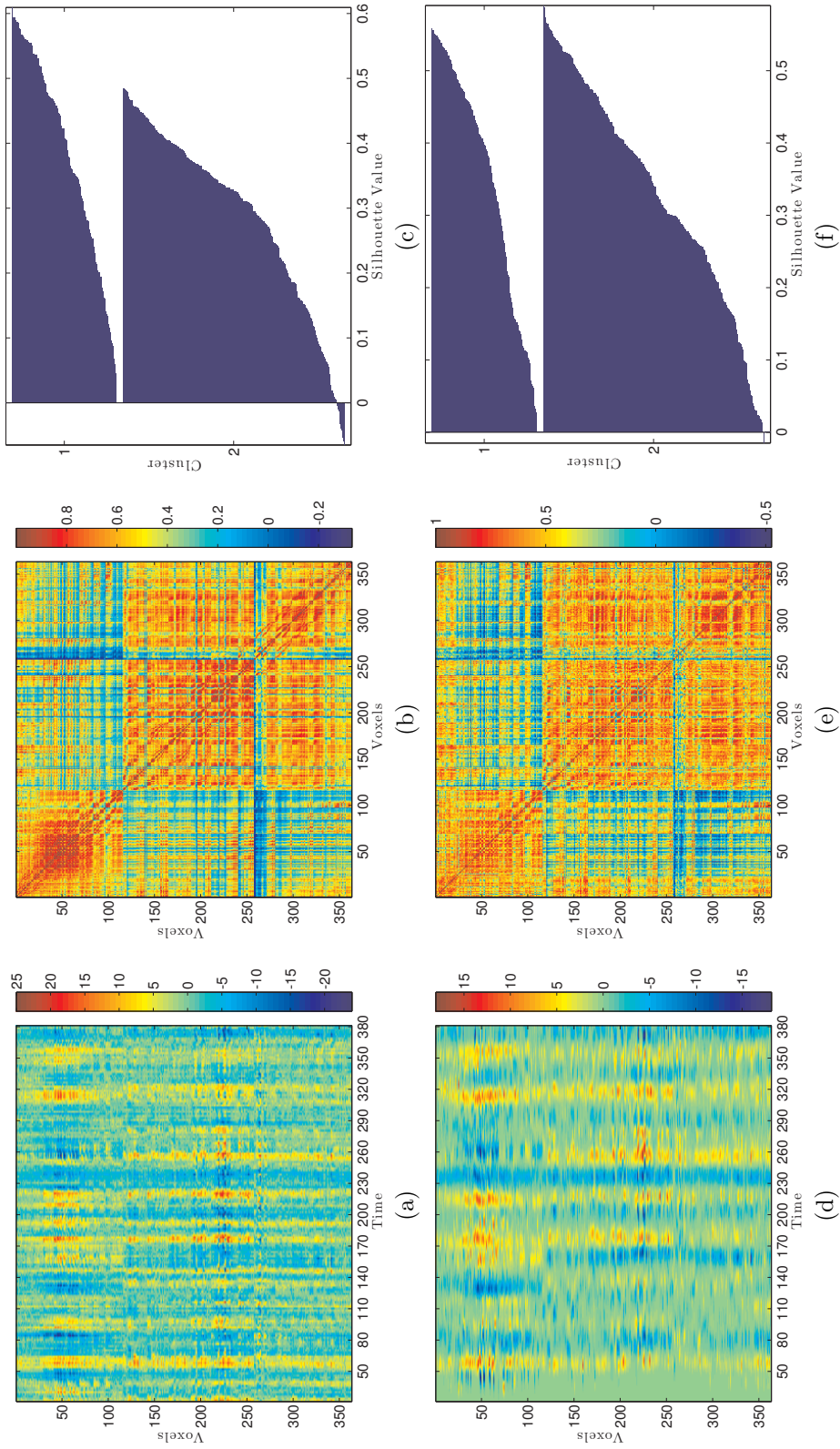


Figure 4.7: Visualization of the change in fMRI data before and after FRI recovery for the cuneus region of subject-1. (a),(d) original and the recovered time courses for $K = 10$, respectively. (b), (e) covariance matrix before and after FRI recovery. (c), (f) silhouette plot for k-means clustering. For visualization purposes the voxels are arranged in 2 groups according to k-means clustering using cosine distance measure.

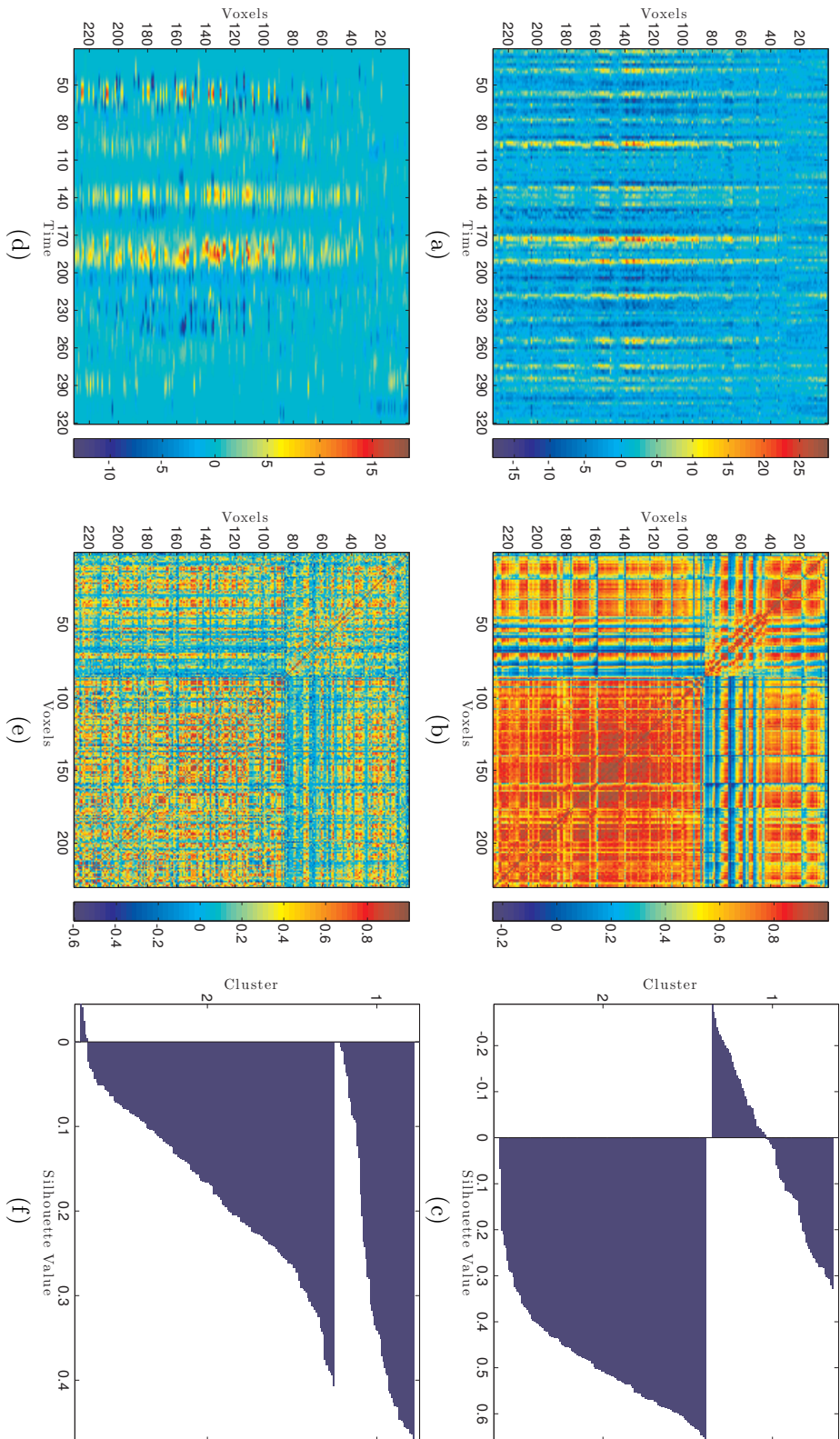


Figure 4.8: Visualization of the change in fMRI data before and after FRI recovery for the cuneus region of subject-2. (a),(d) original and the recovered time courses $K = 5$, respectively. (b), (e) covariance matrix before and after FRI recovery. (c), (f) silhouette plot for k-means clustering. For visualization purposes the voxels are arranged in 2 groups according to k-means clustering using cosine distance measure.

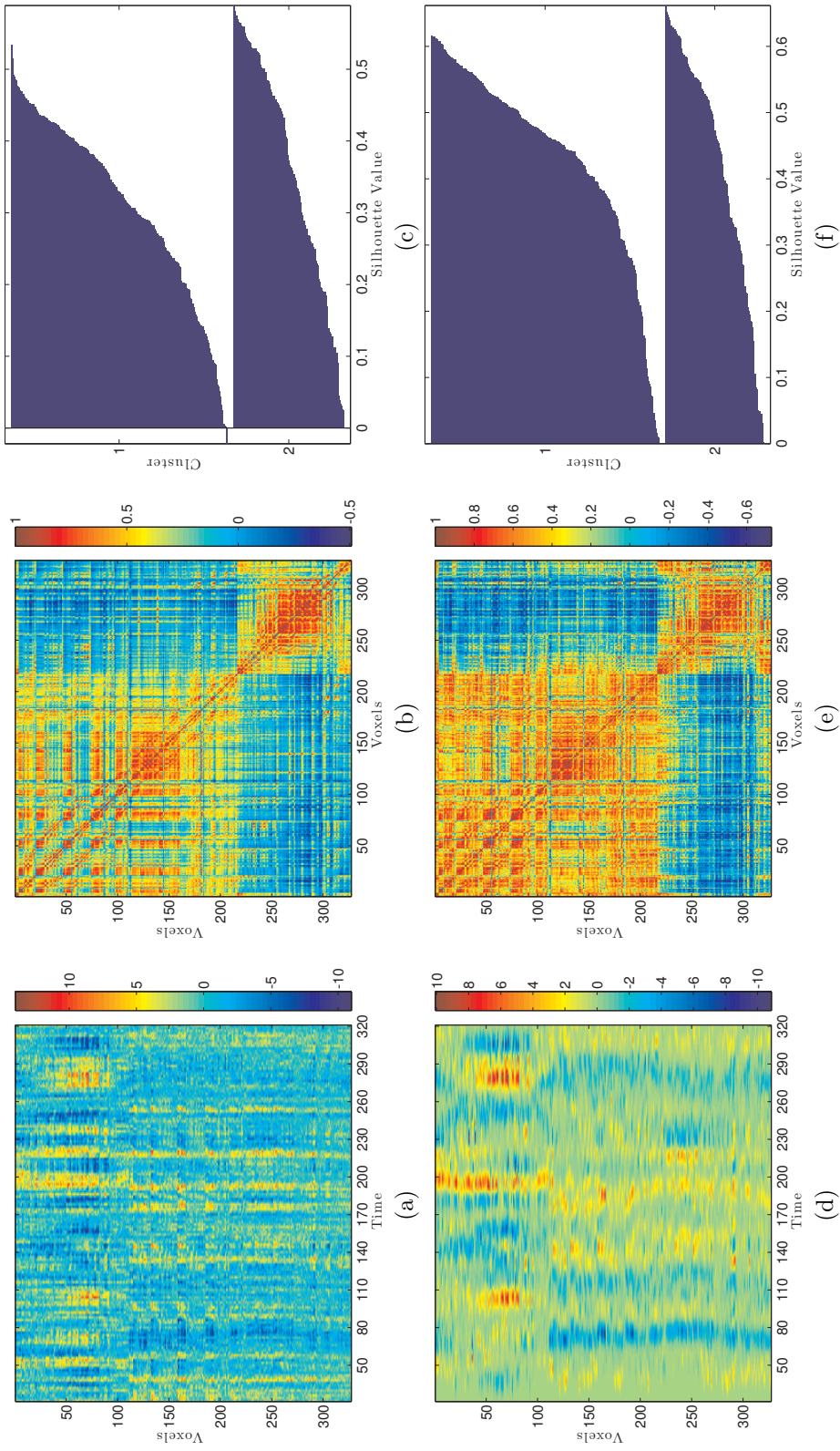


Figure 4.9: Visualization of the change in fMRI data before and after FRI recovery for the cuneus region of subject-3. (a),(d) original and the recovered time courses $K = 6$, respectively. (b), (e) covariance matrix before and after FRI recovery. (c), (f) silhouette plot for k-means clustering. For visualization purposes the voxels are arranged in 2 groups according to k-means clustering using cosine distance measure.

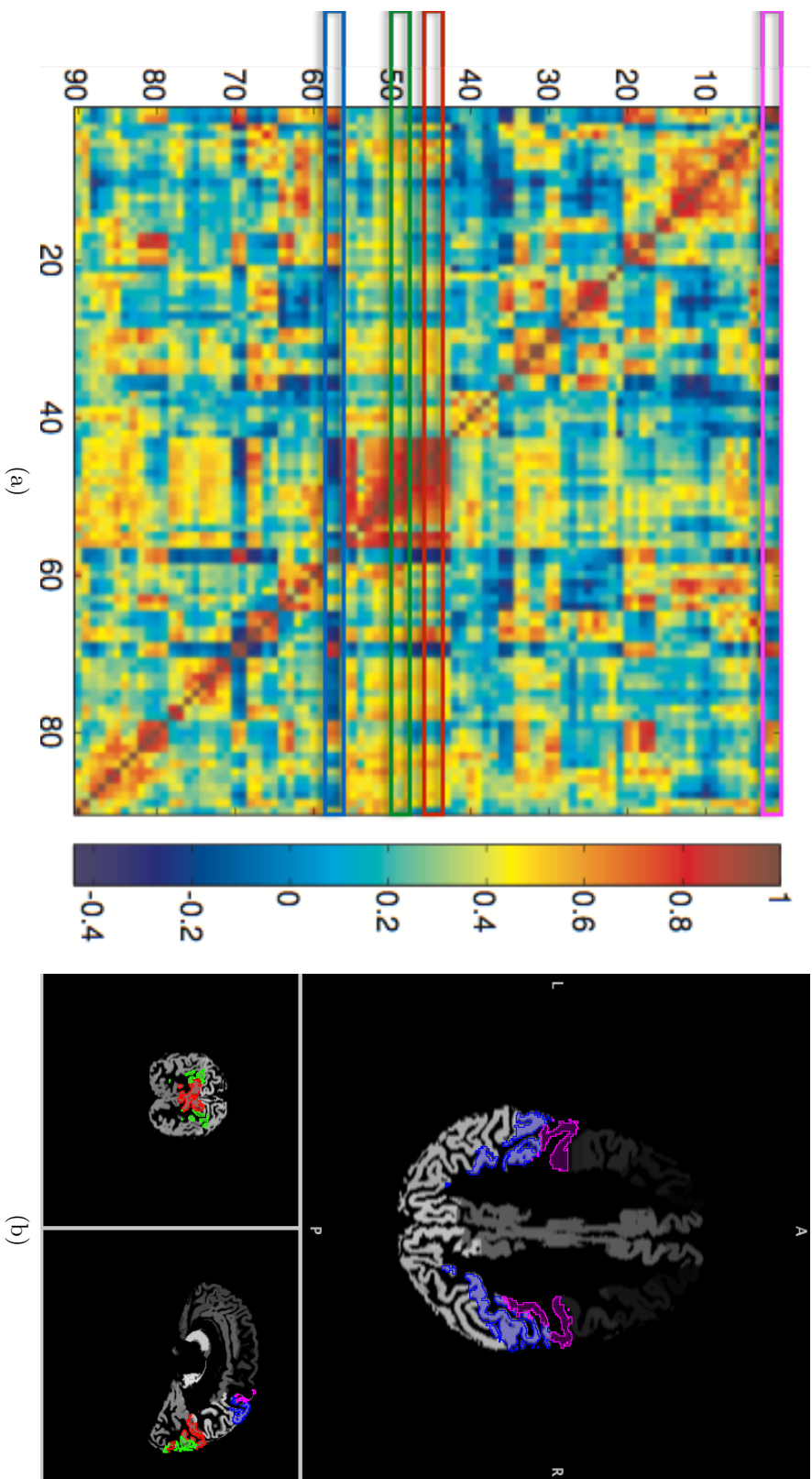


Figure 4.10: Visualization of the interactions between different regions of subject-1. (a) Functional connectivity matrix between 90 regions, (b) T1 registered functional atlas. The colors with frames in (a) and with contours in (b) represent different regions in the brain, specifically the red colors show the cuneus, the green shows superior occipital cortex, the blue color shows the postcentral gyrus, the pink color shows the precentral gyrus.

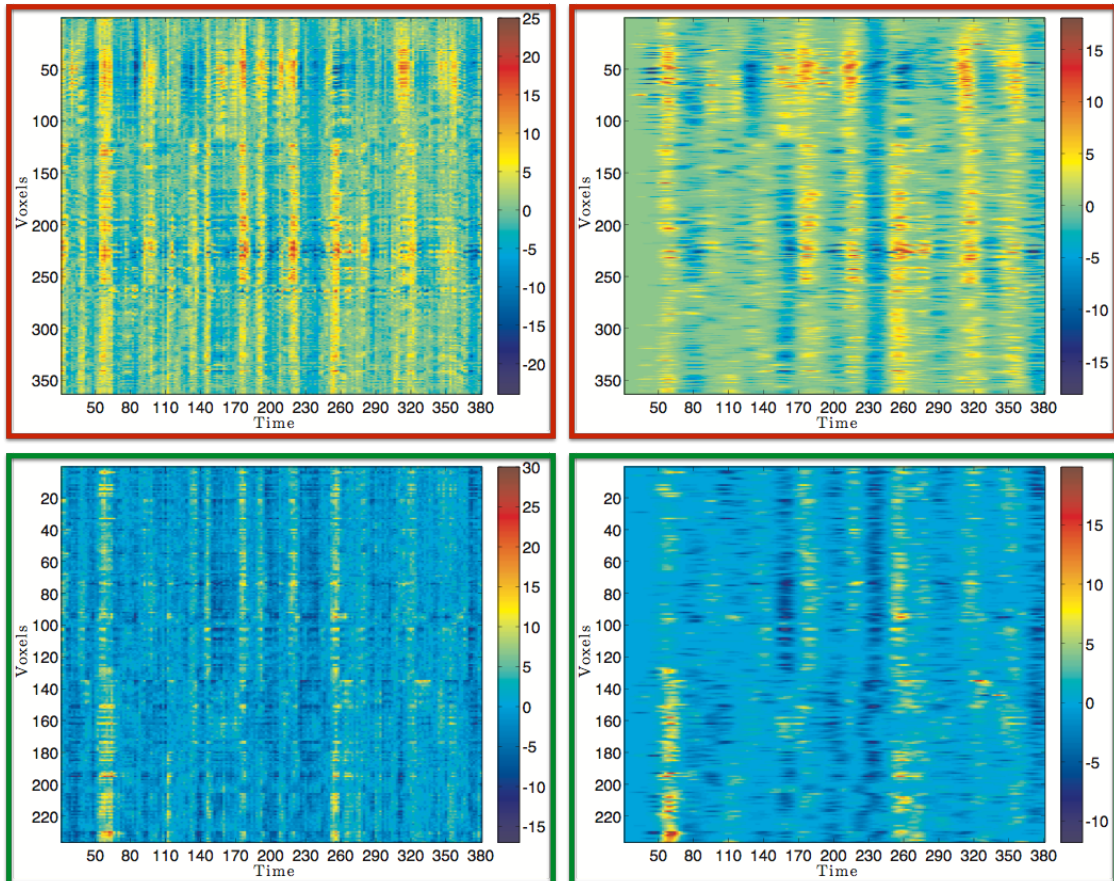


Figure 4.11: Visualization of the change in fMRI data before (left) and after (right) FRI recovery for the cuneus of subject-1 in red frames for FRI recovery with $K = 10$ and for the superior occipital cortex of subject-1 in green frames for FRI recovery with $K = 6$.

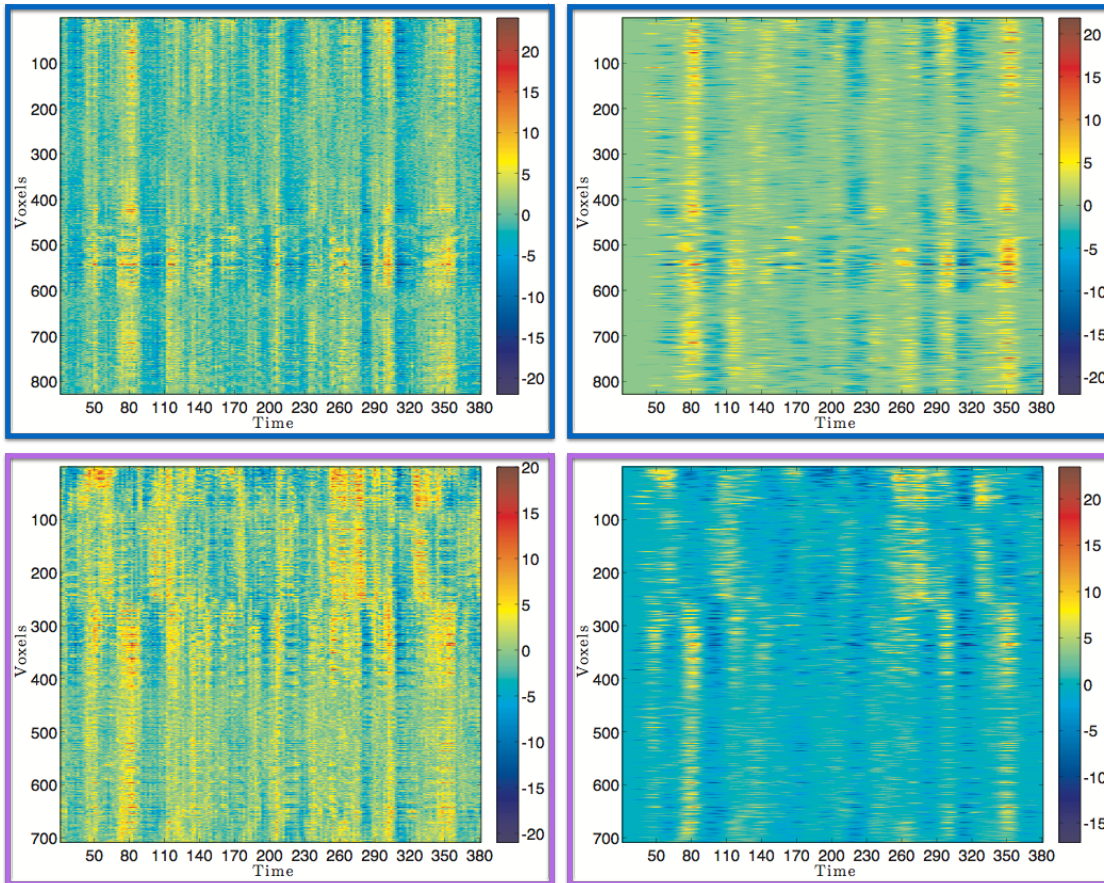


Figure 4.12: Visualization of the change in fMRI data before (left) and after (right) FRI recovery for the postcentral gyrus of subject-1 in blue frames for FRI recovery with $K = 10$ and for the precentral gyrus of subject-1 in pink frames for FRI recovery with $K = 6$.

Chapter 5

FRI for the Inverse Source Problem of Radiating Fields

This chapter is based on the publication: Z. Doğan, T. Blu and D. Van De Ville, ‘*Finite-rate-of-innovation for the inverse source problem of radiating fields*’, *Sampling Theory in Signal and Image Processing*, vol. 13 : (3), 2014, pp. 271-294.

5.1 Introduction

The inverse source problem (ISP) is of interest and importance across many branches of physics, mathematics, engineering and medical imaging. Among these, reconstruction of source distributions from boundary measurements of radiating fields has attracted great attention of many researchers. In particular, the Helmholtz equation that is the fundamental model for radiation and wave propagation has been studied extensively for various electromagnetic and scalar fields [91, 92]. In general, the underlying physical system assumes a well-posed forward model, but, they usually suffer from having an ill-posed inverse problem in terms of uniqueness, stability, and existence of a solution. Typically, one needs additional assumptions about the source distribution to force uniqueness of the solution by either imposing smoothness properties of the distribution or by assuming a parametric source model. The standard solutions of the ISP rely on iteratively fitting of a source model using the forward model. In this case, the sparsity assumption of the source signal plays a key role to regularize the solution [93]. Recently, compressive sensing approaches have been employed [94] for the detection of sparse objects from the field measurements in radar imaging.

There exist several approaches for the ISP that assume parametric source models. In particular, the mathematical uniqueness and local stability of the parametric source distributions have been proven [95]. Moreover, there are several other parameter estimation frameworks in which the computational burden of forward model fitting can be dealt with efficient algorithms [96]. For example, the method known as “reciprocity gap” concept [97] which is essentially an application of Green’s theorem has been recently applied to ISP from boundary measurements of a Poisson’s field [95]. The method is based on transforming a scalar product between the source distribution and a test function into a boundary integral of the measurements and related test function [95].

Several sampling and reconstruction methods have been proposed for specific classes of signals [4], as we have seen in Chapter 2. The common feature of these signals is that they have a parametric representation with finite number of parameters and are, therefore, called the signals with finite-rate-of-innovation (FRI) [4, 5, 24]. Recently, the theory of FRI has been applied to the problem of detecting parametric point sources from boundary measurements of a field generated by the Poisson’s equation [21]. The method proposes analytic sensing functions to map back

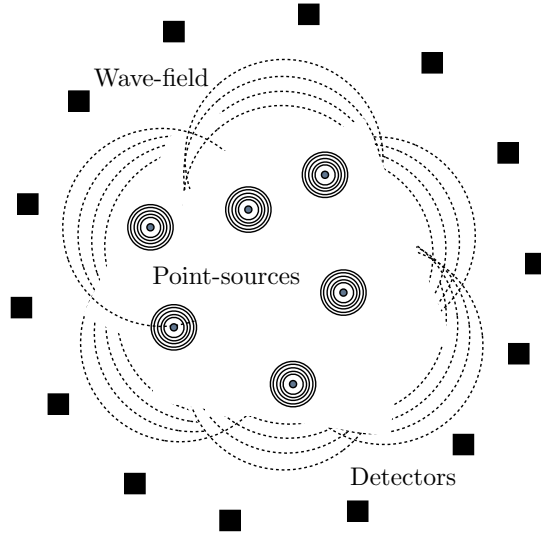


Figure 5.1: Schematic overview of the measurement model and the simplified view of the radiating wavefronts.

the boundary measurements to the underlying point distribution and shows that it is possible to develop non-iterative reconstruction algorithms to retrieve the innovation parameters. The results have been also extended to a multi-layer head model with potential application to detect the epileptic foci from electroencephalography (EEG) data [22].

In this chapter, we focus on the ISP from boundary measurements of radiating fields governed by the Helmholtz equation. A typical measurement setup is shown in Figure 5.1. We exploit an explicit sparsity prior on the source model being a 3-D stream of Diracs such that the only innovation parameters are the locations and weights. Then, we develop a new framework that allows us to identify parametric source models from boundary measurements of a radiating field. For that, we extend the FRI framework developed for the Poisson's equation [21, 22] to general sensing functions derived for radiating fields based on holomorphic functions in the complex plane. Our contributions are twofold: First, we apply the reciprocity gap concept to the sensing functions that are solutions to the homogeneous Helmholtz equation and show that these functions can be used to extract 2-D projections of the locations of the source distribution. Second, we propose families of sensing functions that are holomorphic functions and generate complex polynomials of N-th degree. We show that these sensing functions have a spatial localization that can be controlled so that they dominantly sense the influence of nearby pointwise sources.

This approach brings together several attractive features: (1) the 2-D projections of the locations onto several planes are decoupled; (2) several 2-D projections are combined to retrieve the 3-D locations with a tomographic approach; (3) the solution to the forward model is not necessary; (4) the method is locally adaptive thanks to the generalization of the holomorphic functions to reproduce N-th order polynomials.

5.1.1 Forward problem

The forward problem describes the radiation of waves from a real-valued spatio-temporal source distribution $q(\mathbf{r}, t)$ embedded in an infinite, homogeneous medium. The real-valued radiating wave field satisfies the inhomogeneous scalar wave equation

$$\left[\nabla^2 - \frac{1}{c^2} \frac{\partial^2}{\partial t^2} \right] u(\mathbf{r}, t) = q(\mathbf{r}, t), \quad (5.1)$$

everywhere in space and time, where c is the speed of wave propagation in the medium. The source term $q(\mathbf{r}, t)$ is assumed to be compactly supported in the space-time region $S_0 | \mathbf{r} \in \Omega, t \in [0, T_0]$, where Ω is the spatial volume and $[0, T_0]$ is the interval of time over which the source is present. The solution to (5.1) is not unique. In particular, adding any solution of the homogeneous wave equation to $u(\mathbf{r}, t)$ will be again a solution to (5.1). Therefore, it is necessary to specify initial conditions under the form of Cauchy conditions.

Primarily, the harmonic solution of the wave equation is of particular interest in various applications because the wave equation applies only to non-dispersive and non-attenuating medium, whereas the counterpart Helmholtz equation describes the radiation of waves in a general dispersive medium

$$[\nabla^2 + k^2] U(\mathbf{r}, \omega) = Q(\mathbf{r}, \omega), \quad (5.2)$$

where $k(\mathbf{r}) = \omega/c(\mathbf{r})$ is the wavenumber and $c(\mathbf{r})$ is speed of wave propagation in an inhomogenous medium. Hence, the Helmholtz equation is considered to be the fundamental governing equation of radiation and wave propagation. As it was the case for (5.1), (5.2) does not possess a unique solution and, in particular, one needs to determine the boundary conditions that are dictated by the physics of the problem on the measurement. Then, if the source term, $Q(\mathbf{r}, \omega)$ is known, the solution to (5.1) can be written as

$$U(\mathbf{r}, \omega) = \int_{\Omega} d^3r' G_+(\mathbf{r} - \mathbf{r}', \omega) Q(\mathbf{r}', \omega), \quad (5.3)$$

where $G_+(\mathbf{r})$ is the retarded Green's function of the Helmholtz equation defined as the solution to the partial differential equation

$$[\nabla^2 + k^2] G_+(\mathbf{r} - \mathbf{r}', \omega) = \delta(\mathbf{r} - \mathbf{r}'). \quad (5.4)$$

In the case of the radiating fields in free-space, the physically appropriate boundary condition is that the Green's function satisfies the Sommerfeld radiation condition that is equivalent to the requirement of causality in time domain [92]. Hence, the resulting Green's function is known as the retarded Green's function

$$G_+(\mathbf{r} - \mathbf{r}', \omega) = -\frac{1}{4\pi} \frac{e^{ik\|\mathbf{r}-\mathbf{r}'\|}}{\|\mathbf{r} - \mathbf{r}'\|} \quad (5.5)$$

representing an outgoing-wave.

5.1.2 Inverse source problem

The inverse source problem (ISP) is about finding the source term $Q(\mathbf{r}, \omega)$ from the knowledge of the radiating field $U(\mathbf{r}, \omega)$. The solution to the ISP becomes trivial, when the field $U(\mathbf{r}, \omega)$ is known over S_0 . Indeed, one can simply apply the D'Alembertian operator $\mathcal{W} = \nabla^2 + k^2$ to the field to recover the source term according to the Helmholtz equation. However, in practical situations, the field can only be measured in a restricted region that lies outside the source's space-time support S_0 . In particular, the field $U(\mathbf{r}, \omega)$ and its normal derivative $\partial U(\mathbf{r}, \omega)/\partial n'$ are supposed available on a closed surface $\partial\Omega$.

The standard solution of the source term by the boundary data is given by the Porter-Bojarski (PB) integral equation,

$$Q(\mathbf{r}, \omega) = - \int_{\partial\Omega} dS' \left[U(\mathbf{r}, \omega) \frac{\partial G_-(\mathbf{r} - \mathbf{r}', \omega)}{\partial n'} - G_-(\mathbf{r} - \mathbf{r}', \omega) \frac{\partial U(\mathbf{r}, \omega)}{\partial n'} \right], \mathbf{r} \in \Omega \quad (5.6)$$

where $G_- = G_+^*$ is known as the retarded Green's function representing an incoming-wave, hence (5.6) is referred as the back-propagated-field solution [92].

The classical treatment of the problem based on (5.6) has several limitations that include the limitation to non-dispersive media and the requirement of having full data set over a closed

surface surrounding the source. As an alternative, the problem can be cast in a Hilbert space formulation

$$TQ = f, \quad (5.7)$$

where $T : \mathcal{H}_Q \rightarrow \mathcal{H}_f$ is a linear mapping from a Hilbert space of source functions \mathcal{H}_Q to Hilbert space of measurements \mathcal{H}_f , f is the data term and Q is the source term. With this formulation, the ISP will also apply to the cases of incomplete data as well as to dispersive medium. However, as the two Hilbert spaces \mathcal{H}_Q and \mathcal{H}_f are generally different and the linear operator T is not generally Hermitian, inverting such mappings for the source in terms of data generally requires finite element methods that are computationally heavy [92].

5.2 Finite rate of innovation for the Helmholtz equation from boundary measurements

5.2.1 Innovation signal for radiating field

We consider a 4-D signal model with M point sources inside a region $\Omega \subset \mathbb{R}^3$, enclosed by a surface $\partial\Omega$ where the measurements of the field are taken. Let us assume that the spatial distribution of the sources is given by a set of points at locations $\{\mathbf{r}_m\}_{m=1}^M \in \Omega$ and weights $\{s_m\}_{m=1}^M$. In particular, these weights represent the signal's temporal Fourier transform at the corresponding angular frequency ω . Hence, the total source distribution inside Ω is then described by

$$Q(\mathbf{r}, \omega) = \sum_{m=1}^M s_m(\omega) \delta(\mathbf{r} - \mathbf{r}_m), \quad (5.8)$$

where the only free parameters in the signal $Q(\mathbf{r}, \omega)$ are the locations \mathbf{r}_m and the Fourier coefficients of the m^{th} source signal for a given frequency ω . The generated wave field according to (5.1) is observed with some detectors located $\{\mathbf{r}_d\}_{d=1}^D \in \partial\Omega$ known by the measurement setup. Finally, the problem can be stated as follows.

Problem 2. *Given a set of measurements of a propagating wave field $U(\mathbf{r}, \omega)$ and its normal derivative $\partial U(\mathbf{r}, \omega)/\partial n'$ for a set of points \mathbf{r}_d on $\partial\Omega$, find the source locations $\{\mathbf{r}_m\}_{m=1}^M \in \Omega$ and the weights $s_m(\omega)$ in (5.8) satisfying (5.2).*

5.2.2 Sensing kernels

We start by defining the *Sensing Principle* as the contribution where the current work differentiates from the classical FRI-sampling problems.

Definition 3 (Sensing Function). *Let Ψ be a function that satisfies*

$$\nabla^2 \Psi(\mathbf{r}, \omega) + \frac{\omega^2}{c^2} \Psi(\mathbf{r}, \omega) = 0 \text{ in } \Omega, \quad (5.9)$$

*then we coin the term **sensing function** for Ψ .*

Proposition 4. *Assuming the field and the normal derivative of the wave field are available on the boundary $\partial\Omega$, and one chooses a sensing function Ψ satisfying (5.9), then one can “sense” the source signal through the surface integral:*

$$\langle \Psi, Q \rangle = \oint_{\partial\Omega} \left[\Psi(\mathbf{r}, \omega) \frac{\partial}{\partial n} U(\mathbf{r}, \omega) - U(\mathbf{r}, \omega) \frac{\partial}{\partial n} \Psi(\mathbf{r}, \omega) \right] dS, \quad (5.10)$$

*where the partial derivatives $\frac{\partial}{\partial n}$ are directed outward (from the interior to exterior) and we call $\langle \Psi, Q \rangle$ the **generalized samples** to differentiate from the field measurements.*

Proof. Let $\Psi(\mathbf{r}, \omega)$ and $U(\mathbf{r}, \omega)$ be any two complex functions of position, and $\partial\Omega$ be a closed surface surrounding a volume Ω . If $\Psi(\mathbf{r}, \omega)$, $U(\mathbf{r}, \omega)$, and their first and second partial derivatives are well-defined within Ω and on $\partial\Omega$, respectively, then the second Green's identity states that

$$\int_{\Omega} (U\nabla^2\Psi - \Psi\nabla^2U) dV = \oint_{\partial\Omega} \left(\Psi \frac{\partial}{\partial n} U - U \frac{\partial}{\partial n} \Psi \right) ds. \quad (5.11)$$

When the sensing function Ψ is chosen to satisfy (5.9), we obtain

$$\oint_{\partial\Omega} \left(\Psi \frac{\partial}{\partial n} U - U \frac{\partial}{\partial n} \Psi \right) \cdot ds = \int_{\Omega} \Psi(\mathbf{r}, \omega) Q(\mathbf{r}, \omega) d\mathbf{r} \quad (5.12)$$

$$= \langle \Psi, Q \rangle. \quad (5.13)$$

Hence, the sensing principle that follows from the second Green's identity allows extracting generalized samples of the source term with the sensing function, which creates a link between the model parameters and the measurements on the surface. \square

Many functions that satisfy the Strang–Fix conditions can be extended to multidimensional space by the tensor product [19]. For example, symmetric B-splines, biorthogonal B-splines and orthogonal Daubechies scaling functions [98]. Moreover, there have been various attempts to define functions that satisfy generalized Strang–Fix conditions for scattered data quasi-interpolation [99]. However, the condition that is given by (5.9) prevents straightforward extension of the FRI–theory to multidimensional sensing problems. For that reason, we propose various families of sensing functions that split the problem into pieces in which there exist efficient algorithms to retrieve the innovations of the signal.

Proposition 5 (Sensing functions based on 2D harmonics). *Let $\phi(x, y)$ be a solution to $\nabla^2\phi(x, y) = 0$, then any function*

$$\Psi(x, y, z) = e^{\pm ikz} \phi(x, y) \quad (5.14)$$

would be a solution of the sensing equation given in (5.9).

Proof. Choosing Ψ as in (5.14) and developing (5.9), we have:

$$\begin{aligned} [\nabla^2 + k^2] \Psi(x, y, z) &= \left[\frac{\partial^2}{\partial x^2} + \frac{\partial^2}{\partial y^2} + \frac{\partial^2}{\partial z^2} + k^2 \right] e^{\pm ikz} \phi(x, y) \\ &= e^{\pm ikz} \underbrace{\left[\frac{\partial^2}{\partial x^2} + \frac{\partial^2}{\partial y^2} \right] \phi(x, y)}_{=0} + [(\pm ik)^2 + k^2] e^{\pm ikz} \phi(x, y) \\ &= 0. \end{aligned}$$

The term that appears to be zero in the second line is a harmonic function by definition. If the harmonic function possesses a singularity, it has to be outside of the domain Ω to satisfy (5.9) as to remain a valid sensing function. \square

Now, we consider the sensing function in (5.14) and we ask the question whether the harmonic part of the sensing function $\phi(x, y)$ can satisfy the Strang–Fix conditions to reproduce some polynomials or exponentials.

(a) *Polynomial reproducing kernels:* Consider any compactly supported kernel given by the tensor product of two 1-D functions $\phi(x)$ and $\phi(y)$ that can reproduce polynomials x^α and y^β , respectively, where $\alpha, \beta \in \{1, \dots, n\}$ and $x, y \in \mathbb{R}$. Assuming unit sampling period along each direction, this means that the kernel $\varphi(x, y)$ satisfies

$$\sum_j \sum_k C_{j,k}^{\alpha,\beta} \phi(x-j, y-k) = x^\alpha y^\beta, \quad (5.15)$$

where α and β are the degrees of the polynomials that the kernel can reproduce along x - and y -directions.

Proposition 6. *There is no kernel that can reproduce real polynomials of degree more than 2 that will satisfy both the sensing principle (5.9) and the Strang-Fix conditions (5.15).*

Proof. Let $\phi(x, y)$ be the harmonic function; i.e., $\nabla^2\phi(x, y) = 0$ in Ω . Hence, (5.15) must satisfy the same equation

$$\begin{aligned} \text{LHS} &= \sum_j \sum_k C_{j,k}^{\alpha,\beta} \nabla^2 \phi(x-j, y-k) = 0 \\ \text{RHS} &= \nabla^2 x^\alpha y^\beta = \alpha(\alpha-1)x^{\alpha-2}y^\beta + \beta(\beta-1)x^\alpha y^{\beta-2}. \end{aligned}$$

The RHS is zero only for $\alpha, \beta \in \{0, 1\}$, which yields a contradiction for polynomials of degree $n \geq 2$. \square

- (b) *Exponential reproducing kernels:* Consider any compactly supported kernel given by the tensor product of two 1-D functions $\phi(x)$ and $\phi(y)$ that can reproduce exponentials $e^{\alpha_p x}$ and $e^{\beta_q y}$, respectively, where $\alpha_p = \alpha_0 + p\lambda, \beta_q = \beta_0 + q\gamma$ with $p, q \in \{1, \dots, n\}$ and $x, y \in \mathbb{R}$. Assuming unit sampling interval along each direction, this means that the kernel $\phi(x, y)$ satisfies

$$\sum_r \sum_s C_{r,s}^{p,q} \phi(x-r, y-s) = e^{\alpha_p x} e^{\beta_q y}, \quad (5.16)$$

where α and β are the degrees of the exponentials that the kernel can reproduce along x - and y -directions.

Proposition 7. *There exist kernels that can reproduce exponentials that will satisfy both the sensing principle (5.9) and the Strang-Fix conditions (5.15) provided that $\alpha_p = \pm i\beta_q$ for all p, q .*

Proof. Let $\varphi(x, y)$ be the harmonic function; i.e., $\nabla^2\phi(x, y) = 0$ in Ω . Hence, (5.16) must satisfy the same equation

$$\begin{aligned} \text{LHS} &= \sum_r \sum_s C_{r,s}^{p,q} \nabla^2 \phi(x-r, y-s) = 0 \\ \text{RHS} &= \nabla^2 e^{\alpha_p x} e^{\beta_q y} = (\alpha_p^2 + \beta_q^2) e^{\alpha_p x} e^{\beta_q y} = 0. \end{aligned}$$

\square

Consider a general harmonic function that has no singularity in Ω and a stream of Diracs with $Q(\mathbf{r}, \omega) = \sum_{m=1}^M s_m(\omega) \delta(\mathbf{r} - \mathbf{r}_m)$ for a given frequency ω , $\mathbf{r}^T = [x, y, z]$ and $\mathbf{r}_m^T = [x_m, y_m, z_m]$. We consider the generalized samples on a uniform grid given by

$$\begin{aligned} M_{r,s} &= \left\langle Q(\mathbf{r}, \omega), \Psi \left(\frac{x}{T_x} - r, \frac{y}{T_y} - s, z \right) \right\rangle \\ &= \iiint_{\mathbb{R}^3} Q(\mathbf{r}, \omega) \phi \left(\frac{x}{T_x} - r, \frac{y}{T_y} - s \right) e^{\pm ikz} dx dy dz \end{aligned} \quad (5.17)$$

where $T_x, T_y \in \mathbb{R}^+$ are the sensing intervals along x - and y -directions.

Consider a set of 3-D Dirac distribution $Q(\mathbf{r}, \omega) = \sum_{m=1}^M s_m(\omega) \delta(\mathbf{r} - \mathbf{r}_m)$ for a given frequency ω , $\mathbf{r}^T = [x, y, z]$ and $\mathbf{r}_m^T = [x_m, y_m, z_m]$. Here, we provide an algorithm in the classical FRI-fashion and we refer to Chapter 2 for the details of the method.

- 1) *Retrieve the FRI samples of the signal:* We denote, $\mu_{p,q} = \sum_r \sum_s C_{r,s}^{p,q} M_{r,s}$, the weighted sum of the generalized samples, where the coefficients $C_{r,s}^{p,q}$ are computed by imposing (5.16) that reproduce $e^{\alpha_p x} e^{\beta_q y}$. We have

$$\begin{aligned}
\mu_{p,q} &= \sum_r \sum_s C_{r,s}^{p,q} M_{r,s} \\
&\stackrel{(a)}{=} \sum_r \sum_s C_{r,s}^{p,q} \left\langle Q(\mathbf{r}, \omega), \Psi \left(\frac{x}{T_x} - r, \frac{y}{T_y} - s, z \right) \right\rangle \\
&\stackrel{(b)}{=} \left\langle Q(\mathbf{r}, \omega), e^{\pm ikz} \sum_r \sum_s C_{r,s}^{p,q} \phi \left(\frac{x}{T_x} - r, \frac{y}{T_y} - s \right) \right\rangle \\
&\stackrel{(c)}{=} \left\langle \sum_{m=1}^M s_m(\omega) \delta(\mathbf{r} - \mathbf{r}_m), e^{\pm ikz} e^{\alpha_p x} e^{\beta_q y} \right\rangle \\
&\stackrel{(d)}{=} \sum_{m=1}^M s_m(\omega) e^{\pm ikz_m} e^{\alpha_p x_m} e^{\beta_q y_m}
\end{aligned} \tag{5.18}$$

where (a) follows from the definition of $M_{r,s}$ in (5.17), (b) from the definition of Ψ in (5.14); (c) from the definition of $Q(\mathbf{r}, \omega)$ and (d) from the exponential reproducing property in (5.16).

- 2) *Annihilation along x - and y - axis:* Note that (5.18) can be written as a power series

$$\mu_{p,\cdot} = \sum_{m=1}^M c_m u_m^p \tag{5.19}$$

with $c_m = s_m(\omega) e^{\pm ikz_m} e^{\beta_q y_m + \alpha_0 x_m}$ and $u_m = e^{\lambda x_m}$. Here, the choice $\alpha_p = \alpha_0 + p\lambda$ makes the sum as a power series that can be annihilated with an annihilating filter. Hence the sequence $\{x_m\}_{m=1}^M$ can be retrieved from the FRI-samples $\mu_{p,q}$ using the annihilating filter method also known as Prony's method [28]. Let h_p with $p = 0, \dots, P$, be the filter with z -transform $H(z) = \sum_{p=0}^M h_p z^{-p} = \prod_{m=1}^M (1 - u_m z^{-1})$, that is its roots correspond to the values u_m to be found. Then, it follows that h_p annihilates the observed sequence $\mu_{p,\cdot}$:

$$h_p * \mu_{p,\cdot} = \sum_{i=0}^M h_i \mu_{p-i,\cdot} = \sum_{m=1}^M c_m u_m^p \underbrace{\sum_{i=1}^M h_i u_m^{-i}}_{H(u_m)} = 0. \tag{5.20}$$

Then, the zeros of this filter uniquely defines the values u_m provided that the x_m 's are distinct. Moreover, the same procedure can be followed to retrieve the innovations $\{y_m\}_{m=1}^M$ by defining another annihilating filter h_q to annihilate $\mu_{\cdot,q}$ with the choice $\beta_q = \beta_0 + q\gamma$.

As a final remark for this section, we note that the origin of the sensing grid and step size T_x and T_y have to be chosen such that there exist no singularity in the volume Ω so that (5.9) will be satisfied for every sensing point of the grid in case the function ϕ possesses a singularity.

- (c) *Holomorphic kernels:* We now propose to work with holomorphic functions that are a subset of harmonic functions rather than the general harmonic functions. We first note that this allows to reduce the dimension of the problem, that is, the pairs $\{x_m, y_m\}_{m=1}^M$ will be represented by complex numbers $\xi_m = x_m + iy_m$. Then, we showed that the exponential reproduction constraint of part (b) can be relaxed with a proper design of sensing positions of

the generalized samples. We propose to take these samples at equidistant angles (using polar representation) on the complex domain that will allow to construct an annihilation filter a priori so that the parameters of a characteristic polynomial in which the zeros are defined as the positions on the complex plane can be retrieved using a non-iterative algorithm.

We start by noting that, if a complex-valued function $\varphi(\xi)$ of a single complex variable $\xi = x + iy$ is complex differentiable (i.e., holomorphic), then it is also a harmonic function, i.e., $\nabla^2\varphi = 0$, [100]. Polynomial functions in ξ with complex coefficients, sine, cosine and the exponential function are some examples of holomorphic functions on \mathbb{C} . In this work, we only consider N -th degree polynomials given by

$$\varphi(\xi) = \sum_{l=0}^N \chi_l \xi^l = \prod_{l=1}^N (\xi - s_l) \text{ with } \chi_N = 1, \quad (5.21)$$

where s_l are the zeros of the holomorphic functions that are located on the complex plane in a region S_φ with a radius $s_\varphi = \max_l |s_l|$. Then, we propose to introduce the zeros of the holomorphic function as the poles of the sensing function

$$\Psi(\xi, z) = e^{ikz} (\varphi(\xi))^{-1}, \quad (5.22)$$

such that one can acquire the generalised samples by

$$\mu_n = \langle Q(\mathbf{r}), \Psi(\xi - a_n, z) \rangle, \quad (5.23)$$

where the sensing positions, (i.e., $a_n = r_n e^{i\alpha_n}$), are not on a uniform grid on the complex plane, but located at equidistant angles satisfying $\alpha_n = \alpha_0 + \lambda n$ with arbitrary α_0, λ and $r_n \geq s_\varphi + R$ with R being the radius of the volume Ω to ensure that no singularity exists in the volume for different sensing positions.

Proposition 8. *Consider a stream of 3-D Diracs*

$$Q(\mathbf{r}, \omega) = \sum_{m=1}^M s_m(\omega) \delta(\mathbf{r} - \mathbf{r}_m)$$

for a given frequency ω , $\mathbf{r}^T = [x, y, z]$ and $\mathbf{r}_m^T = [x_m, y_m, z_m]$, the 3-D complex sensing functions in (5.22) that are designed using the holomorphic functions that introduce N -th order poles allow a non-iterative reconstruction algorithm to retrieve the locations of the sequence $\{\xi_m = x_m + iy_m\}_{m=1}^M$.

Proof. The sensing samples in (5.23) will satisfy

$$\mu_n = \left\langle Q(\mathbf{r}, \omega), \frac{e^{ikz}}{\varphi(\xi - a_n)} \right\rangle \quad (5.24)$$

$$\stackrel{(a)}{=} \sum_{m=1}^M \frac{s_m(\omega) e^{ikz_m}}{\varphi(\xi_m - a_n)} \quad (5.25)$$

$$\stackrel{(b)}{=} \frac{\sum_{m=1}^M s_m(\omega) e^{ikz_m} \prod_{i \neq m}^M \varphi(\xi_i - a_n)}{\prod_{m=1}^M \varphi(\xi_m - a_n)} \quad (5.26)$$

$$\stackrel{(c)}{=} \frac{\sum_{m=1}^M s_m(\omega) e^{ikz_m} \prod_{i \neq m}^M \prod_{l=1}^N (\xi_i - s_l - a_n)}{\prod_{m=1}^M \prod_{l=1}^N (\xi_m - s_l - a_n)} \quad (5.27)$$

$$\stackrel{(d)}{=} \frac{\sum_{m=0}^{(M-1)N} s'_m a_n^m}{P(a_n)}, \quad (5.28)$$

where (a) follows from the linearity of the inner product, (b) from combining each terms in (a), (c) from the definition of the φ in (5.21), the numerator of (d) follows from the fact that the numerator of (c) can be rewritten as a polynomial with respect to a_n with at most $(M-1)N$ zeros where s'_m are complex-valued coefficients that do not depend on a_n and the denominator of (d) follows from defining a characteristic polynomial

$$P(x) = \sum_{m=0}^{MN} p_m x^m = \prod_{i=1}^M \prod_{l=1}^N (\xi_m - s_l - x) \quad (5.29)$$

where p_m are the coefficients to be found such that $p_{MN} = 1$. Then, defining a new sequence

$$u_n = \mu_n P(a_n) = \sum_{m=1}^{(M-1)N} s'_m a_n^m = \sum_{m=1}^{(M-1)N} c'_m u_m^n, \quad (5.30)$$

where $c'_m = s'_m r_n e^{i\alpha_0 m}$ and $u_m = e^{i\lambda m}$. Here, the choice $\alpha_n = \alpha_0 + n\lambda$ makes u_n as a power series that can be annihilated with a known annihilating filter given by its z -transform

$$H(z) = \sum_{k=0}^M h_k z^{-k} = \prod_{m=0}^M (1 - e^{i\lambda m} z^{-1}).$$

Hence, the problem reduces to finding the polynomial coefficients (5.29), from the annihilation system given by $\{h * u\}_n = 0$ so that the zeros of the polynomial will give the locations $\xi_m = x_m + iy_m$ for $m = 1, \dots, M$ provided that ξ_m 's are distinct. \square

It is worth mentioning that the choice of the projection plane that is determined by the holomorphic function is arbitrary and it could have been chosen as XZ or YZ planes rather than XY plane. Indeed, any orientation can be applied to the sensing functions using standard rotation matrices about x -, y -, and z -axis, which will be further developed in the following section.

5.3 Proof-of-concept validation

In this chapter, we develop a practical algorithm to retrieve the parameters of a stream of 3-D Diracs from the samples of induced field on a given measurement boundary. In particular, we choose to work with a specific holomorphic function that introduces a first-order pole at the origin; i.e., using the convention from the previous section we choose $\varphi(\xi) = \xi$ where the complex variable is defined as $\xi = x + iy$. Moreover, we provide the details of the implementation with experimental results.

5.3.1 Sensing step

In Section 5.2 we proposed to use novel sensing kernels that are derived from holomorphic functions in complex domain. Now, we consider a general *spherical* sampling geometry and restrict our choice of the sensing function based on the following lemma.

Lemma 2. *Let $a \in \mathbb{C}$ and $\mathbf{r} = [x, y, z]^T$, then*

$$\psi(x, y, z) = \frac{e^{i\omega z/c}}{x + iy - a}, \quad a \notin \Omega \quad (5.31)$$

is a valid sensing function that belongs to the set of functions defined by (5.9).

An instance of the proposed test function is visualized on the measurement surface in Fig. 5.2.

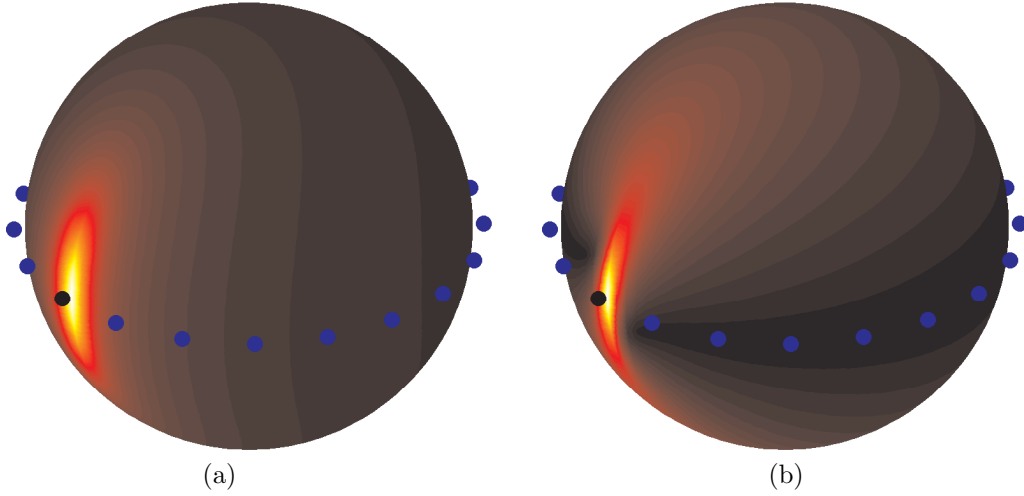


Figure 5.2: Visualization for the sensing function on the measurement surface Ω where the dots around the volume indicate the different sensing positions (i.e., a_n). The chosen sensing position is shown in dark. (a) Sensing function. (b) Normal derivative of the sensing function.

5.3.2 Annihilation step

Proposition 9. *Let ψ_n be a set of sensing functions in Lemma 2 for $n = 0, \dots, N-1$ with a_n 's located with equidistant radial angle, θ on the complex plane, then, the set of generalized samples can be annihilated to find the projections of the source points onto complex plane.*

Proof. We choose N points on the complex plane to define the family of sensing functions in the form $a_n = \alpha_n e^{in\theta}$ for some angle θ with α_n 's are greater than the radius of the measurement surface to satisfy the Lemma 2.

Then, defining a polynomial $R(a_n) = \sum_{m=0}^M r_m a_n^m = \prod_{m=1}^M (x_m + iy_m - a_n)$ with $r_M = 1$ and an FIR filter, h with zeros at $e^{ik\theta}$ given by $H(z) = \sum_{k \in \mathbb{Z}} h[k] z^{-k} = \prod_{k=0}^{M-1} (1 - e^{ik\theta} z^{-1})$, then the set of generalized samples can be reinterpreted as

$$\begin{aligned}
 \mu_n = \langle \psi_n, Q \rangle &= \sum_{m=1}^M s_m \frac{e^{ikz_m}}{x_m + iy_m - a_n}, \\
 &= \frac{\sum_{m=0}^{M-1} s'_m e^{inm\theta}}{\prod_{m=1}^M (x_m + iy_m - a_n)}, \\
 &= \frac{\sum_{m=0}^{M-1} s'_m e^{inm\theta}}{R(a_n)}.
 \end{aligned} \tag{5.32}$$

Then, the predefined filter h annihilates the sequence, $u_n = \{R(a_n)\mu_n\}$ for $n = M, \dots, N-1$,

$$\begin{aligned}
0 = \{h * u\}_n &= \sum_{n'=0}^{N-1} h_{n-n'} R(a_{n'}) \mu_{n'} \\
&= \sum_{n'=0}^{N-1} h_{n-n'} \sum_{k=0}^M r_k a_{n'}^k \mu_{n'} \\
&= \sum_{k=0}^M r_k \sum_{n'=0}^{N-1} h_{n-n'} a_{n'}^k \mu_{n'} \\
&= \sum_{k=0}^M A_{n,k} r_k.
\end{aligned} \tag{5.33}$$

□

In matrix representation, (5.33) can be represented as

$$\mathbf{A}\mathbf{r} = \mathbf{H}\mathbf{D}\mathbf{V}\mathbf{r} = \mathbf{0}, \tag{5.34}$$

where \mathbf{H} is an $(N-M) \times N$ Toeplitz matrix representing the annihilating filter h , \mathbf{D} is an $N \times N$ diagonal matrix of the generalized samples, \mathbf{V} is an $N \times (M+1)$ Vandermonde matrix of poles of the sensing function and \mathbf{r} is the unknown vector of $M+1$ polynomial coefficients with $r_M = 1$. Explicitly, the system matrix \mathbf{A} in (5.34) is decomposed as

$$\underbrace{\begin{bmatrix} h_M & \cdots & h_0 & 0 & \cdots & 0 \\ 0 & h_M & \cdots & h_0 & \cdots & 0 \\ \vdots & \vdots & \ddots & \vdots & \vdots & \vdots \\ 0 & \cdots & 0 & h_M & \cdots & h_0 \end{bmatrix}}_{\mathbf{H}} \underbrace{\begin{bmatrix} \mu_0 & 0 & \cdots & 0 \\ 0 & \mu_1 & \cdots & 0 \\ \vdots & \vdots & \ddots & \vdots \\ 0 & \cdots & \cdots & \mu_{N-1} \end{bmatrix}}_{\mathbf{D}} \underbrace{\begin{bmatrix} a_0^0 & a_0^1 & \cdots & a_0^M \\ a_1^0 & a_1^1 & \cdots & a_1^M \\ \vdots & \vdots & \ddots & \vdots \\ a_{N-1}^0 & \cdots & \cdots & a_{N-1}^M \end{bmatrix}}_{\mathbf{V}} \tag{5.35}$$

which indicates that \mathbf{A} is rank deficient in the ideal case; i.e., $\text{rank}(\mathbf{A}) = M$ and \mathbf{r} admits a solution in the nullspace of \mathbf{A} . Therefore, we can find the solution \mathbf{r} by performing an SVD of the system matrix \mathbf{A} and choosing the column vector corresponding to the smallest singular value. Once the unknown polynomial coefficients satisfying (5.34) are obtained, the projection of the source point onto complex plane is found as the roots of the polynomial $R(a_n)$.

Lemma 3. *Let the locations of the point sources be distinct, then the system matrix in (5.34) is of rank M for the noiseless case.*

Proof. The system matrix in (5.34) has $(N-M)$ equations with M unknowns of the characteristic polynomial $R(a_n)$ defined in Proposition 9 with $r_M = 1$. Then, the minimum number of generalized samples should be $N = 2M$. Hence, we conclude that the system matrix \mathbf{A} in (5.34) is rank M for distinct source positions. □

5.3.3 Practical recovery in 3-D

We propose a three-step algorithm to locate the 3-D locations of the point sources from the measured field by means of applying the sensing principle.

Planar Projection

In the first step, we choose a set of sensing functions Ψ as in (5.31) in a general X'Y'Z' coordinate system that we obtain by applying general rotation matrices along X and Y-axes [101].

$$\Psi_n(\mathbf{R}\mathbf{r}, \omega) = \frac{e^{j\omega z'/c}}{x' + jy' - a_n}, \quad a_n \notin \Omega, \quad (5.36)$$

where a_n 's are the poles of the sensing function on $X'Y'$ -plane located at equidistant angles $a_n = ae^{jn\theta}$, $n \in \llbracket 0, N-1 \rrbracket$, $|a|$ is greater than the radius of Ω excluding the volume and θ is an arbitrary angle. The matrix \mathbf{R} represents the rotation matrix of the coordinate system along the X and Y axes in a standard right-handed cartesian coordinate system given by

$$\underbrace{\begin{bmatrix} x' \\ y' \\ z' \end{bmatrix}}_{\mathbf{r}'} = \underbrace{\begin{bmatrix} 1 & 0 & 0 \\ 0 & \cos \alpha & \sin \alpha \\ 0 & -\sin \alpha & \cos \alpha \end{bmatrix}}_{\mathbf{R}_X(\alpha)} \underbrace{\begin{bmatrix} \cos \beta & 0 & -\sin \beta \\ 0 & 1 & 0 \\ \sin \beta & 0 & \cos \beta \end{bmatrix}}_{\mathbf{R}_Y(\beta)} \underbrace{\begin{bmatrix} x \\ y \\ z \end{bmatrix}}_{\mathbf{r}}. \quad (5.37)$$

Then, by solving the annihilation system in Proposition 9, we find the projections of the point source positions on the corresponding $X' Y'$ -plane defined by the rotation matrix.

Pairing of the Projections

In the second step, we propose a greedy approach to build a manifold of projections to keep the solutions paired between each projection. For each 2-D projection, the locations are found as the roots of a polynomial as described in Proposition 9. However, the sources of each projection are not ordered in the same way. In the ideal case, at least 2 orthogonal projections of the distribution would be sufficient to solve for the 3-D problem. However, to the best of our knowledge there is no efficient solution for this problem under the effect of noise or measurement error.

We propose a solution for the closest pair problem for two separated sets of points between consecutive projection planes. Indeed, the main idea is to compute the Euclidean distance in \mathbb{R}^3 between all the pairs of points in two projection sets and then to group the pairs with respect to the mutually smallest distance criteria [102, 103].

Consider $A \times B$ projection planes defined by $\mathbf{R}(\alpha_i, \beta_j)$ $i \in \llbracket 0, A-1 \rrbracket$ $j \in \llbracket 0, B-1 \rrbracket$ where each plane has M projected points to be paired. We assume an initial labeling for the points of the first plane with l_1 to l_M . Then, to find the pair of closest points $p \in P_k$ and $q \in P_{k-1}$ $k \in \llbracket 2, A \times B \rrbracket$, we compute the distances between all the $M \times M$ pairs of points and we pick and label the pair with the smallest distance and exclude it from the set.

In a similar way, the idea can be generalized for a rotation along X - and Y -axis using a selective projection approach. We propose to selectively project onto planes such that the incremental change between the planes remains minimal. Hence, the Euclidean distance still achieves a good measure to pair the projections between two consecutive projections.

We note that in practice, projection angles along X - and Y -axis do not have to be different due to the fact that the projection is done on a complex plane and only the distance of each source point to the measurement surface matters in reconstruction quality. Hence, choosing the rotation matrix $\mathbf{R}(\alpha, \alpha)$ achieves sufficiently good results.

We provide a summary of the method in Algorithm 7 and we note that the proposed pairing method is computed in $\mathcal{O}(n^2)$ but can be solved in $\mathcal{O}(n \log n)$ using the recursive divide and conquer approach [103].

Reconstruction in 3-D

In the third step, we solve for the 3D positions of the point sources by a least-squares regression of the 2D projections as a special case of tomographic reconstruction. Indeed, once the pairing of the projections for each rotation matrix is known after the second step of the algorithm, one

Algorithm 7 Pair of closest Points**Require:** $p \in P_i$, for $i \in \llbracket 0, P-1 \rrbracket$ **Require:** l_p : Labels of $p \in P_i$ 1: **Initialization:** Label l_0 : 1 to M2: **for** $i=1$ to $P-1$ **do**3: $P_i^* = P_i$ 4: **while** P_i^* is not empty **do**5: $p^* = \operatorname{argmin}_{p \in P_i^*} \min_{q \in P_{i-1}} \|f(p) - f(q)\|^2$ 6: $P_i^* = P_i^* \setminus \{p^*\}$ 7: **end while**8: Label l_i : Match the labels of p^* and q 9: **end for**

can represent each 2D projections with

$$\underbrace{\begin{bmatrix} x_m^k \\ y_m^k \end{bmatrix}}_{\xi_m^k} = \underbrace{\begin{bmatrix} 1 & 0 & 0 \\ 0 & 1 & 0 \end{bmatrix}}_{\mathbf{P}^k} \mathbf{R}(\alpha_i, \beta_j) \underbrace{\begin{bmatrix} x_m \\ y_m \\ z_m \end{bmatrix}}_{\mathbf{r}_m}, \quad (5.38)$$

$$k = i \times A + j, \quad i \in \llbracket 0, A-1 \rrbracket, \quad j \in \llbracket 0, B-1 \rrbracket$$

where $\mathbf{R}(\alpha_i, \beta_j)$ characterizes a set of rotations, k is the index for the selective projection order and ξ_m^k is the projection of the point source \mathbf{r}_m on the plane denoted by k . Finally, we solve for the following least squares problem

$$\hat{\mathbf{r}}_m = \operatorname{argmin}_{\mathbf{r}_m} \sum_{k=0}^{P-1} \|\xi_m^k - \mathbf{P}^k \mathbf{r}_m\|_2^2, \quad \forall m \in \llbracket 1, M \rrbracket. \quad (5.39)$$

A note on the missing Fourier coefficients

In order to completely describe the source distribution, one still has to determine the temporal Fourier coefficients $s_m(\omega)$. The estimation of these parameters can be done with the same set of *generalized samples*. Considering the estimated locations, the generalised samples will be a linear set of equations to be solved for $s_m(\omega)$

$$\mu_n = \langle \psi_n, Q \rangle = \sum_{m=1}^M s_m(\omega) \underbrace{\frac{e^{ikz_m}}{x_m + iy_m - a_n}}_{\text{estimated}}, \quad n \in \llbracket 1, N \rrbracket, \quad (5.40)$$

where μ_n are the generalized samples and x_m, y_m and z_m are the estimated 3-D positions of the source.

In Figure 5.3, we provide a schematic overview of the proposed algorithm for the recovery of the parameters of a source distribution given as a set of 3-D Diracs.

5.3.4 Alternative 3-D recovery method

The pairing algorithm of the projections relies on a closest pair approach based on the Euclidean distance. This heuristic algorithm performs well even if the measurements are degraded by noise. However, we also propose an alternative two-step algorithm based on applying the sensing principle in two steps with two different sensing functions, consecutively. In particular, in the

first step, we extract the projected positions on the complex plane using the Proposition 9. Then, using the projected locations on XY-plane, the same generalized samples as in (5.32) are now used to solve another linear system of equations to extract the weights of the point sources. Hence, this system will satisfy

$$\underbrace{\langle \Psi_n^{(1)}, Q \rangle}_{\text{known}} = \mu_n = \sum_{m=1}^M \frac{p_m}{\underbrace{x_m + iy_m}_{\text{projected locs.}} - a_n}, \quad p_m = s_m e^{ikz_m}. \quad (5.41)$$

where we redefine p_m as a complex variable to be solved and we assume $s_m \in \mathbb{R}$ in this case. In matrix notation, we can express this system as $\mathcal{B}\mathbf{p} = \mu$, where \mathcal{B} is an $N \times M$ matrix with the entries $\mathcal{B}_{m,n} = \frac{1}{x_m + iy_m - a_n}$, and \mathbf{p} is an $M \times 1$ vector with entries $p_m = c_m e^{ikz_m}$ and μ is an $N \times 1$ vector with entries μ_n . Then, we propose to recover the remaining z-locations by means of applying the sensing principle with a proper set of plane waves (note that these sensing functions do not have spatial concentration (i.e., the locality)):

$$\Psi_n^{(2)}(\mathbf{r}) = e^{i(k_x x + k_y y + k_z z)/c}, \quad \text{s.t. } k_x^2 + k_y^2 + k_z^2 = k^2, \quad (5.42)$$

where $k_z < \frac{\pi}{R_o}$, R_o being the radius of the volume of interest, and $(k_x, k_y) = \sqrt{k^2 - k_z^2}(\cos \alpha_n, \sin \alpha_n)$, $\alpha_n = \frac{2\pi}{N}n$, $n \in \llbracket 0, N-1 \rrbracket$. With this selection of the proposed family of plane waves, the extracted samples of the source function become

$$\begin{aligned} \langle \Psi_n^{(2)}, Q \rangle &= \sum_{m=1}^M s_m e^{i(k_x x_m + k_y y_m + k_z z_m)} \\ &= \sum_{m=1}^M \underbrace{s_m e^{i(k_x x_m + k_y y_m)}}_{C'_{m,n}} Z_m, \quad Z_m = e^{ik_z z_m} \end{aligned} \quad (5.43)$$

where we redefine Z_m to be unknown. By construction, the phase of the solution is uniquely determined due to the choice k_z , which guarantees a unique solution in the domain, hence

$$z_m = \frac{\arg(Z_m)}{k_z}, \quad (5.44)$$

where Z_m is the solution of the sensing equation (5.43).

5.3.5 Measurement noise and model mismatch

The algorithm explained so far assumes perfect data, but in practice the set of measurements of the propagating wave field $U(\mathbf{r}, \omega)$ and its normal derivative $\partial U(\mathbf{r}, \omega)/\partial n'$ are corrupted with measurement noise. Hence, the generalized samples by the surface integral in (5.10) will be degraded by noise,

$$\tilde{\mu}_n = \mu_n + \varepsilon_n, \quad (5.45)$$

where ε_n corresponds to the complex noise in the generalized samples. Hence, in the presence of noise, the system matrix

$$\tilde{\mathbf{A}} = \mathbf{H}\tilde{\mathbf{D}}\mathbf{V} \quad (5.46)$$

becomes full rank and will not satisfy (5.34) anymore due to the degradation of the generalized samples. Moreover, since the system matrix \mathbf{A} does not possess any Toeplitz structure, we cannot directly apply the Cadzow-denoising algorithm from Section 2.3.3, which iteratively imposes the rank deficiency property and the Toeplitz structure of the concerned matrix. Therefore, we propose a modified-Cadzow denoising algorithm in order to compensate for the measurement noise and the model mismatch.

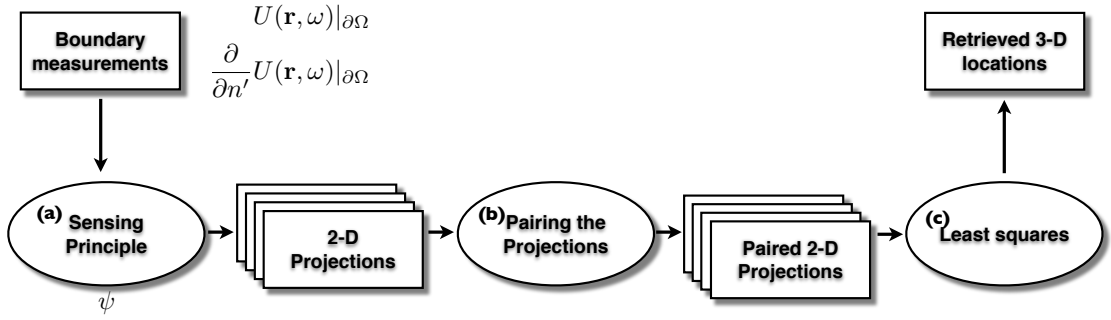


Figure 5.3: Schematic overview of the proposed algorithm to retrieve the locations of a 3-D stream of Diracs from the boundary measurements of an induced field: (a) Find the projected positions on several complex planes by the sensing principle; (b) Pair the projections between each projection plane with respect to the Euclidean distance; (c) Retrieve the 3-D locations by solving a least-squares regression problem.

The convolution matrix \mathbf{H} is in general not unitary, even if it has maximal rank. When the generalized samples are not known with high accuracy, this may distort the recovered polynomial coefficients. Hence, by performing a singular value decomposition of \mathbf{H} , we first replace the convolution matrix with \mathbf{H}_0 such that $\mathbf{H} = \mathbf{U}\mathbf{S}\mathbf{H}_0$ to better condition the system matrix. Next, we observe that the Vandermonde matrix \mathbf{V} can be ill-conditioned in case the angular distances between the singularities of the test pole locations are small. Therefore, we also replace \mathbf{a} by a unitary matrix \mathbf{a}_0 by performing an SVD on \mathbf{V} such that $\mathbf{V} = \mathbf{V}_0\mathbf{\Sigma}\mathbf{M}^*$.

Algorithm 8 Cadzow-like denoising algorithm

Require: Preconditioning of \mathbf{A}

- 1: Replace \mathbf{H} by a unitary matrix \mathbf{H}_0 such that $\mathbf{H} = \mathbf{U}\mathbf{S}\mathbf{H}_0$
 - 2: Replace \mathbf{V} by a unitary matrix \mathbf{V}_0 such that $\mathbf{V} = \mathbf{V}_0\mathbf{\Sigma}\mathbf{M}^*$
 - 3: **for** $i=1$ to **till convergence** **do**
 - 4: Compute $\tilde{\mathbf{A}}_0 = \mathbf{H}_0\tilde{\mathbf{D}}\mathbf{V}_0$
 - 5: Compute low-rank approximation \mathbf{A}_K of $\tilde{\mathbf{A}}_0$
 - 6: Obtain new generalized samples $\tilde{\mathbf{D}}$ by solving (5.47)
 - 7: **end for**
-

The resulting system matrix, $\tilde{\mathbf{A}}_0 = \mathbf{H}_0\tilde{\mathbf{D}}\mathbf{V}_0$ will be used to denoise the generalized samples. In Cadzow-like denoising iterations, we exploit the fact that the system matrix has to remain of rank M at each iteration. Therefore, for any $L > M$, the last $L - M$ singular values of the $\tilde{\mathbf{A}}_0$ are forced to zero to get a low rank approximation of the system matrix, $\hat{\mathbf{A}}$. Then, in the second step, we minimize the following objective

$$\hat{\mathbf{D}} = \arg \min_{\mathbf{D}} \|\mathbf{H}_0\mathbf{D}\mathbf{V}_0 - \tilde{\mathbf{A}}_0\|_F, \quad (5.47)$$

to find a denoised generalized sample by a least squares fit with respect to the Frobenius norm, $\|\cdot\|_F$. The generalized samples and therefore the system matrix can be denoised by iteratively imposing these two steps until convergence. We iterate the scheme until the last $L - M$ singular values of $\hat{\mathbf{A}}$ are smaller than a given threshold; e.g., 10^{-6} . We provide the details of the Cadzow-like denoising scheme in Algorithm 8.

5.4 PAT as a potential application

Photoacoustic tomography (PAT) is a hybrid imaging modality that combines high intrinsic contrast of optical imaging and high spatial resolution of ultrasonic imaging. It is based on the generation of acoustic waves due to the tissue dependent absorption of optical energy. The absorbed energy initially creates a thermally induced pressure jump that leads to an emergence of the propagating acoustic waves in the tissue [104, 105]. Then the activated field is recorded with ultrasound sensors placed on the surface of the volume. The problem is to recover the absorption properties of the tissue from the measured data. Mathematically, this corresponds to the ISP from the measurements of the induced field and, hence fits into our setting with the Helmholtz equation [106].

Numerous approaches have been proposed for the inverse problem of PAT. Many of these algorithms are based on the inversion of the generalized spherical Radon transform and requires the measured data to be densely sampled [96, 107]. Exact analytical solutions in both time and frequency domains are provided assuming continuous aperture with infinite bandwidth [108, 109]. A variety of iterative reconstruction algorithms are proposed to solve the problem for lower sampling density [110, 111], which mostly requires computationally heavy iterations.

5.4.1 Problem setting

In PAT, the optical radiation absorbed by the tissue gives rise to thermal heating. Under the condition of thermal confinement, the tissue subsequently goes into a thermal expansion. The generated acoustic field in which the absorbed energy can be modelled as an heating source is governed by the wave equation

$$\nabla^2 p(\mathbf{r}, t) - \frac{1}{c^2} \frac{\partial^2 p(\mathbf{r}, t)}{\partial t^2} = -\frac{\beta}{C_p} \frac{\partial}{\partial t} H(\mathbf{r}, t), \quad (5.48)$$

where $H(\mathbf{r}, t)$ is the heating function that gives rise to an acoustic field $p(\mathbf{r}, t)$, β is the isobaric volume expansion coefficient [K^{-1}], C_p is the specific heat [$\text{J}/(\text{K kg})$], and c is the speed of sound. Under the thermal confinement condition, the heating function can be further decomposed as the product

$$H(\mathbf{r}, t) = A(\mathbf{r})I(t),$$

where $A(\mathbf{r})$ is the spatial absorption function and $I(t)$ is the temporal illumination function, which is known by the excitation protocol.

In particular, we consider a closed volume of Ω in free space where the optical absorption occurs with a surface $\partial\Omega$ and the activated acoustic field and its normal derivative are measured on the surface of the volume, i.e., $p(\mathbf{r}, t)|_{\partial\Omega}$ and $\nabla p(\mathbf{r}, t)|_{\partial\Omega}$. Then, we parametrize the spatial absorption function as

$$A(\mathbf{r}) = \sum_{m=1}^M s_m \delta(\mathbf{r} - \mathbf{r}_m), \quad (5.49)$$

where $s_m \in \mathbb{R}$, $\mathbf{r}_m \in \Omega$. With this parametrization, the absorption function is completely characterized by the positions and intensities of M sources; i.e., with $4M$ parameters, and the inverse problem becomes well-posed [112]. The key to the reconstruction problem is to recover the spatial absorption function $A(\mathbf{r})$; i.e., the parameters of (5.49) from the boundary measurements of the acoustic field.

5.4.2 Results

We performed numerical experiments to validate our algorithm for a typical PAT setup. Specifically, we considered a spherical geometry of the measurement surface of radius 10 cm that is

assumed to enclose the source function

$$Q(\mathbf{r}) = \sum_{m=1}^M s_m \delta(\mathbf{r} - \mathbf{r}_m).$$

Here, we note that there has been extensive research [113, 114, 115, 116] on the problem that deals with the analysis and design of spherical sensor arrays to allow aliasing-free spatial sampling of the data, if possible, or otherwise with minimal spatial aliasing. However, we would like to repeat (5.10) here to emphasize the fact that the sensing principle relies on the generalized samples of the source function by the following surface integral that links the sampled measurements to the model parameters

$$\mu_n = \langle \psi_n, Q \rangle = \oint_{\partial\Omega} \left[\psi_n(\mathbf{r}, \omega) \frac{\partial}{\partial n} U(\mathbf{r}, \omega) - U(\mathbf{r}, \omega) \frac{\partial}{\partial n} \psi_n(\mathbf{r}, \omega) \right] dS, \quad (5.50)$$

where the partial derivatives $\frac{\partial}{\partial n}$ are directed outward from the interior to exterior. For the current work, we consider that the integral in (5.50) can be taken numerically. In free space, the radiating field $U(\mathbf{r})$ is given by (5.3) and the retarded Green's function as in (5.5). Hence, we compute

$$U(\mathbf{r}) = - \sum_{m=1}^M \frac{s_m}{4\pi} \frac{e^{ik\|\mathbf{r}-\mathbf{r}_m\|}}{\|\mathbf{r}-\mathbf{r}_m\|}, \quad (5.51)$$

which is assumed to be measured by finite sensors located on $\mathbf{r}_d \in \partial\Omega$. We assume that the measurements are degraded by noise such that $\tilde{U}(\mathbf{r}_d)[n] = U(\mathbf{r}_d)[n] + \tilde{v}[n]$, where $v[n]$ is complex AWGN with variance σ^2 such that the real and the imaginary parts of $v[n]$ are uncorrelated and the covariance matrix of noise is given by $\mathbb{R} = \mathbb{E}\{\tilde{\mathbf{v}}\tilde{\mathbf{v}}^H\} = \sigma^2\mathbf{I}$. In Figure 5.4, we illustrate the radiating field and its normal derivative on a spherical measurement surface for a case where the wavenumber is $k = 4188m^{-1}$, which corresponds to a typical temporal frequency of 1 MHz observed in PAT in a medium with a constant speed of sound $c = 1500m/s$ and the measurements are degraded by complex AWGN where the variance is chosen to match the target SNR level. Then, we compute the generalized samples given through the integral (5.50) which is equivalent to the inner product of the source term and the test functions.

Once the generalized samples have been acquired with the sensing step, we first apply the Cadzow-like denoising algorithm to compensate for the measurement noise. Then, the annihilation step follows by constructing the linear system of equations in (5.34) so that the projections on a plane can be retrieved. As we have seen in Section 5.3.2, we first use the Lemma 3 to determine the model order M . In Fig. 5.5 (a), we demonstrate that it is possible to estimate the model order M by observing the decomposition of singular values of the system matrix \mathbf{A} in (5.34). For a 3-D retrieval of the projections, we follow the instructions as in Section 5.3.3. And in Figure 5.5, we provide an instance where the true model has five point sources.

Finally, we provide a few elements to indicate the limitations of our method with PAT. Depending on the application, PAT uses various techniques to tune the imaging depth and the resolution. Then, the generated pressure field is sampled with ultrasound transducers capable of linear/planar measurements of the wave field. Therefore, the normal derivative of the field needs to be approximated from the available data using time- and frequency-domain methods [108]. Moreover, the performance of our method depends on the approximation quality of the surface integral (5.50) which is limited by the current spatial sampling density, the quality of the sensors and the coverage of the measurements on the surface. When the measurements do not cover the entire boundary $\partial\Omega$, and is often , the missing data needs to be taken into account carefully. In order to overcome this shortcoming, the concentration of the sensing functions (locality) can be controlled with the degree of the complex polynomial representing the holomorphic function 5.21. Moreover, with further advancement in photoacoustic imaging technologies, the proposed method indicates great potential to improve the reconstruction quality and performance of the PAT imaging systems [117].

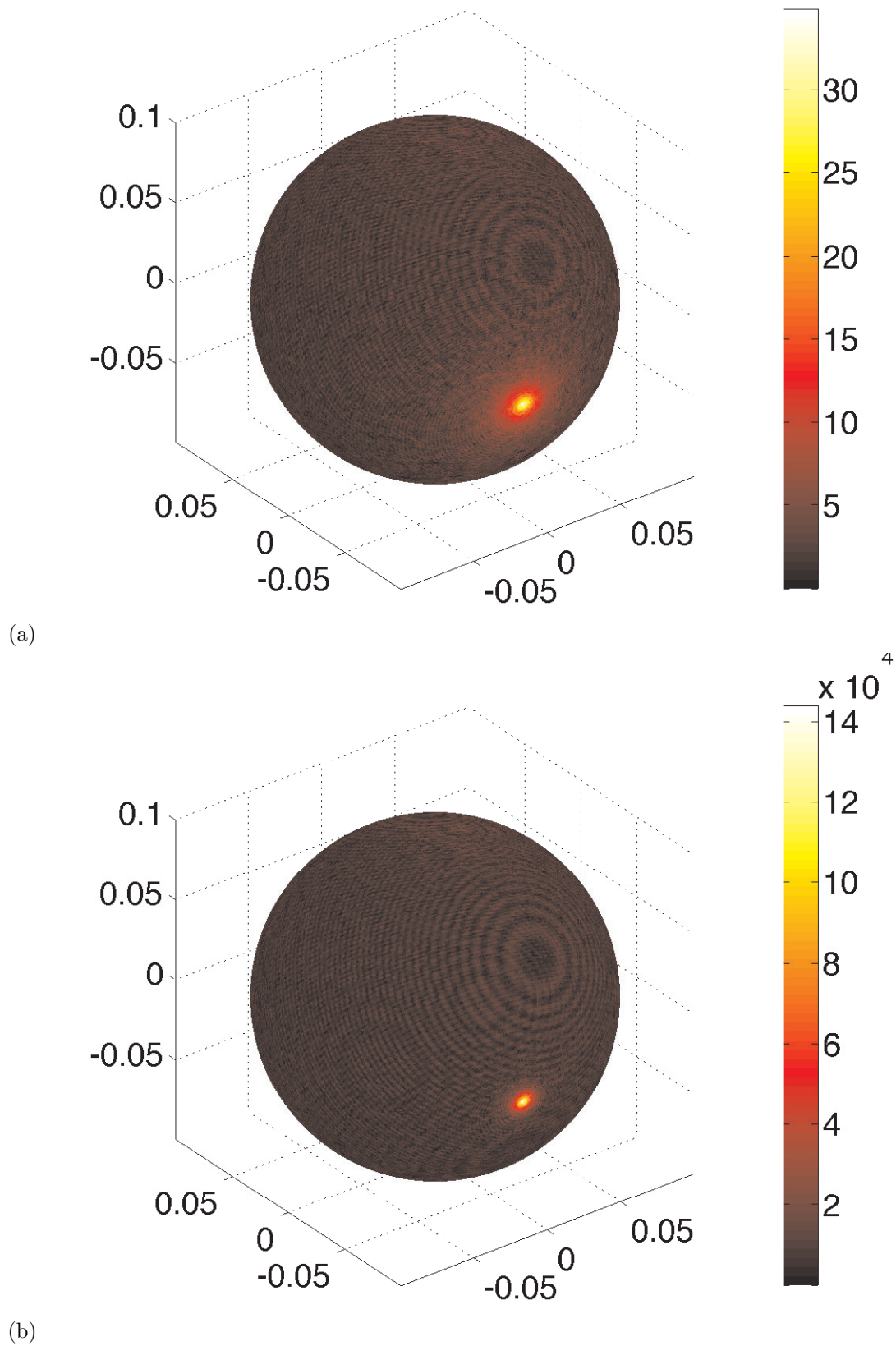


Figure 5.4: Visualization for the measurements of a radiating field in free-space for a spherical geometry of radius 10 cm and wavenumber $k = 4188 m^{-1}$ at 20dB. (a) Real part of the radiating wave. (b) Real part of the normal derivative of the radiating wave.

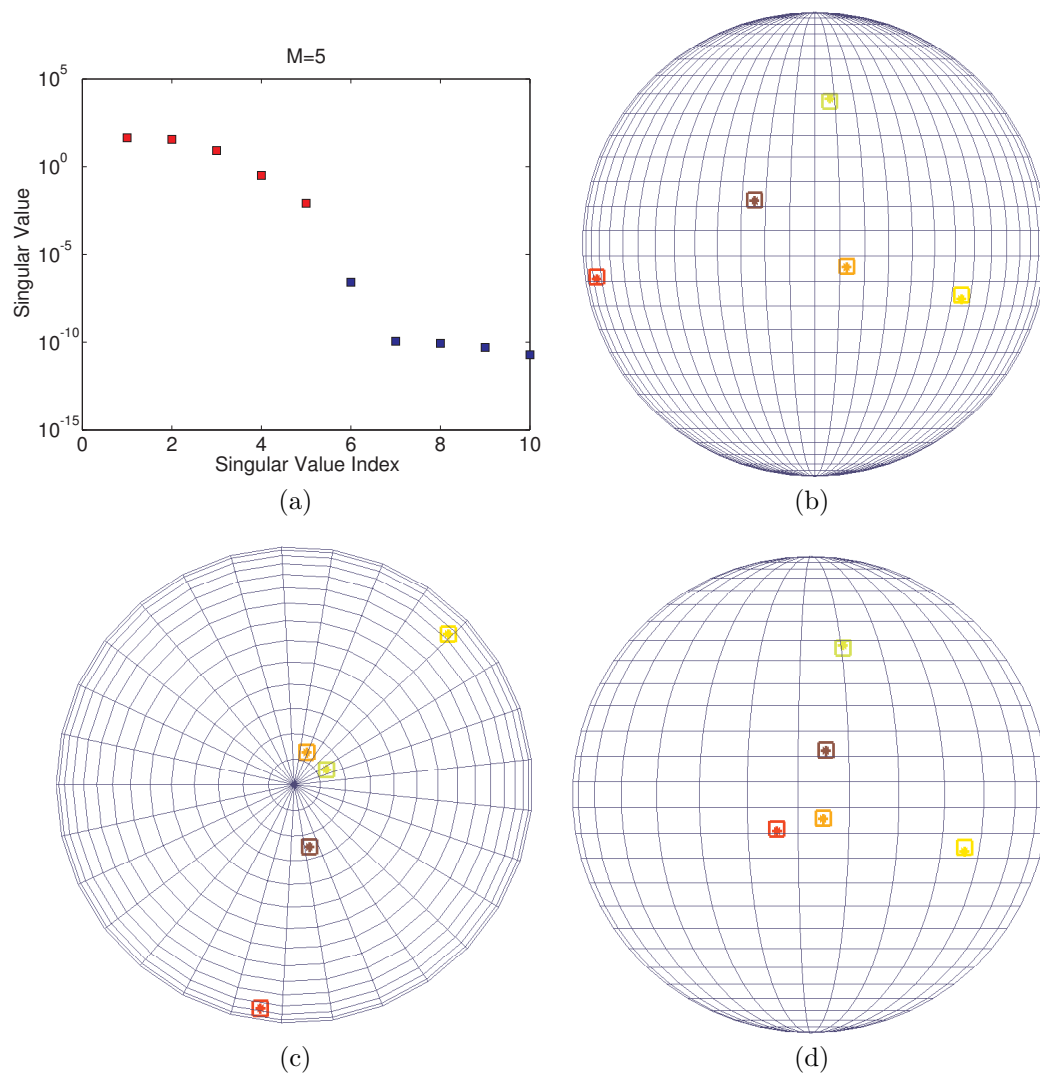


Figure 5.5: Point source model estimation: (a) Estimation of model order by separation of singular values. Different Planar views of the true (+) and the estimated (□) locations of the source in (b) YZ-plane view (c) XY-plane view (d) XZ-plane view where the colors are showing the estimated and true magnitude of the corresponding point source.

5.5 Outlook

Another possible extension of the FRI framework for the ISP can be achieved by considering a generalization of the point source model. In this case, assume that the source function can be represented

$$\dot{Q}(\mathbf{r}) = \sum_{m=0}^M s_m \phi(\mathbf{r} - \mathbf{r}_m) \text{ such that } \dot{Q}(\mathbf{r}) \subset \partial\Omega, \quad (5.52)$$

where $\phi(\mathbf{r})$ is a known compact support spatial distribution function and the only free parameters in the signal are the innovation locations \mathbf{r}_m and the innovation weights s_m . Hence, this is a generalization of the sparse point source model $Q(\mathbf{r})$ in (5.8) where (5.52) can be written equivalently as the convolution of $Q(\mathbf{r})$ with the known spatial function $\phi(\mathbf{r})$; i.e., $\dot{Q}(\mathbf{r}) = (Q * \Phi)(\mathbf{r})$. Furthermore, the counterpart governing equation will be given by

$$[\nabla^2 + k^2] \dot{U}(\mathbf{r}, \omega) = \dot{Q}(\mathbf{r}, \omega), \quad (5.53)$$

where $k^2 = \omega^2/c^2$ is the wavenumber with c being the speed of wave propagation in the medium. Finally, one needs to find the parameters of (5.52) given a set of measurements of the wave field in (5.53) on a surface $\partial\Omega$ enclosing (5.52). We further need to define families of sensing kernels $\dot{\Psi}$ that satisfy

$$[\nabla^2 + k^2] \dot{\Psi}(\mathbf{r}, \omega) = 0 \text{ in } \Omega \quad (5.54)$$

which will allow efficient reconstruction of the parameters of (5.52). Instead of extending the plausible sensing kernels and the corresponding reconstruction methods, we would like to use the framework that we already developed using the following proposition.

Proposition 10. *Choosing a sensing kernel $\dot{\Psi}$ such that $\{\phi^V * \dot{\Psi}\}(\mathbf{r}, \omega) = \Psi(\mathbf{r}, \omega)$ where $\phi^V(\mathbf{r}) = \phi(-\mathbf{r})$ is the reversed version of ϕ and $\Psi(\mathbf{r}, \omega)$ is the sensing kernels given by the Proposition 5, we reduce the problem (5.52) to an equivalent problem*

$$\langle \dot{\Psi}, \dot{Q} \rangle = \oint_{\partial\Omega} \left[\dot{\Psi}(\mathbf{r}, \omega) \frac{\partial}{\partial n} \dot{U}(\mathbf{r}, \omega) - \dot{U}(\mathbf{r}, \omega) \frac{\partial}{\partial n} \dot{\Psi}(\mathbf{r}, \omega) \right] dS, \quad (5.55)$$

$$= \langle \Psi, Q \rangle. \quad (5.56)$$

Proof. The first line is a direct consequence of the sensing principle in Proposition 4. For the second line, we refer to the dual extension principle defined on generalized functions [118] which states that given operators $U, U^* : \mathcal{S} \rightarrow \mathcal{S}$ that form an adjoint pair on $\mathcal{S} \times \mathcal{S}$, their action to $\mathcal{S}' \rightarrow \mathcal{S}'$ is extended by defining Uf and U^*f such that

$$\langle \varphi, Uf \rangle = \langle U^*\varphi, f \rangle, \text{ and } \langle \varphi, U^*f \rangle = \langle U\varphi, f \rangle,$$

which reveals

$$\begin{aligned} \langle \dot{\Psi}, \dot{Q} \rangle &= \langle \dot{\Psi}, \phi * Q \rangle \\ &= \langle \phi^V * \dot{\Psi}, Q \rangle \\ &= \langle \Psi, Q \rangle. \end{aligned} \quad (5.57)$$

□

The choice of the function $\phi(\mathbf{r})$ is in general application dependent. However, a particularly interesting case is to use radial basis functions in higher dimensions which are related to splines as well [119]. These functions are radially symmetric that only depends on the distance, i.e., $\phi(\|\mathbf{r}\|)$. Typical examples are the membrane spline and thin plate splines, which have been used in several other settings [120, 121].

5.6 Summary

We have proposed a novel FRI-like algorithmic framework for identifying parametric source models from boundary measurements of a radiating field. We proposed novel sensing functions that are derived from holomorphic functions and allow 2-D projections of the 3-D locations of the source function.

By design, the zeros of the holomorphic function that generates an N -th degree complex polynomial as the poles of the sensing function, we achieved a locally selective sensing function that is capable to spatially select the influence of the nearby point sources. This property is important in practice since the full view of the field data is usually not available in real applications. Therefore, this enables us to have a better approximation of the closed surface integral of the measurements that is the fundamental equation of the sensing principle but precise demonstration of this trade-off is lacking for now. We demonstrated the feasibility of the proposed algorithm by simulation results.

Chapter 6

Eigensensing Extension for Sparse Source Recovery

This chapter is based on the publication: Z. Doğan, T. Blu and D. Van De Ville, ‘*Eigensensing and Deconvolution for the Reconstruction of Heat Absorption Profiles from Photoacoustic Tomography Data*’, Proceedings of the Tenth IEEE International Symposium on Biomedical Imaging: From Nano to Macro (ISBI’13) pp. 1142-1145, 7-11 April 2013.

6.1 Introduction

In the previous chapter, we have introduced the concept of FRI for the inverse source problem (ISP) of radiating fields by means of defining a strong prior on the source distribution, i.e., a set of point sources. Moreover, we have seen that the introduced sensing principle plays a fundamental role that allows to map the field measurements to the FRI samples by a closed surface integral. Consequently, we elaborate the notion of FRI sampling kernels to FRI sensing kernels that allows to apply the FRI based nonlinear parameter estimation to the ISP of radiating fields from boundary measurements. However, although the point source assumption is general and applicable to many problems such as small absorbers in PAT [122, 108, 111], point scatterers in ultrasound tomography [123, 124] and epileptic foci in electroencephalography (EEG) [21, 22], some other applications require different modeling of the source distribution.

In this chapter, we focus on the sparse source recovery of radiating fields based on boundary measurements for a general source function instead of the point source distribution. Here, we propose a new theoretical framework, for which we coin the term *eigensensing*, to recover a continuous source function. One of the main features of our method is that there is no explicit forward model that needs to be used within a (usually) slow iterative scheme. Instead, the eigensensing principle allows us to computationally obtain several intermediate images that are blurred by known convolution kernels which are chosen as the eigenfunctions of the spatial Laplace operator. In particular, these intermediate images correspond to partial Fourier measurements of the source function. Hence, eigensensing principle establishes a link between FRI and methods that deal with partial Fourier recovery. The source function can be reconstructed by a joint deconvolution algorithm that uses the intermediate images as input. Moreover, we consider total variation regularization to make the inverse problem well-posed and to favor piecewise-smooth source distributions.

6.2 The problem statement

The radiating fields from a real valued spatiotemporal source function embedded in free space are described by the scalar wave equation

$$\left[\nabla^2 - \frac{1}{c^2} \frac{\partial^2}{\partial t^2} \right] u(\mathbf{r}, t) = q(\mathbf{r}, t), \quad (6.1)$$

where $q(\mathbf{r}, t)$ is the sparse source distribution that is assumed to be compactly supported by a measurement surface $\partial\Omega$, $u(\mathbf{r}, t)$ is the resulting causal radiating field and c is the speed of wave propagation in the medium. We further assume that the source function is square integrable, i.e., $\int_{-\infty}^{\infty} \int_{\partial\Omega} |q(\mathbf{r}, t)|^2 d^3r dt < \infty$. In this case, the solution for the field is given

$$u(\mathbf{r}, t) = \int_{-\infty}^{\infty} \int_{\partial\Omega} g_+(\mathbf{r} - \mathbf{r}', t - t') q(\mathbf{r}', t') d^3r' dt', \quad (6.2)$$

where $g_+(\mathbf{r}, t)$ is the retarded Green's function that satisfies

$$\left[\nabla^2 - \frac{1}{c^2} \frac{\partial^2}{\partial t^2} \right] g_+(\mathbf{r}, \mathbf{r}', t, t') = \delta(\mathbf{r} - \mathbf{r}') \delta(t - t'). \quad (6.3)$$

In the case of Sommerfield radiation boundary condition, the resulting causal Greens's function is given as

$$g_+(\mathbf{r}, \mathbf{r}', t, t') = -\frac{1}{4\pi} \frac{\delta\left(t' - \left(t - \frac{\|\mathbf{r} - \mathbf{r}'\|}{c}\right)\right)}{\|\mathbf{r} - \mathbf{r}'\|}, \quad (6.4)$$

that represents the radiating field due to an impulsive source located at $\{\mathbf{r}', t'\}$. Therefore, the forward model of the radiation is well defined by (6.2) and (6.4) for a known source function $q(\mathbf{r}, t)$. Instead, we consider the inverse source problem (ISP) to determine the unknown source function $q(\mathbf{r}, t)$ in (6.1) from measurements of the radiating field $u(\mathbf{r}, t)$. In general, the applications that require a solution to such an ISP can be categorized into two groups: First one is for imaging the interior of a volume source from observations of the radiating field in applications such as photoacoustic tomography (PAT) [122, 125], ultrasound tomography [123] and bioluminescence tomography (BLT) [126]. These applications are a variety of the so called hybrid methods that have been recently introduced and studied to overcome the individual deficiencies of conventional imaging methods and to combine the strengths of multiple imaging methods, hence termed as hybrid imaging methods. The second one is to design a volume of sources that acts as an antenna to radiate a prescribed field in wave field synthesis [127, 128]. In the first application, the field measurements are employed to reconstruct the source function whereas in the second application the field measurements are used to design a source distribution to replicate and transfer the field for example by an antenna. Mathematically, both ISP are identical with different emphasis of the application. However, the difference between these two cases ultimately reduces to consideration of the impact of non-radiating source function on the ISP. Hence, the ISP cannot have a unique solution due to the possible presence of non-radiating source functions [92]. Therefore, we consider the reconstruction of the source function that is physically meaningful; i.e., the one that generates a radiating field outside of its support.

Without loss of generality, we consider the time harmonic solutions of the scalar wave equation, and write the scalar Helmholtz equation

$$[\nabla^2 + k^2] U(\mathbf{r}, \omega) = Q(\mathbf{r}, \omega), \quad (6.5)$$

where $k^2 = \omega^2/c^2$ is the wavenumber and c is the speed of the wave propagation in free-space. We focus on the recovery of the source function $Q(\mathbf{r}, \omega)$ enclosed by a measurement surface from the knowledge of the field $U(\mathbf{r}, \omega)$ on $\partial\Omega$.

6.3 Eigensing principle

Definition 11 (Eigensing Function). *Let Ψ be an eigenfunction of the spatial Laplacian operator*

$$\nabla^2 \Psi(\mathbf{r}, \omega) + k^2 \Psi(\mathbf{r}, \omega) = 0, \quad (6.6)$$

*then we coin the term **eigensensor** for Ψ .*

Note that the sensing functions developed in Chapter 5 are solutions of the homogeneous Helmholtz equation restricted to the volume of interest. Therefore, the derived holomorphic sensing functions (5.31) do not satisfy 6.6 outside the volume Ω enclosing the source function. Instead, the eigensensors constitute a subset of valid sensing functions satisfying (5.9) by construction.

Proposition 12. *Assuming that the field and the normal derivative of the wave field are available on the boundary $\partial\Omega$, and one chooses Ψ satisfying (6.6), then one can “sense” the image of the source function through the surface integral:*

$$I_\Psi(\mathbf{r}) = (Q * \Psi)(\mathbf{r}) = \oint_{\partial\Omega} \left[U \frac{\partial}{\partial n} \Psi(\mathbf{r} - \mathbf{r}') - \Psi(\mathbf{r} - \mathbf{r}') \frac{\partial}{\partial n} U \right] dS, \quad (6.7)$$

where $$ is the 2-D or 3-D convolution operator, the partial derivatives $\frac{\partial}{\partial n}$ are directed outward (from the interior to exterior) and we call $I_\Psi(\mathbf{r})$ the **image of the source**.*

Proof. Using the Proposition 4, we can write

$$\langle \Psi, Q \rangle = \oint_{\partial\Omega} \left[\Psi(\mathbf{r}, \omega) \frac{\partial}{\partial n} U(\mathbf{r}, \omega) - U(\mathbf{r}, \omega) \frac{\partial}{\partial n} \Psi(\mathbf{r}, \omega) \right] dS. \quad (6.8)$$

Additionally, since the Laplace operator is shift-invariant, we can sense the source function at different spatial position and construct the image of the source function

$$I_\Psi(\mathbf{r}) = (Q * \Psi)(\mathbf{r}) \quad (6.9)$$

$$= \int_{\Omega} \Psi(\mathbf{r} - \mathbf{r}') Q(\mathbf{r}') d\mathbf{r}' \quad (6.10)$$

$$= \oint_{\partial\Omega} \left[U \frac{\partial}{\partial n} \Psi(\mathbf{r} - \mathbf{r}') - \Psi(\mathbf{r} - \mathbf{r}') \frac{\partial}{\partial n} U \right] dS, \quad (6.11)$$

where $*$ is the 2-D or 3-D convolution operator. We can thus compute the source image I_Ψ at any \mathbf{r} by the surface integral (6.7) using the boundary measurements, which represent the interaction of the source function with the eigensensor. In sum, the boundary measurements have been mapped to volumetric information without an explicit forward model as in conventional methods. \square

6.3.1 2D image reconstruction

To demonstrate the feasibility of the proposed method, we developed our method for an instructive 2-D setting. Let us first derive the separable eigenfunction of the 2-D Laplace operator in polar coordinates (r, ϕ) :

$$\left[\frac{1}{r} \frac{\partial}{\partial r} \left(r \frac{\partial}{\partial r} \right) + \frac{1}{r^2} \frac{\partial^2}{\partial \phi^2} \right] \Psi(r, \phi) = -k^2 \Psi(r, \phi). \quad (6.12)$$

Using the method of separation of variables and the non-singularity requirement at the origin, we get the eigenfunction of the Laplace operator in polar coordinates as the basis function for the polar Fourier transform on the whole space

$$\Psi_m^k(r, \phi) = \sqrt{\frac{k}{2\pi}} J_m(kr) e^{jm\phi}, \quad (6.13)$$

where J_m are the m^{th} -order Bessel functions ($m = 0, 1, \dots$). In Figure 6.1, we demonstrate the first four eigenfunctions in 2D polar coordinates. To better appreciate the meaning of the eigensensors, we provide the Fourier transform of Ψ_m

$$\mathcal{F}\{\Psi_m^k\}(k', \varphi'_k) = \delta(k - k') \frac{(-i)^m}{\sqrt{2\pi k}} e^{im\varphi'_k}, \quad (6.14)$$

where k' and φ'_k are the radial and angular parts of the polar Fourier space and which is nonzero only on a circle of radius k . Alternatively, this states that plane waves of the same wavenumber, as the basis function for the normal Fourier transform, can be superposed to get a so-called cylindrical wave [129, 130].

We can then formulate the image reconstruction problem as a joint deconvolution of multiple sensing functions degraded by known eigensensors by means of their known frequency domain localization. In particular, given the set of source images $I_{\Psi_m^{k_n}}$ computed from the measurements using eigensensors $\Psi_m^{k_n}$, $m = 1, \dots, M$ and at finitely chosen wavenumbers such that $0 < k_l \leq k_n \leq k_h$, $n = 1, \dots, N$ where k_l and k_h represent the lower and upper limits of k , we solve for

$$\hat{Q} = \arg \min_Q \sum_{n=1}^N \sum_{m=1}^M \left\| I_{\Psi_m^{k_n}} - Q * \Psi_m^{k_n} \right\|_2^2 + \mu J_{\text{reg}}(Q) \quad (6.15)$$

where the first term measures the data fidelity (under the ℓ^2 -norm) and the second term regularizes the source function, with the parameter $\mu \geq 0$ controlling the relative weights of the two terms. The regularization term is used to favor some solutions by penalizing the other by measuring the lack of smoothness and sparseness with differential operators.

We note that there exist a tremendous amount of research on the regularization of inverse problems and corresponding efficient minimization algorithms for the convex optimization problems [131, 132]. We choose the regularization term as the total variation (TV) semi-norm

$$J_{\text{TV}}(Q) = \int_{\mathbb{R}^2} \|\nabla Q(\mathbf{r})\|_2 d\mathbf{r}, \quad (6.16)$$

which favors sparseness in the gradient of A . The total variation (TV) regularization was introduced by Rudin et al. in 1992 [133] as a noise removal algorithm. Since then it has become more popular and the application of the same idea has been extended for many other inverse problems [134]. Recent advances in convex optimization theory have led to efficient algorithms for such minimization problem.

Minimization algorithm

The main difficulty in solving (6.15) is due to the non-differentiability of the regularization term. Standard approaches approximate the TV semi-norm with a smooth and differentiable one or to approximate it with a quadratic penalty technique. Here, we choose to use the alternating direction method of multipliers (ADMM) for which convergence has been proved [135]. For the sake of completeness, we briefly review the application of the ADMM method for the current problem.

Hereafter, we assume a discrete setting and replace (6.15) with the following problem noticing that eigensensors for the same order m are mutually disjoint in the frequency domain

$$\hat{a} = \arg \min_a \frac{1}{2} \sum_{m=1}^M \|\mathcal{F}I_{\Gamma_m} - \Gamma_m \mathcal{F}a\|_2^2 + \mu \sum_i \|D_i a\|_2 \quad (6.17)$$

where a is an $n \times n$ gray-scale image representing the source function, \mathcal{F} is a two-dimensional discrete Fourier transform matrix and $\Gamma_m = \sum_{n=1}^N \mathcal{F}\Psi_m^{k_n}$ is the Fourier transform of m^{th} -order

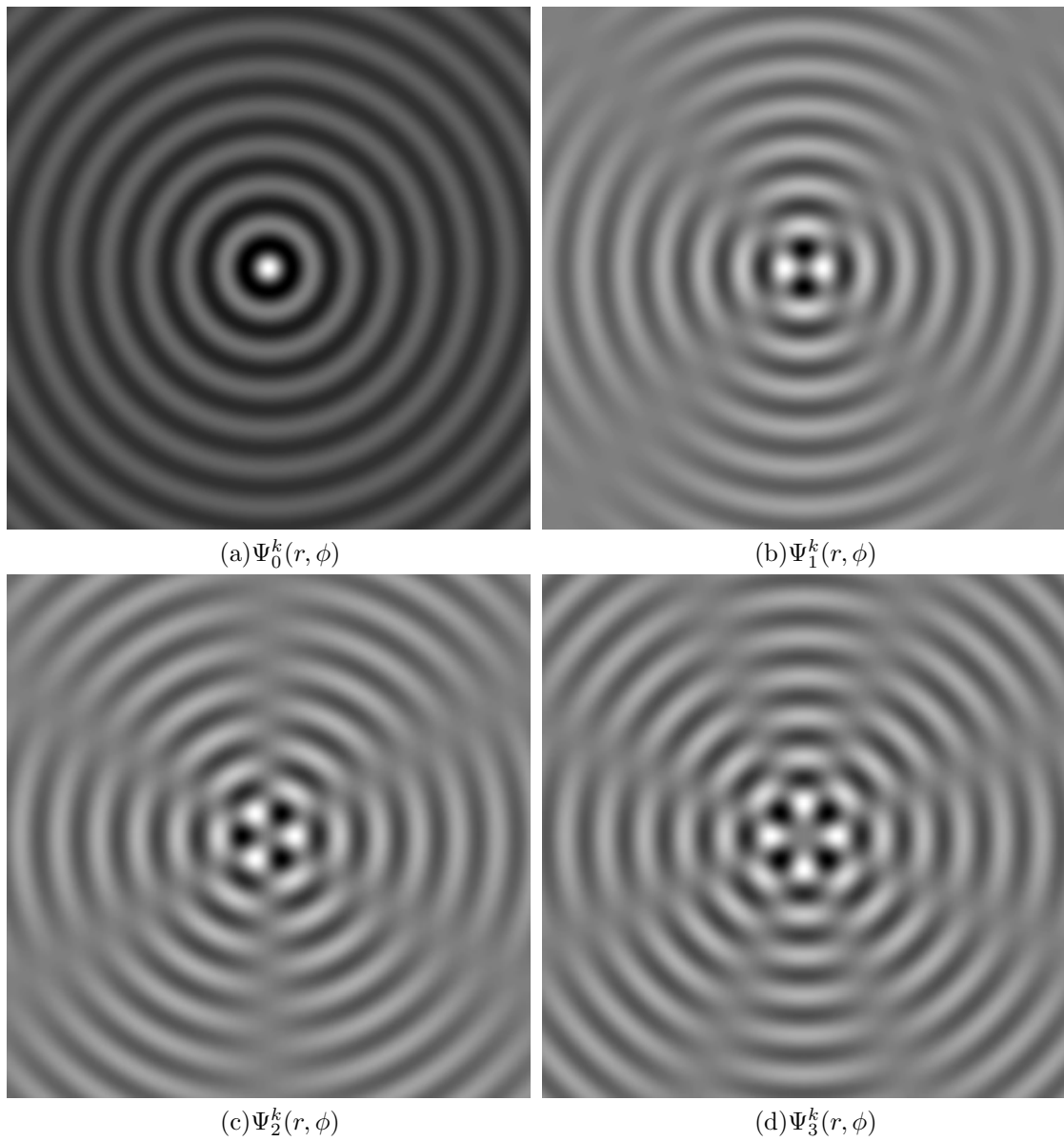


Figure 6.1: Visualization of the first four eigenfunctions of the Laplacian in polar coordinates with wavenumber $k = 4188\text{m}^{-1}$, which corresponds to 1 MHz in homogeneous medium with $c = 1500\text{m/s}$.

joint eigensensor; i.e., it represents a weighted selection matrix in k -space according to (6.14) and $I_{\Gamma_m} = \sum_{n=1}^N I_{\Psi_m^{k_n}}$ is the m^{th} -order observation of a . Next, $\sum_i \|D_i a\|_2$ is a discretization of the total variation (TV) of a with the common TV-L2 model where $D_i a = [(D^{(1)}a)_i; (D^{(2)}a)_i]$ denotes the discrete gradient of a at pixel i with $D^{(1)}$ and $D^{(2)}$ representing the two first order forward finite difference operators under periodic boundary conditions for a .

Algorithm 9 ADMM minimization algorithm

Require: $I_{\Gamma_m}; \Gamma_m; \mu > 0; p > 0$

- 1: **Initialization:** α^0, z^0
 - 2: **while** Not Converged **do**
 - 3: $a^{k+1} \leftarrow \underset{a}{\operatorname{argmin}} L_p(a, z^k, \alpha^k)$ by solving (6.19)
 - 4: $z^{k+1} \leftarrow \underset{z}{\operatorname{argmin}} L_p(a^{k+1}, z, \alpha^k)$ by solving (6.20)
 - 5: $\alpha^{k+1} \leftarrow \alpha^k + Da^{k+1} - z^{k+1}$
 - 6: **end while**
-

Next, we first introduce auxiliary variables $z_i = ((z_1)_i; (z_2)_i)$'s which are approximations of $D_i a$'s and then replace (6.17) with a constrained minimization problem

$$\min_{a, z_i} \frac{1}{2} \sum_{m=1}^M \|\mathcal{F}I_{\Gamma_m} - \Gamma_m \mathcal{F}a\|_2^2 + \mu \sum_i \|z_i\|_2 \quad \text{s.t. } z_i = D_i a, \forall i.$$

Relaxing the equality conditions and penalizing their violations by quadratic functions we get the scaled form [135] of the corresponding augmented Lagrangian

$$\begin{aligned} L_p(a, z, \alpha) = & \frac{1}{2} \sum_{m=1}^M \|\mathcal{F}I_{\Gamma_m} - \Gamma_m \mathcal{F}a\|_2^2 + \mu \sum_i \|z_i\|_2 \\ & + \frac{p}{2} \|Da - z + \alpha\|_2^2, \end{aligned} \quad (6.18)$$

where α is a scaled dual variable and p is the penalty parameter. Despite more decision parameters compared to (6.17), the problem (6.18) is easier to minimize with respect to z and a . First for a fixed z , the minimization of (6.18) for a becomes the least square problem

$$\min_a \frac{1}{2} \sum_{m=1}^M \|\mathcal{F}I_{\Gamma_m} - \Gamma_m \mathcal{F}a\|_2^2 + \frac{p}{2} \|Da - z + \alpha\|_2^2. \quad (6.19)$$

Second, for a fixed a , the second and third terms are separable with respect to z_i , so minimizing (6.18) for z is equivalent to solving

$$\min_{z_i} \left(\|z_i\|_2 + \frac{p}{2} \|D_i a - z_i + \alpha\|_2^2 \right), \quad \forall i, \quad (6.20)$$

for which the minimizer is given by the two dimensional shrinkage formula [136]. We provide a summary of the method in Algorithm 9.

6.4 PAT as a potential application

As a potential application, we again consider the reconstruction of heat absorption map in photoacoustic tomography (PAT). Specifically, the optical radiation absorbed by the tissue deposits

thermal energy. Due to the photoacoustic effect, the subsequent thermal expansion can be modeled as a heat source $H(\mathbf{r}, t)$ that gives rise to a pressure field $u(\mathbf{r}, t)$ governed by the wave equation in an acoustically homogeneous medium (under the condition of thermal confinement):

$$\nabla^2 u(\mathbf{r}, t) - \frac{1}{c^2} \frac{\partial^2 u(\mathbf{r}, t)}{\partial t^2} = -\frac{\beta}{C_p} \frac{\partial}{\partial t} H(\mathbf{r}, t), \quad (6.21)$$

where β is the isobaric volume expansion coefficient [K^{-1}], C_p is the specific heat [$\text{J}/(\text{K kg})$], and c is the speed of sound. Human breast is made of soft tissue with speed variations in the range of 10% and can thus be considered as an homogeneous medium [125]. The heating function can be further decomposed as the product

$$H(\mathbf{r}, t) = A(\mathbf{r})g_e(t),$$

where $A(\mathbf{r})$ is the spatial absorption function and $g_e(t)$ the temporal illumination function, which is known by the optical excitation protocol. The spatial absorption function is to be recovered from the boundary measurements of the pressure wave u . We further assume that the region-of-interest is Ω with boundary $\partial\Omega$. We can then write the time harmonic solutions of the PAT wave equation as

$$\nabla^2 U(\mathbf{r}, \omega) + \frac{\omega^2}{c^2} U(\mathbf{r}, \omega) = -(j\omega)A(\mathbf{r})G_e(\omega), \quad (6.22)$$

which is the inhomogeneous Helmholtz equation. The problem is to recover the spatial absorption function $A(\mathbf{r})$ from the Cauchy data $(U|_{\partial\Omega}, \nabla U \cdot \mathbf{e}_{\partial\Omega})$, which consists of the pressure field and its normal derivative along $\mathbf{e}_{\partial\Omega}$ being the unit outward normal to the boundary, respectively. Without loss of generality, we consider a specific frequency ω with corresponding wave-number $k = \omega/c$ and denote $\alpha = (j\omega)G_e(\omega)$. Hence, we can construct the image of the spatial absorption function

$$I_\Psi(\mathbf{r}) = \frac{1}{\alpha} (A * \alpha\Psi)(\mathbf{r}) = \frac{1}{\alpha} \oint_{\partial\Omega} \left[\Psi(\mathbf{r}, \omega) \frac{\partial}{\partial n} U(\mathbf{r}, \omega) - U(\mathbf{r}, \omega) \frac{\partial}{\partial n} \Psi(\mathbf{r}, \omega) \right] dS. \quad (6.23)$$

Finally, using the method developed in Section 6.3.1, we can reconstruct the spatial absorption function $A(\mathbf{r})$ from the measurements of the induced field. In Figure 6.2, we provide a flow-chart of the proposed algorithm.

6.4.1 Simulation results

We consider a typical PAT breast imaging system where the detection geometry is assumed to have a 8 cm radius and the generated pressure field is sampled with fast ultrasound transducers capable of linear and planar measurements of the wave field. The surface integral (6.23), which is the core of the eigensing framework, is assumed to be well-approximated thanks to the high sampling densities that are achieved in current devices [125]. For signals in the typical PAT range of 0.1–3 MHz, the wavenumber k will be between 500–12'500/m assuming constant speed of sound in soft tissue; i.e., $c = 1500\text{m/s}$ which imposes approximately 0.04mm spatial resolution of the sensing functions to be constructed [137, 138, 139].

We perform numerical experiments to evaluate the performance of our reconstruction algorithm on a numerical phantom of size 4096×4096 for the absorption map of a $16 \times 16\text{cm}^2$ breast tissue given in Fig. 6.3 (a). We choose only the zeroth order eigenfunction Ψ_0^k in (6.13) for different wavenumber, k from the specified PAT range. In our framework, each eigenfunction will perform a selection of partial Fourier measurements only on a circle of radius k in the k -space.

Due to incapability of most standard ultrasound transducers, detectors miss the low frequency components—frequencies less than 0.1 MHz—that are necessary for characterization of different

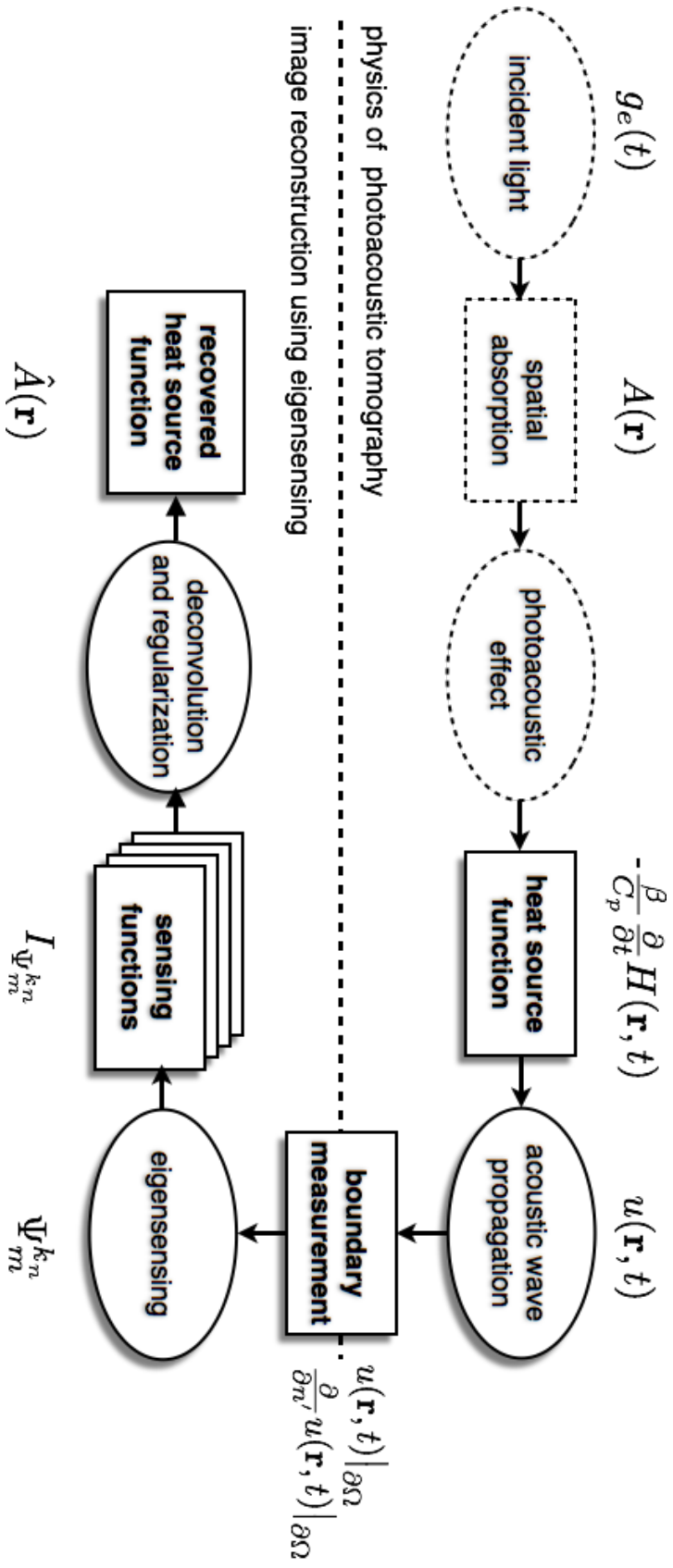


Figure 6.2: A schematic view of the proposed algorithm for PAT to reconstruct the spatial absorption function from the boundary measurements of the induced field.

tissues. Therefore, we propose to compare the reconstruction result and the original absorption map after a normalization process. We coin the term SNR improvement (iSNR)

$$\text{iSNR} = 10 \log_{10} \frac{\sum_i \|\hat{a} - \bar{a}\|^2}{\sum_i \|\hat{a}_0 - \bar{a}\|^2}, \quad (6.24)$$

where a , \hat{a} and \hat{a}_0 are the original image, the reconstructed image and the initial back-projected image, respectively, which are all normalized with respect to the mean and standard deviation of the data, i.e., $\bar{a} = (a - \eta)/\sigma$ where η is the mean and σ is the standard deviation of the data.

For the experiments, we use the breast phantom in Fig. 6.3 (a) and the image is scaled to $[0, 1]$ followed by a degradation with additive white gaussian noise at 20dB. We assume that the surface integral (6.23), is well-approximated and we solve for (6.17) for a suitably chosen regularization parameter (i.e., $\mu = 8$ with an oracle) using partial Fourier samples along a number of circles that correspond to chosen wavenumbers from the range of PAT. In Table 1, we demonstrate the results of the reconstruction quality with respect to number of evenly chosen frequencies on the Fourier domain. As it is expected, the quality of the reconstruction increases as the number of chosen wave numbers increases which allows more coverage of partial Fourier measurements. The results in Table 1 also indicate that the necessary number of wavenumbers to be used are limited for images composed of piecewise smooth absorption regions.

Table 6.1: Comparison of reconstruction quality in terms of iSNR with respect to number of wavenumber used (#k) evenly spaced on the k-space in the range of PAT.

#k	iSNR (dB)	#k	iSNR (dB)
5	3.19	30	6.26
10	4.74	35	6.27
15	5.79	40	6.28
20	5.88	45	6.29
25	6.21	50	6.30

In Fig. 6.3, we show the reconstruction result for a case where we evenly select 15 frequencies from the k-space. We observe the corresponding joint mask in the Fourier plane in Fig. 6.3 (b) and the corresponding inverse Fourier of the measured partial frequency data with 0 dB iSNR by (6.24). Finally, in Fig. 6.3 (d), we provide our solution with 5.79 dB iSNR with respect to normalized data as explained earlier. The result shows that reconstruction of fine spatial details while preserving sharp boundaries is achieved with the proposed method thanks to the TV regularization which is well-suited to the purpose of reconstruction of images composed of piecewise smooth regions.

6.5 Summary

We presented a novel theoretical framework called *eigensensing* principle and considered PAT as an example setting for the simulations to recover the heat absorption profile from the boundary measurements of induced wavefield. We proposed a family of sensing functions being eigenfunctions of the spatial Laplace operator to relate the boundary measurements of a wave field to the spatial source function. We also showed that the eigensensing principle allows for partial Fourier measurements of the source function which can be used in a joint deconvolution framework for the reconstruction.

The choice of the sensing functions as the eigenfunctions of the spatial Laplace operator in polar coordinates allowed better Fourier plane coverage rather than choosing a plane wave. Notice that the Bessel functions, which are the radial part of the eigensensors in 2D, decay like

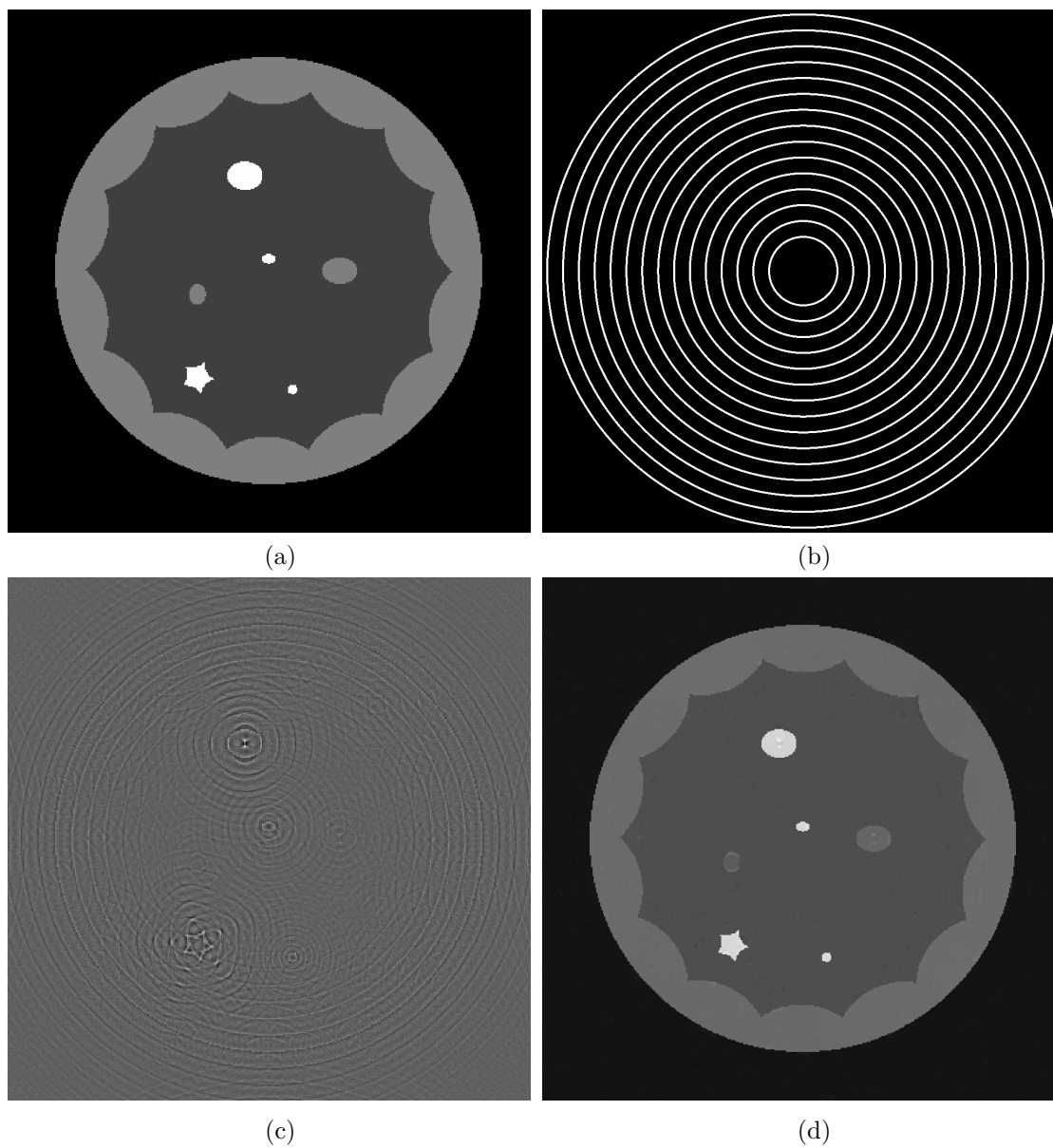


Figure 6.3: Reconstruction of heat absorption profile of a breast phantom; (a) Original phantom image (b) Partial frequency sampling along 15 evenly chosen wavenumbers from the range of PAT using eigensensing principle. (c) Inverse Fourier transform of the measured partial Fourier data with iSNR 0dB (d) Reconstruction with total variation (TV) regularization iSNR 5.79dB.

$1/\sqrt{r}$ which also yields better spatial localization than a plane wave. Hence, this also improves the approximation of the surface integration of the measurements with the sensing function.

We applied our method on a numerical phantom representing the heat absorption profile of a breast tissue for a 2-D proof-of-concept study. We opted for the total variation (TV) semi-norm as the regularization term that favors sparseness in the gradient of the absorption profile as an a priori. The preliminary results showed that the eigensing principle yields promising results on the detection of fine spatial details with varying absorption characteristics, which is potentially interesting for applications such as distinguishing malignant breast tissues from the normal ones.

Sparse image models for the reconstruction of the absorption profile the breast tissue in PAT from overdetermined boundary field measurements remains as a challenging research area of further research.

Chapter 7

Conclusion

In this thesis we have presented a new framework for the non-linear recovery of sparse signal representations. The remarkable aspect of these continuous-domain signal models is that they are characterized by finite rate parameters representing an innovation in time or in space. For the temporal case, this type of signals is used to model either a spontaneous change in the signal or to represent the (exact) timing of a pulse or a package of information in a communication channel. Regardless of the application, the localization of the instantaneous signal is utmost important to fully recover the signal content. Moreover, detecting an unexpected change is a critical feature for many applications based on time series analysis. For the spatial case, this type of signals are employed to model a sparse distribution of point sources that generate a radiating field. For example, the detection of the position of the emitter and the receiver is key to many applications in signal processing bearing an inherent localization problem from an observed field at a distance. Moreover, in many tomographical imaging systems, visualizing the internal volume from a set of boundary measurements is central to many applications where the abrupt changes in the volume of interest are used to elucidate any abnormality that might play a key role in early medical diagnosis. More specifically, we have developed non-linear recovery frameworks applicable to localization problems in time and in space. The main findings and results are summarized in the next section.

7.1 Summary of findings

- **Model fitting approach for improved recovery of noisy FRI signals**

We addressed the reconstruction of FRI signal parameters from severely degraded signal samples. We proposed a novel reconstruction method using a model-fitting approach that is based on minimizing the error between the computed and the recovered FRI samples subject to the annihilation system given by the Prony's method. We have seen that this approach outperforms the other state-of-the-art FRI reconstruction methods in terms of two aspects. First, we observed that FRI recovery with model-fitting approach reaches to the Cramer-Rao Lower Bounds at a lower SNR level with respect to the other methods well-known in the FRI domain. Second, we have seen that our approach could provide adequate reconstruction that best explains the available data even if the noise level does not allow for an accurate estimation with the other methods. Additionally, we proposed a new model order selection framework to determine the number of unknown parameters (i.e., the innovation rate) by analyzing the interpretation quality of data with respect to different model order. Thanks to this extension, the method becomes capable to operate in real applications.

- **FRI to study spontaneous brain activity in fMRI data**

We have further tailored the method of the FRI reconstruction with model-fitting approach for fMRI data analysis. More specifically, we considered the problem of spontaneous activity detection in fMRI timecourses using the HRF response as an FRI sampling kernel to adapt our work. We have validated our method using the fMRI data acquired during an event-related experiment with visual stimuli. The results showed decisively that the FRI framework can recover the activity signal in the visual cortex without requiring prior knowledge of the onsets and durations of the events. Hence, the model fitting approach with this new model order selection framework proved to be useful in detecting spontaneous activity in fMRI data. Moreover, the use of the FRI framework among non-visual related regions in the brain uncovered interesting activities unrelated to the stimulus, thereby, suggest further analysis of resting-state fMRI data for studying non-stationary dynamics.

- **FRI to recover sparse source distributions of radiating fields**

We developed the FRI framework for the inverse source problem of radiating fields. We have introduced the sensing principle (as an interpretation of Green’s theorem) that allows us to define several classes of sensing kernels invoking the link between the boundary measurements of the radiating field with the generalized samples of the sparse distribution, i.e., a set of point sources. In particular, we focused on specific sensing kernels that are derived from holomorphic functions and allow to retrieve projections of the source locations on a chosen plane. Finally, using several of these projections, we have shown that it is possible to recover the parameters of an FRI source distribution from its induced field measurements on an enclosing surface. Additionally, we demonstrated that this framework can be useful in a typical photoacoustic tomography as a potential application in which the goal is to localize small energy absorbing regions in the tissue.

- **Eigensensing principle to extract partial Fourier measurements**

We developed a new theoretical framework for the inverse source problem of radiating fields by means of generalizing the sensing principle. We proposed to use the spatial eigenfunctions of the Laplace operator as the new sensing kernels which allow to induce the link between the boundary measurements of the radiating field with partial Fourier measurements of the source function. With this generalization, we have shown that we can computationally obtain several images of the source function blurred by known sensing kernels. Finally, we proposed a joint deconvolution framework to reconstruct the source function from these intermediate images where each corresponds to partial Fourier measurements of the source function. Hence, the results confirmed that the source function can be reconstructed without an explicit forward model that needs to be used within a (usually) slow iterative scheme as in standard methods.

7.2 Outlook

The nonlinear recovery of sparse signal representations provides promising outlook that can potentially lead to new insights into different application of the FRI theory. Here, we discuss future considerations and some emerging directions concerning the techniques we developed in this thesis.

- **Resting State Dynamics in fMRI using FRI:**

Conventional analysis of functional magnetic resonance imaging (fMRI) data heavily relies on approaches where prior knowledge about the experimental paradigm is known. However, not all brain activity can be modeled using a priori known temporal regressors such as spontaneous activity, interictal epileptic discharges, hallucinations in schizophrenia. Moreover, the so-called resting-state is known to produce characteristic patterns of brain activity referred to as resting-state networks. Therefore, the exploration of brain activity using the

developed FRI framework is worth elaborating in the future. Furthermore, it is of particular interest to monitor different regions of the brain with respect to the activity rate using the new model order selection framework.

- **Variability of the HRF:**

The FRI framework models the fMRI timecourse for every voxel as a convolution between the innovation signal -a stream of Diracs- and the hemodynamic response function (HRF) as a predefined impulse response. There exist several techniques and models to estimate the HRF components. It is, however, well known that this approach is limited since high variability of the HRF within and across subjects has been well acknowledged. Therefore, a fundamental step in terms of fMRI analysis is to be able to account for the variability of the HRF. In the FRI framework for fMRI, it is possible to incorporate different HRF models per regions or voxels as long as they are defined a priori to map the fMRI timecourse samples to FRI samples. Alternatively, a substantial improvement would be to perform HRF identification from the fMRI data and to simultaneously use it to recover the activity signal.

- **Localized sensing functions:**

The sensing principle addresses the link between the boundary measurements of a radiating field and the inducing source function through a closed surface integral that has to be computed precisely. However, in practice we only have access to a finite number of measurements degraded by noise. We partially proposed a solution by designing specific sensing kernels that are extensions of 2D holomorphic functions where we can control the decay rate of the function with respect to chosen order of the holomorphic functions. Furthermore, the adapted Cadzow-like denoising scheme is used to relief any model mismatch and noise. However, designing compact support (or spatially most concentrated functions such as so-called Slepian functions [140, 141]) sensing kernels bears the supreme importance for adapting the framework for applications where we have access to only local measurements.

- **Sensing in heterogeneous media:**

We have used the scalar wave equation where we assumed that the medium of propagation is homogeneous with constant speed of sound c . Unfortunately, many applications cannot be modeled using only the homogeneous medium and adequate treatment is required for the inhomogeneous case. This problem is known as the speed map reconstruction in nonlinear ultrasound tomography. Specifically, the propagation of the wave is nonlinear in heterogeneous media, and the reconstruction of the speed map $c(\mathbf{r})$ is an active research topic in nonlinear tomography [142, 143]. However, we note that the sensing principle will hold as long as we adapt the sensing functions to the nonlinear propagation medium. Hence, we can show that the families of sensing functions satisfying

$$\left[\nabla^2 - \frac{\omega^2}{c(\mathbf{r})} \right] \Psi(\mathbf{r}, t) = 0, \text{ in } \Omega, \quad (7.1)$$

where $c(\mathbf{r})$ is the known (or estimated) speed map of the propagation medium, will accomplish to induce the link between the boundary measurements and the source function.

- **Sensing principle for different PDE's:**

In this manuscript we have considered mainly the Helmholtz equation as a reduced scalar wave equation that represents radiating fields. However, the developed FRI framework and the sensing principle can be extended to cope with the inverse source problem governed by the heat equation:

$$\left[\nabla^2 - \frac{1}{\alpha} \frac{\partial}{\partial t} \right] u(\mathbf{r}, t) = -p(\mathbf{r}, t), \text{ in } \Omega, \quad (7.2)$$

where α is the thermal diffusivity constant, $p(\mathbf{r}, t)$ is the compactly supported heat source to be determined from the measurements of the field, $u(\mathbf{r}, t)$ on $\partial\Omega$. This model is widely used to represent diffusion processes in many important physical or biological phenomena such as temperature variations, and photon transportation in tissues. In this case, we need to define the families of sensing functions that satisfy

$$\left[\nabla^2 - \frac{1}{\alpha} \frac{\partial}{\partial t} \right] \Psi(\mathbf{r}, t) = 0, \text{ in } \Omega. \quad (7.3)$$

Using the principle of the extension of 2-D harmonic functions into proper sensing functions for the wave field in Proposition 5, we propose that $\Psi(x, y, z, t) = e^{\pm\sqrt{\sigma}z + \alpha\sigma t} \varphi(x, y)$ is a valid sensing function that satisfies (7.3) where $\varphi(x, y)$ is a 2-D harmonic function, and σ is a proportionality constant. Finally, in order to use the developed framework for the localization of point heat sources, we propose that

$$\Psi(x, y, z, t) = \frac{e^{\pm\sqrt{\sigma}z + \alpha\sigma t}}{x + iy - a_n} \text{ where } a_n \notin \Omega \quad (7.4)$$

will be the necessary sensing function that is valid to use in our framework.

7.3 Concluding remarks

Finally, we would like to give some concluding remarks with respect to FRI framework and concepts of sparsity:

- **Sparsity in the new era of signal processing:**

The concept of sparsity is at the heart of all recent developments in signal processing research in continuous or discrete domain. The reason for this tremendous effort is likely because sparse signals are easy to process, compress, transmit, and denoise and they are also broad enough to model numerous classes of naturally-occurring signals and facilitate observation of various physical phenomena. Moreover, this is also well-aligned with the Occam's razor principle that states 'The simplest explanation for some phenomenon is more likely to be accurate than more complicated explanations', strengthening the power of sparse signal representations. Hence, it will probably stay at the heart of modern signal processing and keep reshaping the field in the future.

- **Rise of the non-linear signal reconstruction algorithms:**

Starting with the revolution around the concept of sparsity and search for sparse signal representations, the field is experiencing an increased empirical evidence that non-linear methods overpass the classical linear algorithms in terms of reconstruction quality and performance at the expense of the usage of more elaborate mathematical techniques. However, so far endowed attention on non-linear reconstruction algorithms has been demonstrated great success suggesting further progression in this direction.

- **Novel sparse representation of signals:**

New representations of signals have emerged during the past decades to better express the sparsity structure of the underlying signal form. Thanks to the considerable amount of research around this topic, we now have strong alternatives for the signal representations including novel transforms and dictionaries, such as wavelets [98, 14, 12, 144], curvelets [145, 146] and activelets [62, 63] to name a few. Another remarkable observation is that many classes of signals of practical interest actually live in a union of subspaces which could potentially pave the way for novel representation of sparse signals [147]. Furthermore, the families of sparse stochastic processes are introduced by means of extending the classical

innovation model as a solution of linear stochastic differential equations which flourishingly uncovers possible interpretations of sparsity beyond the assumptions of Gaussianity and stationarity of classical signal processing [118, 148, 149].

Appendix A

Appendices

A.1 Derivation of CRLB

The goal of the reconstruction problem given in (3.28) is to estimate the parameters $\Theta = [t_1, t_2, \dots, t_K, a_1, a_2, \dots, a_K]^T$ from a vector of M noisy samples $\tilde{s}_m = s_m + \tilde{e}_m$ where $\tilde{e}_m = \tilde{e}_{\mathcal{R}m} + i\tilde{e}_{\mathcal{I}m}$ is complex additive white Gaussian noise with variance σ^2 . The real and the imaginary parts of \tilde{e}_m are uncorrelated and each has a variance of $\sigma^2/2$, i.e., $\tilde{e}_{\mathcal{R}m}, \tilde{e}_{\mathcal{I}m} \sim \mathcal{N}(0, \sigma^2/2)$ so that the covariance matrix of the noise is $\mathbf{R} = \mathbb{E}\{\tilde{\mathbf{e}}\tilde{\mathbf{e}}^H\} = \sigma^2\mathbf{I}$. Now, assume that the *PDF* of $p(\tilde{\mathbf{s}}, \Theta)$ satisfies the regularity condition, i.e.,

$$\mathbb{E} \left[\frac{\partial \ln p(\tilde{\mathbf{s}}, \Theta)}{\partial \Theta} \right] = 0 \text{ for all } \Theta, \quad (\text{A.1})$$

then, the variance of any unbiased estimator $\hat{\Theta}$ satisfies $\mathbf{C}_{\hat{\Theta}} - \mathbf{I}_{\mathbf{F}}^{-1}(\Theta) \geq 0$, where $\mathbf{C}_{\hat{\Theta}}$ is the covariance matrix and $\mathbf{I}_{\mathbf{F}}(\Theta)$ is the Fisher information matrix given by

$$\mathbf{I}_{\mathbf{F}i,j}(\Theta) = -\mathbb{E} \left[\frac{\partial^2 \ln p(\tilde{\mathbf{s}}, \Theta)}{\partial \Theta_i \partial \Theta_j} \right]. \quad (\text{A.2})$$

Consider the *PDF* given by

$$p(\tilde{\mathbf{s}}, \Theta) = \frac{1}{(2\pi\sigma^2)^{M/2}} \exp \left(-\frac{1}{2\sigma^2} \sum_{m=1}^M (\tilde{s}_m - s_m(\Theta))^2 \right), \quad (\text{A.3})$$

in which case, the covariance matrix is lower bounded by

$$\mathbf{C}_{\hat{\Theta}} \geq \mathbf{I}_{\mathbf{F}}^{-1}(\Theta) \quad (\text{A.4})$$

where the Fisher information matrix is written explicitly by

$$\mathbf{I}_{\mathbf{F}} = \Phi_{\mathbf{S}}^H \mathbf{R}^{-1} \Phi_{\mathbf{S}} \quad (\text{A.5})$$

where

$$\Phi_{\mathbf{S}} = \begin{bmatrix} \frac{\partial s_1}{\partial \Theta_1} & \frac{\partial s_1}{\partial \Theta_2} & \cdots & \frac{\partial s_1}{\partial \Theta_{2K}} \\ \frac{\partial s_2}{\partial \Theta_1} & \frac{\partial s_2}{\partial \Theta_2} & \cdots & \frac{\partial s_2}{\partial \Theta_{2K}} \\ \vdots & \vdots & \dots & \vdots \\ \frac{\partial s_M}{\partial \Theta_1} & \frac{\partial s_M}{\partial \Theta_2} & \cdots & \frac{\partial s_M}{\partial \Theta_{2K}} \end{bmatrix}. \quad (\text{A.6})$$

Hence, the variance of the estimator is bounded by

$$\text{var}(\hat{\Theta}) \geq \text{diag}(\mathbf{I}_{\mathbf{F}}^{-1}). \quad (\text{A.7})$$

A.2 Training error of the estimator

The goal of the training error is to choose a reliable model order based on the degradation of the samples. In practical applications, the true model order is not available. Hence, one has to determine the degrees of freedom from the available data itself. However, as the degradation of the samples gets worse with increasing noise levels, the model order selection becomes more challenging.

We will further analyze the training error and the underlying model order selection framework developed in Sec. 3.2.3. For a given parameter set $\Theta = [t_1, t_2, \dots, t_K, a_1, a_2, \dots, a_K]^T$, we assume that available samples are degraded versions of the true samples

$$\tilde{s}_m = s_m + \tilde{e}_m$$

where $\tilde{e}_m = \tilde{e}_{\mathcal{R}m} + i\tilde{e}_{\mathcal{I}m}$ is complex additive white Gaussian noise with variance σ^2 . The real and the imaginary parts of \tilde{e}_m are uncorrelated and each has a variance of $\sigma^2/2$, i.e., $\tilde{e}_{\mathcal{R}m}, \tilde{e}_{\mathcal{I}m} \sim \mathcal{N}(0, \sigma^2/2)$ so that the covariance matrix of the noise is $\mathbf{R} = \mathbb{E}\{\tilde{\mathbf{e}}\tilde{\mathbf{e}}^H\} = \sigma^2\mathbf{I}$.

Let us assume $Q_{\hat{k}}(\tilde{s})$ is a nonlinear denoising method that includes a nonlinear estimation method; e.g., the data fitting framework in our case. Then, the computation of the estimated complex moment is given by

$$Q_{\hat{k}}(\tilde{s}) = \sum_{k=0}^{\hat{K}-1} \hat{a}_k e^{\alpha_m \frac{\tilde{s}}{\hat{t}_k}}. \quad (\text{A.8})$$

where $\{\hat{t}_k, \hat{a}_k\}_{k=1 \dots \hat{k}}$ are the estimated parameters for a model order \hat{K} . Finally, the training error curve is defined as

$$E_T(\hat{k}) = \|Q_{\hat{k}}(\tilde{s}) - \tilde{s}\|_2^2, \quad (\text{A.9})$$

where $\hat{k} = [1, \dots, \frac{M}{2}]$ and M is the number of samples of \tilde{s} . We can then write

$$\begin{aligned} \mathbb{E}[E_T(\hat{k})] &= \mathbb{E}[\|Q_{\hat{k}}(\tilde{s}) - \tilde{s}\|_2^2] \\ &= \mathbb{E}[\|Q_{\hat{k}}(\tilde{s}) - s + s - \tilde{s}\|_2^2] \\ &= \mathbb{E}[\|Q_{\hat{k}}(\tilde{s}) - s\|_2^2] + \mathbb{E}[\|s - \tilde{s}\|_2^2] + 2\mathbb{E}[\|(Q_{\hat{k}}(\tilde{s}) - s)^H(s - \tilde{s})\|_2^2] \\ &= \mathbb{E}[\|Q_{\hat{k}}(\tilde{s}) - s\|_2^2] + \mathbb{E}[\|s - \tilde{s}\|_2^2] - 2\mathbb{E}[\|w^H(Q_{\hat{k}}(\tilde{s}))\|_2^2] \end{aligned} \quad (\text{A.10})$$

where the three terms in the last line are known as the true MSE of the estimator, the noise power, i.e., $M\sigma^2$, and the divergence of the estimator for additive gaussian noise case. Although this is well-known from Stein's unbiased risk estimate for real valued functions [150, 151], we develop the case for the complex valued functions for the sake of completeness.

The complex Gaussian random is given in (3.28) with $w_{\mathcal{R}m}, w_{\mathcal{I}m} \sim \mathcal{N}(0, \sigma^2/2)$ with the PDF is given by

$$p(\tilde{\mathbf{e}}) = \frac{1}{(\pi\sigma^2)^{M/2}} \exp\left(-\frac{1}{\sigma^2} \sum_{m=1}^M (\tilde{e}_m)^2\right). \quad (\text{A.11})$$

We work on the following expectation $\mathbb{E}[\|\tilde{e}^H(Q_{\hat{k}}(\tilde{s}))\|_2^2] = \mathbb{E}[\|\tilde{e}_I^H(Q_{\hat{k}}(\tilde{s}))\|_2^2] - i\mathbb{E}[\|\tilde{e}_Q^H(Q_{\hat{k}}(\tilde{s}))\|_2^2]$ real and the imaginary parts separately. We first assume the mapping $Q_{\hat{k}}$:

$\mathbb{C}^M \rightarrow \mathbb{C}^M$ be weakly differentiable. Then,

$$\mathbb{E}[\|\tilde{e}_I^H(Q_{\hat{k}}(\tilde{s}))\|_2^2] \quad (\text{A.12})$$

$$= \int p(\tilde{\mathbf{e}}_I) \sum_{m=1}^M \tilde{e}_{I_m} Q_{\hat{k}}(s + \tilde{\mathbf{e}}_I + i\tilde{\mathbf{e}}_Q) d^M \tilde{\mathbf{e}}_I \quad (\text{A.13})$$

$$= \sum_{m=1}^M \int p(\tilde{\mathbf{e}}_I) \tilde{e}_i Q_{\hat{k}}(s + \tilde{\mathbf{e}}_I + i\tilde{\mathbf{e}}_Q) d^M \tilde{\mathbf{e}}_I \quad (\text{A.14})$$

$$= \sum_{m=1}^M \int \frac{-\sigma^2}{2} \frac{\partial}{\partial \tilde{e}_{I_m}} p(\tilde{\mathbf{e}}_I) Q_{\hat{k}}(s + \tilde{\mathbf{e}}_I + i\tilde{\mathbf{e}}_Q) d^M \tilde{\mathbf{e}}_I \quad (\text{A.15})$$

$$= \mathbb{E}\left[\frac{\sigma^2}{2} \text{div}_{\tilde{e}_I} Q_{\hat{k}}(\tilde{s})\right], \quad (\text{A.16})$$

where $\text{div}_{\tilde{e}} = \sum_{m=1}^M \frac{\partial}{\partial \tilde{e}_m}$ is the divergence with respect to the real and the imaginary parts. Hence, the second term is written similarly

$$\mathbb{E}[\|\tilde{e}_Q^H(Q_{\hat{k}}(\tilde{s}))\|_2^2] = \mathbb{E}\left[\frac{\sigma^2}{2} \text{div}_{\tilde{e}_Q} Q_{\hat{k}}(\tilde{s})\right] \quad (\text{A.17})$$

which finally yields

$$\mathbb{E}[\|\tilde{e}^H(Q_{\hat{k}}(\tilde{s}))\|_2^2] = \frac{\sigma^2}{2} \mathbb{E}[(\text{div}_{\tilde{e}_I} - i\text{div}_{\tilde{e}_Q}) Q_{\hat{k}}(\tilde{s})]. \quad (\text{A.18})$$

We note that this can be useful since one can define an unbiased MSE estimator using the training error, the noise variance σ^2 and the divergence of the estimator without knowing the true value of the signal [150, 151]. However, although an approximation of the divergence can be done using a Monte-Carlo SURE approach, computing the divergence of a nonlinear estimator is always a challenging problem itself. Hence, we leave this discussion at this point and focus only on the training error curve.

The model selection requires to choose the number of degrees of freedom in our estimation problem. We rather proposed a model selection framework in Sec. 3.2.3 following our observation that the training curve exhibits a U-curve pattern. This can be easily seen from the first two terms of the analysis in (A.12) while ignoring the last term. Obviously, the second term does not change with respect to our mapping $Q_{\hat{k}}$. Hence, the first term, i.e., the MSE of the estimator, will dominate the training error for the under and the over fitting values of model order \hat{k} as there will be a contribution coming from the bias of the estimator. However, for the true model order, the estimator MSE will be the variance for an unbiased estimator. Therefore, once the training error hits the fitting region defined by a plato behavior, we choose the minimum of model order in this plato to favor a parsimonious model.

Bibliography

- [1] D.L. Donoho, “Compressed sensing,” *IEEE Transactions on Information Theory*, vol. 52, no. 4, pp. 1289–1306, April 2006.
- [2] E.J. Candes and M.B. Wakin, “An introduction to compressive sampling,” *IEEE Signal Processing Magazine*, vol. 25, no. 2, pp. 21–30, March 2008.
- [3] S.J. Wright, R.D. Nowak, and M.A.T. Figueiredo, “Sparse reconstruction by separable approximation,” *IEEE Transactions on Signal Processing*, vol. 57, no. 7, pp. 2479–2493, July 2009.
- [4] M. Vetterli, P. Marziliano, and T. Blu, “Sampling signals with finite rate of innovation,” *IEEE Transactions on Signal Processing*, vol. 50, no. 6, pp. 1417–1428, 2002, IEEE Signal Processing Society’s 2006.
- [5] P.L. Dragotti, M. Vetterli, and T. Blu, “Sampling moments and reconstructing signals of finite rate of innovation: Shannon meets Strang-Fix,” *IEEE Transactions on Signal Processing*, vol. 55, no. 5, pp. 1741–1757, may 2007.
- [6] T. Blu, P.-L. Dragotti, M. Vetterli, P. Marziliano, and L. Coulot, “Sparse sampling of signal innovations,” *IEEE Signal Processing Magazine*, vol. 25, no. 2, pp. 31–40, 2008.
- [7] C.E. Shannon, “Communication in the presence of noise,” *Proceedings of the IRE*, vol. 37, no. 1, pp. 10–21, Jan 1949.
- [8] M. Unser, “Sampling-50 years after Shannon,” *Proceedings of the IEEE*, vol. 88, no. 4, pp. 569–587, apr 2000.
- [9] T. Blu and M. Unser, “Approximation error for quasi-interpolators and (multi-)wavelet expansions,” *Applied and Computational Harmonic Analysis*, vol. 6, no. 2, pp. 219 – 251, 1999.
- [10] M. Unser, A. Aldroubi, and M. Eden, “Polynomial spline signal approximations: filter design and asymptotic equivalence with Shannon’s sampling theorem,” *IEEE Transactions on Information Theory*, vol. 38, no. 1, pp. 95–103, Jan 1992.
- [11] S. Mallat, *A Wavelet Tour of Signal Processing, Third Edition: The Sparse Way*, Academic Press, 3rd edition, 2008.
- [12] M. Vetterli and J. Kovačević, *Wavelets and Subband Coding*, Prentice-Hall, Inc., Upper Saddle River, NJ, USA, 1995.
- [13] M. Unser, “Splines: a perfect fit for signal and image processing,” *IEEE Signal Processing Magazine*, vol. 16, no. 6, pp. 22–38, Nov 1999.
- [14] M. Unser and T. Blu, “Wavelet theory demystified,” *IEEE Transactions on Signal Processing*, vol. 51, no. 2, pp. 470–483, Feb 2003.

-
- [15] Y. M. Lu and M. N. Do, “A Theory for Sampling Signals From a Union of Subspaces,” *IEEE Transactions on Signal Processing*, vol. 56, no. 6, pp. 2334–2345, June 2008.
- [16] R. Tur, Y.C. Eldar, and Z. Friedman, “Innovation rate sampling of pulse streams with application to ultrasound imaging,” *IEEE Transactions on Signal Processing*, vol. 59, no. 4, pp. 1827–1842, April 2011.
- [17] J. Oñativia, S.R. Schultz, and P.-L Dragotti, “A finite rate of innovation algorithm for fast and accurate spike detection from two-photon calcium imaging,” *Journal of Neural Engineering*, vol. 10, no. 4, pp. 046017, 2013.
- [18] A. Erdozain and P.M. Crespo, “Reconstruction of aperiodic FRI signals and estimation of the rate of innovation based on the state space method,” *Signal Processing*, vol. 91, no. 8, pp. 1709 – 1718, 2011.
- [19] P. Shukla and P.-L Dragotti, “Sampling schemes for multidimensional signals with finite rate of innovation,” *IEEE Transactions on Signal Processing*, vol. 55, pp. 3670–3686, 2007.
- [20] H. Pan, T. Blu, and P.-L Dragotti, “Sampling curves with finite rate of innovation,” *IEEE Transactions on Signal Processing*, vol. 62, no. 2, pp. 458–471, January 2014.
- [21] D. Kandaswamy, T. Blu, and D. Van De Ville, “Analytic sensing: Noniterative retrieval of point sources from boundary measurements,” *SIAM Journal on Scientific Computing*, vol. 31, no. 4, pp. 3179–3194, July 2009.
- [22] D. Kandaswamy, *Sparse Source Recovery from Boundary Measurements using an Extension of Prony’s Method for the Poisson Equation*, Ph.D. thesis, STI, Lausanne, 2011.
- [23] Z Doğan, T. Blu, and D. Van De Ville, “Finite-rate-of-innovation for the inverse source problem of radiating fields,” *Sampling Theory in Signal and Image Processing*, vol. 13, no. 3, pp. 271–294, 2014.
- [24] J.A. Urigen, T. Blu, and P.L. Dragotti, “FRI sampling with arbitrary kernels,” *IEEE Transactions on Signal Processing*, vol. 61, no. 21, pp. 5310–5323, 2013.
- [25] G. Strang and G. Fix, “A Fourier analysis of the finite element variational method,” C.I.M.E., II Ciclo Erice 1971, constr. Aspects functional Analysis, 793-840 (1973)., 1973.
- [26] M. Unser and T. Blu, “Cardinal exponential splines: Part I-theory and filtering algorithms,” *IEEE Transactions on Signal Processing*, vol. 53, pp. 1425–1438, 2005.
- [27] T. Blu and M. Unser, “Quantitative Fourier analysis of approximation techniques: Part ii - wavelets,” *IEEE Transactions on Signal Processing*, vol. 47, pp. 2783–2795, 1999.
- [28] P. Stoica and R.L. Moses, *Introduction to spectral analysis*, Prentice Hall, 1997.
- [29] S.M. Kay, *Modern Spectral Estimation: Theory and Application*, Prentice-Hall signal processing series. Prentice Hall, 1999.
- [30] D.H. Johnson and D.E. Dudgeon, *Array Signal Processing: Concepts and Techniques*, Prentice-Hall signal processing series. P T R Prentice Hall, 1993.
- [31] J. Benesty, J. Chen, and Y. Huang, *Microphone Array Signal Processing*, Springer Topics in Signal Processing. Springer, 2008.
- [32] M. Elad, P. Milanfar, and G.H. Golub, “Shape from moments - an estimation theory perspective,” *IEEE Transactions on Signal Processing*, vol. 52, no. 7, pp. 1814–1829, July 2004.

- [33] P. Milanfar, George C. Verghese, W. Clem Karl, and A.S. Willsky, "Reconstructing polygons from moments with connections to array processing," *IEEE Transactions on Signal Processing*, vol. 43, no. 2, pp. 432–443, Feb 1995.
- [34] Par R. Prony, "Essai expérimental et analytique sur les lois de la dilatabilité des fluides élastiques, et sur celles de la force expansive de la vapeur de leau et de la vapeur de l'alkool, á différentes températures," *Journal de l'Ecole Polytechnique*, vol. 1, pp. 24–76, 1795.
- [35] B. De Moor, "The singular value decomposition and long and short spaces of noisy matrices," *IEEE Transactions on Signal Processing*, vol. 41, no. 9, pp. 2826–2838, Sep 1993.
- [36] G. Strang, *Introduction to Linear Algebra*, Wellesley-Cambridge Press, 2003.
- [37] Bart De Moor, "Structured total least squares and $\{L_2\}$ approximation problems," *Linear Algebra and its Applications*, vol. 188189, no. 0, pp. 163 – 205, 1993.
- [38] P. Lemmerling, L. Vanhamme, S. Van Huffel, and B. De Moor, "Iqml-like algorithms for solving structured total least squares problems: a unified view," *Signal Processing*, vol. 81, no. 9, pp. 1935 – 1945, 2001.
- [39] J. A. Cadzow, "Signal enhancement: A composite property mapping algorithm," *IEEE Trans. on Acoust., Speech, Signal Processing*, vol. 36, pp. 39–62, 1988.
- [40] Y. Hua and T.K. Sarkar, "Matrix pencil method for estimating parameters of exponentially damped/undamped sinusoids in noise," *IEEE Transactions on Acoustics, Speech and Signal Processing*, vol. 38, no. 5, pp. 814–824, May 1990.
- [41] T.K. Sarkar and O. Pereira, "Using the matrix pencil method to estimate the parameters of a sum of complex exponentials," *IEEE Antennas and Propagation Magazine*, vol. 37, no. 1, pp. 48–55, Feb 1995.
- [42] B.D. Rao and K.S. Arun, "Model based processing of signals: a state space approach," *Proceedings of the IEEE*, vol. 80, no. 2, pp. 283–309, Feb 1992.
- [43] Y. Hua and T.K. Sarkar, "On svd for estimating generalized eigenvalues of singular matrix pencil in noise," *IEEE Transactions on Signal Processing*, vol. 39, no. 4, pp. 892–900, April 1991.
- [44] I. Maravic and M. Vetterli, "Sampling and reconstruction of signals with finite rate of innovation in the presence of noise," *IEEE Transactions on Signal Processing*, vol. 53, no. 8, pp. 2788–2805, Aug 2005.
- [45] D.W. Tufts and R. Kumaresan, "Estimation of frequencies of multiple sinusoids: Making linear prediction perform like maximum likelihood," *Proceedings of the IEEE*, vol. 70, no. 9, pp. 975–989, Sept 1982.
- [46] B. Porat and Benjamin Friedlander, "On the accuracy of the kumaresan-tufts method for estimating complex damped exponentials," *IEEE Transactions on Acoustics, Speech and Signal Processing*, vol. 35, no. 2, pp. 231–235, Feb 1987.
- [47] K. Gedalyahu, R. Tur, and Y.C. Eldar, "Multichannel sampling of pulse streams at the rate of innovation," *IEEE Transactions on Signal Processing*, vol. 59, no. 4, pp. 1491–1504, April 2011.
- [48] V.Y.F. Tan and V.K. Goyal, "Estimating signals with finite rate of innovation from noisy samples: A stochastic algorithm," *IEEE Transactions on Signal Processing*, vol. 56, no. 10, pp. 5135–5146, Oct 2008.

- [49] A. Hirabayashi, “Sampling and recovery of continuously-defined sparse signals and its applications,” in *Subspace Methods for Pattern Recognition in Intelligent Environment*, Yen-Wei Chen and Lakhmi C. Jain, Eds., vol. 552 of *Studies in Computational Intelligence*, pp. 151–170. Springer Berlin Heidelberg, 2014.
- [50] C. Gilliam and T. Blu, “Fitting instead of annihilation: Improved recovery of noisy FRI signals,” in *Acoustics, Speech and Signal Processing (ICASSP), 2014 IEEE International Conference on*, May 2014, pp. 51–55.
- [51] A.C. Davison, *Statistical Models*, Cambridge Series in Statistical and Probabilistic Mathematics. Cambridge University Press, 2003.
- [52] B. De Moor, “Total least squares for affinely structured matrices and the noisy realization problem,” *IEEE Transactions on Signal Processing*, vol. 42, no. 11, pp. 3104–3113, Nov 1994.
- [53] Y. Bresler and A. Macovski, “Exact maximum likelihood parameter estimation of superimposed exponential signals in noise,” *IEEE Transactions on Acoustics, Speech and Signal Processing*, vol. 34, no. 5, pp. 1081–1089, Oct 1986.
- [54] V. Nagesha and S. Kay, “On frequency estimation with the iqml algorithm,” *IEEE Transactions on Signal Processing*, vol. 42, no. 9, pp. 2509–2513, Sept. 1994.
- [55] M.P. Clark and L.L. Scharf, “On the complexity of iqml algorithms,” *IEEE Transactions on Signal Processing*, vol. 40, no. 7, pp. 1811–1813, July 1992.
- [56] Z Doğan, T. Blu, and D. Van De Ville, “Detecting spontaneous brain activity in functional magnetic resonance imaging using finite rate of innovation,” in *Biomedical Imaging (ISBI), 2014 IEEE 11th International Symposium on*, April 2014, pp. 1047–1050.
- [57] K.J. Worsley and K.J. Friston, “Analysis of fMRI time-series revisited - again,” *NeuroImage*, vol. 2, pp. 173–181, 1995.
- [58] Hong Yuan, Hong Li, Zhijie Zhang, and Jiang Qiu, “A general fmri linear convolution model based dynamic characteristic,” in *ICNC (1)*, Lipo Wang, Ke Chen 0001, and Yew-Soon Ong, Eds. 2005, vol. 3610 of *Lecture Notes in Computer Science*, pp. 952–955, Springer.
- [59] K.J. Friston, J. Ashburner, S.J. Kiebel, T.E. Nichols, and W.D. Penny, Eds., *Statistical Parametric Mapping: The Analysis of Functional Brain Images*, Academic Press, 2007.
- [60] Bharat B. Biswal, “Resting state fmri: A personal history,” *NeuroImage*, vol. 62, no. 2, pp. 938 – 944, 2012.
- [61] C.C. Gaudes, N. Petridou, S. T. Francis, I. L. Dryden, and P. A. Gowland, “Paradigm free mapping with sparse regression automatically detects single-trial functional magnetic resonance imaging blood oxygenation level dependent responses,” *Human Brain Mapping*, vol. 34, no. 3, pp. 501–518, 2013.
- [62] I. Khalidov, J. Fadili, F. Lazeyras, D. Van De Ville, and M. Unser, “Activelets: Wavelets for sparse representation of hemodynamic responses,” *Signal Processing*, vol. 91, no. 12, pp. 2810 – 2821, 2011.
- [63] F.I. Karahanoglu, C.C. Gaudes, F. Lazeyras, and D. Van De Ville, “Total activation: fmri deconvolution through spatio-temporal regularization,” *NeuroImage*, vol. 73, no. 0, pp. 121 – 134, 2013.

- [64] C.F. Beckmann and S.M. Smith, "Probabilistic independent component analysis for functional magnetic resonance imaging," *IEEE Transactions on Medical Imaging*, vol. 23, no. 2, pp. 137–152, Feb 2004.
- [65] V.D. Calhoun and T. Adali, "Unmixing fmri with independent component analysis," *IEEE Engineering in Medicine and Biology Magazine*, vol. 25, no. 2, pp. 79–90, March 2006.
- [66] S.A. Huettel, A.W. Song, and G. McCarthy, *Functional Magnetic Resonance Imaging*, Freeman, 2009.
- [67] R. B. Buxton, *Introduction to Functional Magnetic Resonance Imaging*, Cambridge University Press, second edition, 2009, Cambridge Books Online.
- [68] M.H. Levitt, *Spin Dynamics: Basics of Nuclear Magnetic Resonance*, Wiley, 2001.
- [69] R.R. Ernst, G. Bodenhausen, and A. Wokaun, *Principles of Nuclear Magnetic Resonance in One and Two Dimensions*, International series of monographs on chemistry. Clarendon Press, 1990.
- [70] E.M. Haacke, R.W. Brown, M.R. Thompson, and R. Venkatesan, *Magnetic Resonance Imaging: Physical Principles and Sequence Design*, Wiley, 1999.
- [71] M.A. Bernstein, K.F. King, and X.J. Zhou, *Handbook of MRI Pulse Sequences*, Elsevier Science, 2004.
- [72] D. J Heeger and D Ress, "What does fMRI tell us about neuronal activity?," *Nature Reviews Neuroscience*, vol. 3, no. 2, pp. 142–151, 2002.
- [73] G.D. Iannetti and R. G. Wise, "BOLD functional MRI in disease and pharmacological studies: room for improvement?," *Magnetic Resonance Imaging*, vol. 25, no. 6, pp. 978 – 988, 2007, Proceedings of the International School on Magnetic Resonance and Brain Function Proceedings of the International School on Magnetic Resonance and Brain Function.
- [74] A. L. Vazquez and D. C. Noll, "Nonlinear aspects of the BOLD response in functional MRI," *NeuroImage*, vol. 7, no. 2, pp. 108 – 118, 1998.
- [75] N. Zhang, E. Yacoub, X.H. Zhu, K. Ugurbil, and W. Chen, "Linearity of blood-oxygenation-level dependent signal at microvasculature," *NeuroImage*, vol. 48, no. 2, pp. 313 – 318, 2009.
- [76] R. D. Hoge, J. Atkinson, B. Gill, G. R. Crelier, S. Marrett, and G. B. Pike, "Linear coupling between cerebral blood flow and oxygen consumption in activated human cortex," *Proceedings of the National Academy of Sciences*, vol. 96, no. 16, pp. 9403–9408, 1999.
- [77] K.J. Friston, A. Mechelli, R. Turner, and C.J. Price, "Nonlinear responses in fmri: The balloon model, volterra kernels, and other hemodynamics," *NeuroImage*, vol. 12, no. 4, pp. 466 – 477, 2000.
- [78] K. J. Friston, S. Williams, R. Howard, R. S. J. Frackowiak, and R. Turner, "Movement-related effects in fMRI time-series," *Magnetic Resonance in Medicine*, vol. 35, pp. 346–355, 1996.
- [79] Torben E. Lund, Kristoffer H. Madsen, K. Sidaros, W.L. Luo, and T. E. Nichols, "Non-white noise in fmri: Does modelling have an impact?," *NeuroImage*, vol. 29, no. 1, pp. 54 – 66, 2006.

- [80] Daniel A. Handwerker, John M. Ollinger, and Mark D’Esposito, “Variation of {BOLD} hemodynamic responses across subjects and brain regions and their effects on statistical analyses,” *NeuroImage*, vol. 21, no. 4, pp. 1639 – 1651, 2004.
- [81] A. M. Smith, B. K. Lewis, U. E. Ruttimann, F. Q. Ye, T. M. Sinnwell, Y. Yang, J. H. Duyn, and J. A. Frank, “Investigation of low frequency drift in fmri signal,” *NeuroImage*, vol. 9, no. 5, pp. 526 – 533, 1999.
- [82] E. Zarahn, G.K. Aguirre, and M. D’Esposito, “Empirical analyses of {BOLD} fmri statistics,” *NeuroImage*, vol. 5, no. 3, pp. 179 – 197, 1997.
- [83] M. M. Monti, “Statistical analysis of fmri time-series: A critical review of the glm approach,” *Frontiers in Human Neuroscience*, vol. 5, pp. 28, 2011.
- [84] J. V. Stone and J. Porrill, “Independent component analysis and projection pursuit: A tutorial introduction,” 1998.
- [85] I. Khalidov and M. Unser, “From differential equations to the construction of new wavelet-like bases,” *IEEE Transactions on Signal Processing*, vol. 54, no. 4, pp. 1256–1267, April 2006.
- [86] C. Caballero G., N. Petridou, I. L. Dryden, L. Bai, S. T. Francis, and P. A. Gowland, “Detection and characterization of single-trial fmri bold responses: Paradigm free mapping,” *Human Brain Mapping*, vol. 32, no. 9, pp. 1400–1418, 2011.
- [87] F.I. Karahanoglu, I. Bayram, and D. Van De Ville, “A signal processing approach to generalized 1-d total variation,” *IEEE Transactions on Signal Processing*, vol. 59, no. 11, pp. 5265–5274, Nov 2011.
- [88] L. Berman and A. Feuer, “On perfect conditioning of vandermonde matrices on the unit circle,” *ELA. The Electronic Journal of Linear Algebra [electronic only]*, vol. 16, pp. 157–161, 2007.
- [89] J. Ashburner and K.J. Friston, “Unified segmentation,” *NeuroImage*, vol. 26, pp. 839–851, 2005.
- [90] Y. Alemán-Gómez, L. Melie-García, and P. Valdés-Hernandez, “IBASPM: Toolbox for automatic parcellation of brain structures,” in *12th Annual Meeting of the Organization for Human Brain Mapping*, June 2006.
- [91] V. Isakov, *Inverse Problems for Partial Differential Equations*, Number v. 127 in Applied Mathematical Sciences (Springer-Verlag), Vol 127. Springer, 1998.
- [92] A.J. Devaney, *Mathematical Foundations of Imaging, Tomography and Wavefield Inversion*, Mathematical Foundations of Imaging, Tomography and Wavefield Inversion. Cambridge University Press, 2012.
- [93] A. Fannjiang, T. Strohmer, and P. Yan, “Compressed remote sensing of sparse objects,” *SIAM Journal on Imaging Sciences*, vol. 3, no. 3, pp. 595–618, 2010.
- [94] R. Baraniuk, “Compressive radar imaging,” in *Proc. 2007 IEEE Radar Conf*, 2007, pp. 128–133.
- [95] A. E. Badia and T. Nara, “An inverse source problem for Helmholtz’s equation from the Cauchy data with a single wave number,” *Inverse Problems*, vol. 27, no. 10, pp. 105001, 2011.
- [96] D. Finch and S. Patch, “Determining a function from its mean values over a family of spheres,” *SIAM Journal on Mathematical Analysis*, vol. 35, no. 5, pp. 1213–1240, 2004.

- [97] S. Andrieux and A. B. Abda, "Identification of planar cracks by complete overdetermined data: inversion formulae," *Inverse Problems*, vol. 12, no. 5, pp. 553, 1996.
- [98] I. Daubechies, *Ten lectures on wavelets*, Society for Industrial and Applied Mathematics, 1 edition, June 1992.
- [99] Z. M. Wu and J. P. Liu, "Generalized strang-fix condition for scattered data quasi-interpolation.," *Adv. Comput. Math.*, vol. 23, no. 1-2, pp. 201–214, 2005.
- [100] E. Kreyszig, *Introductory Functional Analysis with Applications*, Wiley classics library. Wiley India Pvt. Limited, 2007.
- [101] G.G.B. Arfken and H.J. Weber, *Mathematical Methods for Physicists*, Academic Press, 2005.
- [102] Y. Tao, K. Yi, C. Sheng, and P. Kalnis, "Efficient and accurate nearest neighbor and closest pair search in high-dimensional space," *ACM Trans. Database Syst.*, vol. 35, no. 3, pp. 20:1–20:46, July 2010.
- [103] M. I. Shamos and D. Hoey, "Closest-point problems," in *Foundations of Computer Science, 1975., 16th Annual Symposium on*, Oct 1975, pp. 151–162.
- [104] L. V. Wang, "Multiscale photoacoustic microscopy and computed tomography," *Nature photonics*, vol. 3, no. 9, pp. 503–509, Aug. 2009.
- [105] Lihong V. W. and Song H., "Photoacoustic tomography: In vivo imaging from organelles to organs," *Science*, vol. 335, no. 6075, pp. 1458–1462, 2012.
- [106] H. Ammari, E. Bossy, V. Jugnon, and H. Kang, "Mathematical modeling in photoacoustic imaging of small absorbers," *SIAM Review*, vol. 52, pp. 677–695, November 2010.
- [107] M. Xu and L. V. Wang, "Universal back-projection algorithm for photoacoustic computed tomography," *Phys. Rev. E*, vol. 75, pp. 059903, May 2007.
- [108] Minghua X., Yuan X., and L.V. Wang, "Time-domain reconstruction algorithms and numerical simulations for thermoacoustic tomography in various geometries," *IEEE Transactions on Biomedical Engineering*, vol. 50, no. 9, pp. 1086–1099, sept. 2003.
- [109] Yuan Xu, Minghua Xu, and Lihong V. Wang, "Exact frequency-domain reconstruction for thermoacoustic tomography: II. cylindrical geometry.," *IEEE Transactions on Medical Imaging*, vol. 21, no. 7, pp. 829–833, 2002.
- [110] G. Paltauf, J. A. Viator, S. A. Prahl, and S. L. Jacques, "Iterative reconstruction algorithm for optoacoustic imaging," *The Journal of the Acoustical Society of America*, vol. 112, no. 4, pp. 1536–1544, 2002.
- [111] A. Buehler, A. Rosenthal, T. Jetzfellner, A. Dima, D. Razansky, and V. Ntziachristos, "Model-based optoacoustic inversions with incomplete projection data," *Medical Physics*, vol. 38, no. 3, pp. 1694–1704, 2011.
- [112] V Isakov, "Uniqueness and stability in multi-dimensional inverse problems," *Inverse Problems*, vol. 9, no. 6, pp. 579, 1993.
- [113] I. B: Hagai, F.M. Fazi, and B. Rafaely, "Generalized sampling expansion for functions on the sphere," *IEEE Transactions on Signal Processing*, vol. 60, no. 11, pp. 5870–5879, 2012.
- [114] J.D. McEwen and Y. Wiaux, "A novel sampling theorem on the sphere," *IEEE Transactions on Signal Processing*, vol. 59, no. 12, pp. 5876–5887, 2011.

- [115] B. Rafaely, “Analysis and design of spherical microphone arrays,” *IEEE Transactions on Speech and Audio Processing*, vol. 13, no. 1, pp. 135–143, 2005.
- [116] B. Rafaely, B. Weiss, and E. Bachmat, “Spatial aliasing in spherical microphone arrays,” *IEEE Transactions on Signal Processing*, vol. 55, no. 3, pp. 1003–1010, 2007.
- [117] L.V. Wang, *Photoacoustic Imaging and Spectroscopy*, Optical Science and Engineering. CRC Press, 2009.
- [118] M. Unser and P.D. Tafti, *An Introduction to Sparse Stochastic Processes*, Cambridge University Press, Cambridge, UK, 2014, 367 p.
- [119] M. D. Buhmann and M. D. Buhmann, *Radial Basis Functions*, Cambridge University Press, New York, NY, USA, 2003.
- [120] T. Blu and M. Unser, “Wavelets, fractals, and radial basis functions,” *IEEE Transactions on Signal Processing*, vol. 50, no. 3, pp. 543–553, Mar 2002.
- [121] J. Duchon, “Splines minimizing rotation-invariant semi-norms in sobolev spaces,” in *Constructive Theory of Functions of Several Variables*, Walter Schempp and Karl Zeller, Eds., vol. 571 of *Lecture Notes in Mathematics*, pp. 85–100. Springer Berlin Heidelberg, 1977.
- [122] K. Wang and M. Anastasio, “Photoacoustic and thermoacoustic tomography: Image formation principles,” in *Handbook of Mathematical Methods in Imaging*, Otmar Scherzer, Ed., pp. 781–815. Springer New York, 2011.
- [123] F Natterer and F Wubbeling, “A propagation-backpropagation method for ultrasound tomography,” *Inverse Problems*, vol. 11, no. 6, pp. 1225, 1995.
- [124] P. De Vries, D. V. Van Coevorden, and A. Lagendijk, “Point scatterers for classical waves,” *Rev. Mod. Phys.*, vol. 70, pp. 447–466, Apr 1998.
- [125] M. Xu and L.V. Wang, “Photoacoustic imaging in biomedicine,” *Rev. Sci. Instrum.*, vol. 77, no. 4, pp. 041101, 2006.
- [126] J. Tian, X. Yang, C. Qin, and K. Liu, “Bioluminescence tomography,” in *Molecular Imaging*, Advanced Topics in Science and Technology in China, pp. 217–240. Springer Berlin Heidelberg, 2013.
- [127] A. J. Berkhout, D. de Vries, and P. Vogel, “Acoustic control by wave field synthesis,” *The Journal of the Acoustical Society of America*, vol. 93, no. 5, pp. 2764–2778, 1993.
- [128] M. M. Boone, E. N. G. Verheijen, and P. F. Van Tol, “Spatial sound-field reproduction by wave-field synthesis,” *J. Audio Eng. Soc.*, vol. 43, no. 12, pp. 1003–1012, 1995.
- [129] Q. Wang, O. Ronneberger, and H. Burkhardt, “Rotational invariance based on Fourier analysis in polar and spherical coordinates,” *IEEE Transactions on Pattern Analysis and Machine Intelligence*, vol. 31, no. 9, pp. 1715–1722, Sept 2009.
- [130] R. Mehrem, “The plane wave expansion, infinite integrals and identities involving spherical bessel functions,” *Applied Mathematics and Computation*, vol. 217, no. 12, pp. 5360 – 5365, 2011.
- [131] H. W. Engl, M. Hanke, and A. Neubauer, *Regularization of Inverse Problems*, Springer, 1996.
- [132] A. Beck and M. Teboulle, “A fast iterative shrinkage-thresholding algorithm for linear inverse problems,” *SIAM Journal on Imaging Sciences*, vol. 2, no. 1, pp. 183–202, 2009.

- [133] L. I. Rudin, S. Osher, and E. Fatemi, “Nonlinear total variation based noise removal algorithms,” *Phys. D*, vol. 60, no. 1-4, pp. 259–268, Nov. 1992.
- [134] Z. Doğan, “Deconvolution with sparsity constraints,” M.S. thesis, EPFL, STI, EPFL, Switzerland, 2011.
- [135] S. Boyd, N. Parikh, E. Chu, B. Peleato, and J. Eckstein, “Distributed optimization and statistical learning via the alternating direction method of multipliers,” *Found. Trends Mach. Learn.*, vol. 3, no. 1, pp. 1–122, Jan. 2011.
- [136] Yilun Wang, Junfeng Yang, Wotao Yin, and Yin Zhang, “A new alternating minimization algorithm for total variation image reconstruction,” *SIAM Journal on Imaging Sciences*, vol. 1, no. 3, pp. 248–272, Aug. 2008.
- [137] F. Pinto and M. Vetterli, “Space/time-frequency processing of acoustic wave fields: theory, algorithms, and applications,” *IEEE Transactions on Signal Processing*, vol. 58, no. 9, pp. 4608–4620, 2010.
- [138] T. Ajdler, *The plenacoustic function and its applications*, Ph.D. thesis, IC, Lausanne, 2006.
- [139] M. Kolundzija, *Spatial Acoustic Signal Processing*, Ph.D. thesis, IC, Lausanne, 2012.
- [140] F. J. Simons and F. A. Dahlen, “Spherical Slepian functions and the polar gap in geodesy,” *Geophys. J. Int.*, vol. 166, pp. 1039–1061, 2006.
- [141] F. J. Simons, “Slepian functions and their use in signal estimation and spectral analysis,” in *Handbook of Geomathematics*, pp. 891–923. Springer, 2010.
- [142] F. Natterer and F. Wubbeling, *Mathematical Methods in Image Reconstruction*, Society for Industrial and Applied Mathematics, 2001.
- [143] F. Natterer, *The Mathematics of Computerized Tomography*, Society for Industrial and Applied Mathematics, 2001.
- [144] I. Khalidov, M. Unser, and J.P. Ward, “Operator-like wavelet bases of $l_2(R^d)$,” *The Journal of Fourier Analysis and Applications*, vol. 19, no. 6, pp. 1294–1322, December 2013.
- [145] E. Cands, L. Demanet, D. Donoho, and L. Ying, “Fast discrete curvelet transforms,” *Multiscale Modeling & Simulation*, vol. 5, no. 3, pp. 861–899, 2006.
- [146] M. Jianwei and G. Plonka, “The curvelet transform,” *IEEE Signal Processing Magazine*, vol. 27, no. 2, pp. 118–133, March 2010.
- [147] P.L. Dragotti and Y.M. Lu, “On sparse representation in Fourier and local bases,” *IEEE Transactions on Information Theory*, vol. 60, no. 12, pp. 7888–7899, Dec 2014.
- [148] M. Unser, P.D. Tafti, and Q. Sun, “A unified formulation of Gaussian versus sparse stochastic processes—Part I: Continuous-domain theory,” *IEEE Transactions on Information Theory*, vol. 60, no. 3, pp. 1945–1962, March 2014.
- [149] M. Unser, P.D. Tafti, A. Amini, and H. Kirshner, “A unified formulation of Gaussian versus sparse stochastic processes—Part II: Discrete-domain theory,” *IEEE Transactions on Information Theory*, vol. 60, no. 5, pp. 3036–3051, May 2014.
- [150] F. Luisier, T. Blu, and M. Unser, “A new SURE approach to image denoising: Interscale orthonormal wavelet thresholding,” *IEEE Transactions on Image Processing*, vol. 16, no. 3, pp. 593–606, March 2007.

- [151] T. Blu, “The SURE-LET methodology—A prior-free approach to signal and image denoising,” in *Plenary Presentation at the Eighth International Workshop on Sampling Theory and Applications (SampTA'09)*, May 18–22, 2009.

Zafer Dogan

EPFL/IBI-STI GRVDV
Station 17 CH-1015 Lausanne
+41786274860
zafer.dogan@epfl.ch
<http://miplab.epfl.ch/dogan/>



Key Strengths

- **+6 years of experience** in research, algorithm development and coding in **MATLAB** and **JAVA**
- PhD on **inverse problems** with sparse signal representations and nonlinear recovery methods
- MSc on **information technologies** with specialization on **image processing**
- Main interests: Inverse problems, **statistical modeling**, **data analysis**, sparsity, and **inference**
- Diverse technical and communication skills enabling to work in **multidisciplinary** and **dynamic** fields

Education

Apr. 2011–	École Polytechnique Fédérale de Lausanne (EPFL), Lausanne, Switzerland
Apr. 2015 ^(Exp.)	PhD in Electrical Engineering: “ <i>Non-linear Recovery of Sparse Signal Representations with Applications to Temporal and Spatial Localization</i> ” Advisor: Prof. Dimitri Van de Ville, Co-advisor: Prof. Thierry Blu
Sept. 2009–	École Polytechnique Fédérale de Lausanne (EPFL), Lausanne, Switzerland
Feb. 2011	MSc in Electrical Engineering, “ <i>De-convolution with sparsity constraints</i> ”, Advisor: Prof. Michael Unser Graduate GPA: 5.67 /6.00, Graduate Rank: 2 out of 31 (Information Technologies)
Sept. 2005–	Middle East Technical University (METU), Ankara, Turkey
June 2009	BSc in Electrical and Electronics Engineering Graduate GPA: 3.94 /4.00, Graduate Rank: 5 out of 209

Technical Experience

(Research)	EPFL, Medical Image Processing Lab , (PhD Thesis)
2011 – now	Development of robust algorithms for solving inverse problems in image and signal processing applications with several contributions at renowned international conferences and journals. <ul style="list-style-type: none">• Generalized Sensing Principle: Developed recovery frameworks to deal with the inverse source problem of radiating fields from boundary measurements for the localization of sparse objects in tomography and radar imaging [1, 3-6].• FRI Sampling/Recovery: Developed a novel spectral estimation algorithm for the recovery of sparse events from severely degraded samples [A].• Neuroimaging: Developed a framework for the detection of spontaneous and resting-state brain activity in functional magnetic resonance imaging data [2,B].• Non-linear Recovery of Sparse Signal Representations: Developed fast, non-linear recovery methods for sparse representations signal with application [C]
(Teaching)	EPFL , (Doctoral School of Electrical Engineering)
2011 – now	Image Processing I & II: The theory and practice of image processing with integrated lab sessions for software development in JAVA
(Supervision)	EPFL, Medical Image Processing Lab , (Student project supervision)
Spring 2013	<ul style="list-style-type: none">• Sparse recovery for spherical harmonics expansion
Spring 2011	<ul style="list-style-type: none">• Wave-based analytic sensing and its applications [7]
	EPFL, Biomedical Imaging Group , (Master thesis)
2010-2011	Developed a regularization method for de-noising and de-blurring of images [8].
	TUBITAK, Space Research Center, Ankara (Student researcher)
2008-2009	Developed data hiding methods for video applications against compression attacks [9].

Skills

Data Processing	Signal & Image Processing: Signal models, interpolation, estimation , restoration, data analysis , machine learning and classification, Functional and complex analysis, estimation theory, classical and Bayesian statistics , harmonics analysis, convex optimization
Scientific Computing	Programming languages: MATLAB , C, C++, JAVA , R , Python Software development: Eclipse, MS Visual Studio, Xcode Publishing: LATEX, TEX, MS Office, Keynote, Photoshop, HTML/CSS
Languages	English (fluent), French (intermediate), German (intermediate) and Turkish (native)

Publications

- [1] Dogan, Z., Blu, T. & Van De Ville, "Finite-rate-of-innovation for the inverse source problem of radiating fields", Sampling Theory in Signal and Image Processing, Vol. 13, No. 3, pp. 271-294, 2014.
- [2] Dogan, Z., Blu, T. & Van De Ville, D., "Detecting Spontaneous Brain Activity in Functional Magnetic Resonance Imaging using Finite Rate of Innovation", Proceedings of the Eleventh IEEE International Symposium on Biomedical Imaging: From Nano to Macro (ISBI'14), Beijing, China, pp. 1047-1050, April 29--May 2, 2014.
- [3] Dogan, Z., Blu, T. & Van De Ville, D., "Eigensensing And Deconvolution For The Reconstruction Of Heat Absorption Profiles From Photoacoustic Tomography Data", Proceedings of the Tenth IEEE International Symposium on Biomedical Imaging: From Nano to Macro (ISBI'13), San Francisco, USA, pp. 1142-1145, April 7--11, 2013. (★ **Student Paper Award Finalist**)
- [4] Dogan, Z., Jovanovic, I., Blu, T. & Van De Ville, D., "Localization of Point Sources in Wave Fields From Boundary Measurements Using New Sensing Principle", Proceedings of the Tenth International Workshop on Sampling Theory and Applications (SampTA'13), Bremen, Germany, pp. 321-324, July 1--5, 2013.
- [5] Zafer Doğan ; Ivana Jovanovic ; Thierry Blu ; Dimitri Van De Ville; "Application of a new sensing principle for photoacoustic imaging of point absorbers". Proc. SPIE 8581, Photons Plus Ultrasound: Imaging and Sensing 2013, 85813Z (March 4, 2013); doi:10.1117/12.2005063.
- [6] Dogan, Z., Jovanovic, I., Blu, T. & Van De Ville, D., "3D reconstruction of wave-propagated point sources from boundary measurements using joint sparsity and finite rate of innovation", Proceedings of the Ninth IEEE International Symposium on Biomedical Imaging: From Nano to Macro (ISBI'12), Barcelona, Spain, pp. 1575-1578, May 2--5
- [7] Dogan, Z., Tsiminaki, V., Jovanovic, I., Blu, T. & Van De Ville, D. "Localization of point sources for systems governed by the wave equation", Wavelets and Sparsity XIV. Proceedings of the SPIE, San Diego, USA, Vol. 8138, pp. 81380P1-11, August 21--24, 2011.
- [8] Z. Dogan, S. Lefkimmatis, A. Bourquard, M. Unser, "A second-order extension of TV regularization for image deblurring", Image Processing (ICIP), 2011 18th IEEE International Conference on, vol., no., pp.705-708, 11-14 Sept. 2011
- [9] Esen, E. ; Dogan, Z. ; Ates, T.K. ; Alatan, A.A., "Comparison of Quantization Index Modulation and Forbidden Zone Data Hiding for compressed domain video data hiding", Signal Processing and Communications Applications Conference, 2009. SIU 2009. IEEE 17th, pp.404-407, April 2009
- [A] Dogan, Z., Blu, T. & Van De Ville, "FRI Sampling and Reconstruction with Model Fitting" (submitted)
- [B] Dogan, Z., Blu, T. & Van De Ville, "Resting State Network using Finite-rate-of-innovation" (in preparation)
- [C] Dogan Z., "Non-linear Recovery of Sparse Signal Representations with Applications", Ph.D. thesis, STI, EPFL, Lausanne, 2015.

Technical Activities

Professional Memberships	Student Member of IEEE (The Institute of Electrical and Electronics Engineers) and SPS (Signal Processing Society) since 2011. Student Member of SIAM (Society for Industrial and Applied Mathematics) since 2011. Student Member of SPIE (international society for optics and photonics) between 2012-2013
Reviewer	IEEE International Symposium on Biomedical Imaging (ISBI) Pattern Recognition in Neuroimaging (PRNI) International Conference on Sampling Theory and Applications (SampTA)

Honors & Awards

2009 – 2011	Excellence fellowship (EPFL) offered to 20 students with outstanding academic records
June 2009	Best Engineering Senior Design Project Award (METU EE Dept.)
2006–2008	Assoc. Prof. Bülent Kerim Altay Award (METU EE Dept.) given to high honor roll students
July 2007	Language Fellowship (German Academic Exchange Service, DAAD)
2006–2009	Rudolf Diesel Excellence Scholarship (MAN Turkey)

References

Prof. Dimitri Van De Ville	EPFL Medical Image Processing Lab University of Geneva Radiology, CIBM	+41 21 6939669 +41 22 3725215	dimitri.vandeville@epfl.ch
Prof. Thierry Blu	Chinese University of Hong Kong Department of Electronic Engineering	+852 3943 8288	thierry.blu@m4x.org